POLYTECHNIQUE MONTRÉAL
affiliée à l'Université de Montréal

Real-Time Microwave Signal Processing: Dispersion Engineering and Time Modulation

XIAOYI WANG
Département de génie électrique

Thèse présentée en vue de l'obtention du diplôme de *Philosophiæ Doctor*
génie électrique

Septembre 2020

POLYTECHNIQUE MONTRÉAL
affiliée à l'Université de Montréal

Cette thèse intitulée :

Real-Time Microwave Signal Processing: Dispersion Engineering and Time Modulation

présentée par **Xiaoyi WANG**
en vue de l'obtention du diplôme de *Philosophiæ Doctor*
a été dûment acceptée par le jury d'examen constitué de :

Ke WU, président
Christophe CALOZ, membre et directeur de recherche
Mohammad S. SHARAWI, membre et codirecteur de recherche
Shulabh GUPTA, membre
Qingfeng ZHANG, membre externe

DEDICATION

To my family

ACKNOWLEDGEMENTS

I would like to express my sincere gratitude to all the people who have helped me during my Ph.D. study.

My deepest gratitude goes to my Ph.D. supervisor, Prof. Christophe Caloz, who has been the educator, the motivator, and the mentor for my Ph.D. research and my life beyond research. His attitude and effort to scientific work affect me a lot and light me to face the challenges in my future career path.

I would like to express my thank to my Ph.D. co-supervisor, Prof. Mohammad S. Sharawi for having accepted me during the last year of my Ph.D. study.

I would like to convey my acknowledgement to the committee members, Prof. Ke Wu from École Polytechnique de Montréal, Prof. Shulabh Gupta from Carelton University and Prof. Qingfeng Zhang from South University of Science and Technology of China, for having accepted to examine my Ph.D. thesis.

I would also like to thank my colleagues Lianfeng Zou, Zoé-Lise Deck-Léger, Luzhou Chen, Ashutosh Patri, Karim Achouri, Guillaume Lavigne, Yousef Vahabzadeh, Oscar V. Céspedes, Xiao Jia, Chunmei Liu, Xiaoqiang Gu, Desong Wang, Yifan Yin and many others for their invaluable help on my Ph.D. research.

I would also like to thank all the technicians at Poly-Grames Research Center, Mr. Jules Gauthier, Mr. Jean-Sébastien Décarie, Mr. Traian Antonescu, Mr. David Dousset and Mr. Steve Dubé for their suggestions and help on my research.

Last but not least, many loves go to my family, for always being supportive and helpful during my Ph.D. study.

RÉSUMÉ

Il y a aujourd'hui une demande pour des systèmes radiofréquences ayant une large bande passante, une faible latence, des bas coûts, une grande fiabilité et une faible consommation d'énergie. Par exemple, la prochaine génération de systèmes sans fil mobiles devrait avoir une capacité mille fois plus élevée qu'aujourd'hui pour répondre aux exigences de diverses applications telles que les véhicules sans pilote et la télémédecine. Bien que la technologie dominante actuelle, le traitement de signal numérique (DSP en anglais), soit compacte, flexible et précise, elle souffre de problèmes fondamentaux, notamment une consommation d'énergie élevée, une conversion analogique-numérique coûteuse, une bande passante limitée, un stockage en mémoire faible et une mauvaise performance aux hautes fréquences. Par conséquent, nous proposons ici d'effectuer le traitement du signal micro-ondes analogiquement et en temps réel. Cette technique attrayante a été peu explorée jusqu'à présent, et pourrait remplacer ou complémenter le traitement numérique.

Le chapitre 1 présente la motivation du traitement du signal micro-ondes analogique en temps réel (R-MSP), deux solutions R-MSP complémentaires basées respectivement sur l'ingénierie de la dispersion et la modulation du temps, ainsi que les contributions de cette thèse.

Les chapitres 2 et 3 proposent deux applications basées sur l'ingénierie de dispersion pour le traitement des signaux micro-ondes. Cette technologie est inspirée de l'optique ultra-rapide, où les signaux électromagnétiques sont traités en temps réel à l'aide de composants optiques dispersifs. Dans le domaine des micro-ondes, ces composants conçus pour la dispersion ont reçu le nom de "phaseurs" et, comme leurs homologues optiques, manipulent la phase ou le retard de groupe des signaux d'entrée. En concevant les caractères de dispersion des composants, diverses fonctions peuvent être réalisées.

Le chapitre 2 présente un transformateur de Hilbert hyperfréquence. Ce transformateur de Hilbert est basé sur la combinaison d'un coupleur et d'un résonateur en boucle. La fonction de transfert du transformateur est dérivée à l'aide de graphiques de flux de signaux, et deux chiffres de mérite sont introduits pour caractériser efficacement le dispositif. De plus, une explication détaillée de son fonctionnement physique est fournie. Le transformateur micro-ondes de Hilbert est démontré expérimentalement dans trois applications: pour la détection d'un front d'onde, pour la suppression de la crête et pour la modulation à bande latérale unique.

Le chapitre 3 présente une conception de l'ingénierie de la dispersion basée sur un décomposeur de spectre à lentille Rotman planaire (RL-SD) qui offre une flexibilité de résolution,

une position du port d'entrée arbitraire et une plage de fréquences et une résolution réglable. La flexibilité de résolution consiste à autoriser différentes fonctions d'échantillonnage de fréquence en répartissant correctement les emplacements des ports de sortie. La position arbitraire du port d'entrée est réalisée en ajoutant un réseau d'étalonnage compensant l'écart de fréquence induit par la modification du port d'entrée. Les réglages de la plage de fréquences et de la résolution sont réalisés par la commutation du port d'entrée.

Le traitement du signal micro-ondes basé sur une modulation temporelle fait référence aux technologies de traitement du signal où les propriétés du signal varient dans le temps, et ce grâce aux variations temporelles des paramètres physiques du système. Par rapport aux technologies basées sur l'ingénierie de dispersion, qui sont invariantes dans le temps et limitées par des limites physiques fondamentales, les technologies de modulation du temps brisent ces limites et permettent une manipulation universelle des spectres temporels et spatiaux des ondes électromagnétiques.

Le chapitre 4 présente une technologie de camouflage basée sur une métasurface modulée dans le temps. Différente des technologies de camouflage conventionnelles, généralement invariantes dans le temps (LTI), la technologie proposée est active et répartit l'énergie incidente dans le spectre temporel. En outre, cette technologie module la métasurface avec une séquence pseudo-aléatoire, qui répartit le spectre de l'onde incidente en un spectre semblable à du bruit avec une densité spectrale de puissance minimale, et donc des performances de camouflage maximales.

Enfin, le chapitre 5 résume les travaux de cette thèse, souligne les limites actuelles de R-MSP et suggère des sujets potentiels pour de futurs travaux.

ABSTRACT

Today's exploding demands for wider bandwidth, lower latency, lower cost and more reliable and power-efficient radio systems bring more challenges for signal processing technologies. For example, the next generation mobile wireless systems in the coming decade is expected to have thousand times higher capacity than it is right now to meet the requirements of various applications, for instance, unmanned vehicles and telemedicines. Although current dominant technology, digital signal processing (DSP), offers the benefits of device compactness and processing flexibility and preciseness, it also suffers fundamental issues, including high power consumption, high-cost analog-digital conversion, limited operating bandwidth, low memory storage, and poor performance at high frequencies. Therefore, processing microwave signal in real time and purely analog domain as an alternative or complementary technique is desired, which is attractive but less explored till now. Chapter 1 introduces the motivation of real-time microwave signal processing (R-MSP) and two complementary R-MSP solutions based on dispersion engineering and time modulation, respectively, along with the contributions of this thesis.

Dispersion engineering based microwave signal processing is a signal processing technology inspired from ultra-fast optics, where electromagnetic signals are processed in real-time using dispersive optical components. In microwave domain, these dispersion-engineered components have been given the name "phasers" and, similar to its optical counterpart, manipulates the phase or the group delay of input signals. By engineering the dispersion characters of the components, various functions may be realized. In chapters 2 and 3, two applications based on dispersion engineering for microwave signal processing are proposed.

Chapter 2 presents a microwave Hilbert transformer as a new component for R-MSP. This Hilbert transformer is based on the combination of a branch-line coupler and a loop resonator. The transfer function of the transformer is derived using signal flow graphs, and two figures of merits are introduced to effectively characterize the device. Moreover, a detailed physical explanation of its physical operation is provided. The microwave Hilbert transformer is demonstrated experimentally in three applications: edge detection, peak suppression and single sideband modulation.

Chapter 3 presents a design of dispersion engineering based a planar Rotman lens spectrum decomposer (RL-SD) with the features resolution flexibility, input port position arbitrariness and frequency range and resolution tunability. The resolution flexibility consists in allowing different frequency sampling functions by properly distributing the output port locations.

The input port position arbitrariness is realized by adding a calibration array compensating for the frequency deviation induced by the input port modification. The frequency range and resolution tunability is achieved by input port switching.

Time modulation based microwave signal processing refers to the signal processing technologies whose properties are time-varying introduced by the time variation of their physical parameters. Compared to dispersion engineering based technologies, whose are time-invariant and limited by its fundamental physical bounds, time modulation technologies naturally break these bounds and allow universal manipulation of the temporal and spatial spectra of electromagnetic waves.

Chapter 4 presents a time-modulated metasurface based camouflaging technology. Different conventional camouflaging technologies, which are usually linear time invariant (LTI), the proposed technology is active and spreads the incident energy into temporal spectrum. Besides, this technology modulates the metasurface with a pseudo-random sequence, which spreads the spectrum of the incident wave into a noise-like spectrum with minimal power spectral density, and hence maximal camouflaging performance.

Finally, Chapter 5 summarizes the work of this thesis, points out current limitation of R-MSP and suggests potential topics for future works.

TABLE OF CONTENTS

LIST OF TABLES

LIST OF FIGURES

LIST OF SYMBOLS AND ABBREVIATIONS

Abbreviations

5G	5th Generation
ADC	Analog-Digital Converter
CDMA	Code Division Multiple Access
CRLH	Composite Right/Left-Handed
DC	Direct Current
DCMA	Dispersion Code Multiple Access
DSBP	Delay Swing Bandwidth Product
DSP	Digital Signal Processing
DOA	Direction of Arrival
EBG	Electromagnetic BandGap
FBG	Fiber Bragg Grating
FPGA	Field Programmable Gate Array
HT	Hilbert Transformer
LTI	Linear Time-Invariant
MIM	Metal-insulator-metal
MIMO	Multi-input Multi-output
OFDM	Orthogonal Frequency Division Modulation
OFDMA	Orthogonal Frequency Division Multiple Access
RF	Radio Frequency
RFID	Radio Frequency Identification
RTSS	Real-Time Spectrum Sniffer
R-MAP	Real-time Microwave signal processing
RL	Rotman Lens
RL-SD	Rotlan Lens Spectrum Decomposer
SAW	Surface Acoustic Wave
SD	Spectrum Decomposer
SNR	Signal to Noise Ratio
SSB	Single-Side Bandwidth
ST	Space-Time
UWB	Ultra Wideband

LIST OF APPENDICES

CHAPTER 1 INTRODUCTION

1.1 Background and Motivation

Signal processing refers to the processing technologies that modify, analyze and synthesis signals such as sounds, images and different types of picked up data. It is widely used in our current daily life in order to improve the performance of system by enhancing signal transmission, storage efficiency and quality and to also resolve interest component in a picked up signal.

The principles of signal processing originates in 17th century from the classical numerical analysis techniques. Until 1948, Claude Shannon' work [17] laid the groundwork for later development of information theoretical communication systems and the related signal processing techniques. Signal processing is matured and began to boom in the 1960s, firstly among analog domain and later digital signal processing became widely used with digital signal processor since the 1980s.

Signal processing is wildly applied in many application fields in our world. For example, in audio, signal processing is used to represent sound, such as speech and music. In image, signal processing is used to process the data obtained from cameras and various imaging systems. In wireless communication, signal processing is used in waveform generation, signal modulation and demodulation, equalization,filtering, et al.

Over the past few decades, the requirement for lower latency, wider band, more scalable and reliable micorwave systems in wireless communication systems, radars and sensors have been exploding very fast. More recently, this trend has been predominant to meet modern life's requirements [1]. For instance, game players may expect extremely low latency network without lag, which may lead to delay between the action of the game players and the actual responses within the game. Mobile users may expect to experience much faster and more reliable internet access when having video meetings and uploading and downloading documents. All of these requirements pose unprecedented challenges in signal processing, especially in the widely used digital signal processing (DSP). For example, massive multi-input and multi-output (MIMO) technology, as an extension of current MIMO technology and a key enabler for the forthcoming 5G's extremely fast data rates, needs thousands of antennas and related hardwork implementations, which leads to fast increase of hardware cost and signal processing complexity.

Thanks to the development of semiconductor technology, DSP is popularly applied in today's

signal processing applications and offers many powerful advantages, such as compact-size and high-resolution and processing flexibility. However, DSP also suffers several fundamental issues, for example, high-cost analog-digital conversion, limited operating bandwidth, inevitable memory delay, poor performance at high frequencies, and high power consumption, which may finally result in poor user experience [1].

To overcome these issues, and hence address the aforementioned challenges, advanced microwave analog signal processing with many natural benefits needs to be reconsidered again. Therefore, real-time microwave signal processing (R-MSP), which consists in the potential features of low-cost, wide-band and real-time, are studied in this thesis. Compared to conventional DSP-based signal processing technology, R-MSP may play an important role as an alternative signal processing technology in future microwave systems.

1.2 Real-Time Microwave Signal Processing (R-MSP)

R-MSP is a microwave technology that manipulating microwave electromagnetic signals in real-time to overcome the issues that DSP is facing [1]. In this thesis, We will introduce two different but complementary technologies that are used to process microwave signal in real-time, respectively.

We first introduces dispersion engineering based real-time microwave signal processing, which is a purely passive technology. By engineering the group delay of the microwave devices, varies of signal processing functions can be realized. However, these dispersion engineering devices are usually linear time-invariant (LTI) systems and are limited by the LTI physical bounds, which may limit their functions in many applications. For example, no new frequencies can be generated, therefore, many useful signal processing functions, such as mixing, modulation and precoding, can not be realized. To overcome these issues, time-modulation, a complemental active technology, is also studied to process microwave signals. Different with dispersion engineering based technology, which is the limited by the LTI physical bounds, the time modulated technology naturally breaks these bounds and shows many more promising features than purely passive technologies.

1.2.1 Dispersion Engineering

Dispersion engineering based microwave signal processing is a signal processing technology inspired from ultra-fast optics, where electromagnetic signals are processed in real-time using dispersive optical components. In microwave domain, these dispersion-engineered components are called "phasers", and manipulates the group delay of the components similar to its

optical counterpart [1].

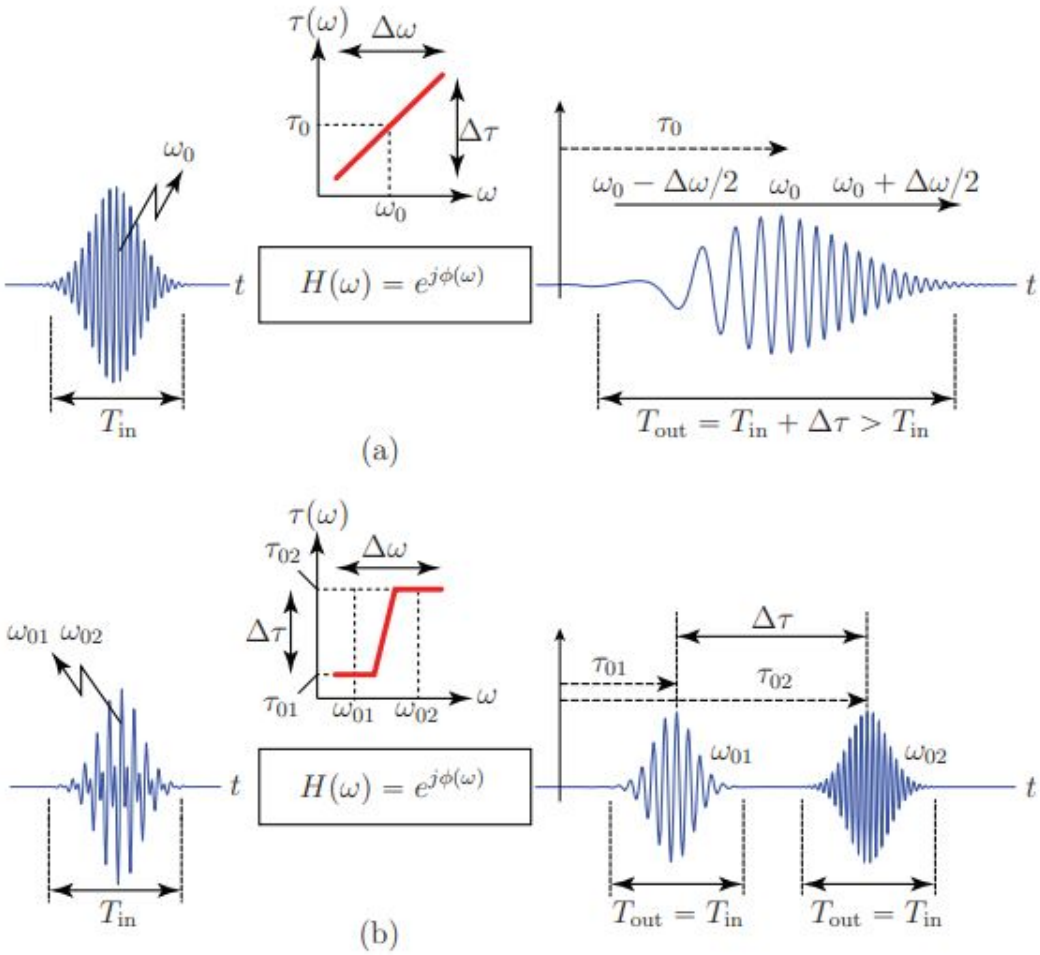

Figure 1.1 Illustration of two phaser effect. (a) Signal chirping. (b) Frequency discrimination (C. Caloz, et. al [1], Microwave Magazine, ©2013 IEEE)

As the core component of dispersion engineering based R-MSP, a phaser is typically engineered to have a frequency-independent magnitude transfer function over a desired bandwidth, i.e. $|H(\omega)| = 1$, and a specified frequency-dependent group delay transfer function, i.e. $\tau(\omega) = -\partial\phi/\partial\omega$ [1,18].

Two typical examples of phaser function, signal chirping and frequency discrimination, are described in Fig. 1.1. In Fig. 1.1(a), a modulated gaussian pulse with a centering frequency ω_0 and a bandwidth $\Delta\omega$ is sent into a phaser with the transfer function $H(\omega)$, which exhibits a positive linear group delay slope. As a result, different spectrum in the gaussian pulse experiences different group delays, which leads to function that the lower-frequency components are less delayed compared to the higher-frequency components and reshapes the modulated pulse into a pulse with increasing chirping spectrum distribution.

In Fig. 1.1(b), the input pulse is modulated by a signal with two frequencies, ω_1 and and ω_2, and is sent into a phaser with a step-case group delay at ω_1 and ω_2, respectively. According to its dispersive feature, the lower frequency experiences smaller delay than the the higher frequency. Thus, the two frequencies are separated in time.

Phasers have been recently realized in many different forms, as shown in Fig. 1.2. For example, in [2, 19–22], C-sections and D-sections are applied to design phasers. In [3, 23] cross-coupled resonators are studied. In [4, 24], nonuniform delay lines are engineered. Some other technologies such as metamaterial transmission-line structures [5] and loss-gain pairs [25] are also investigated .

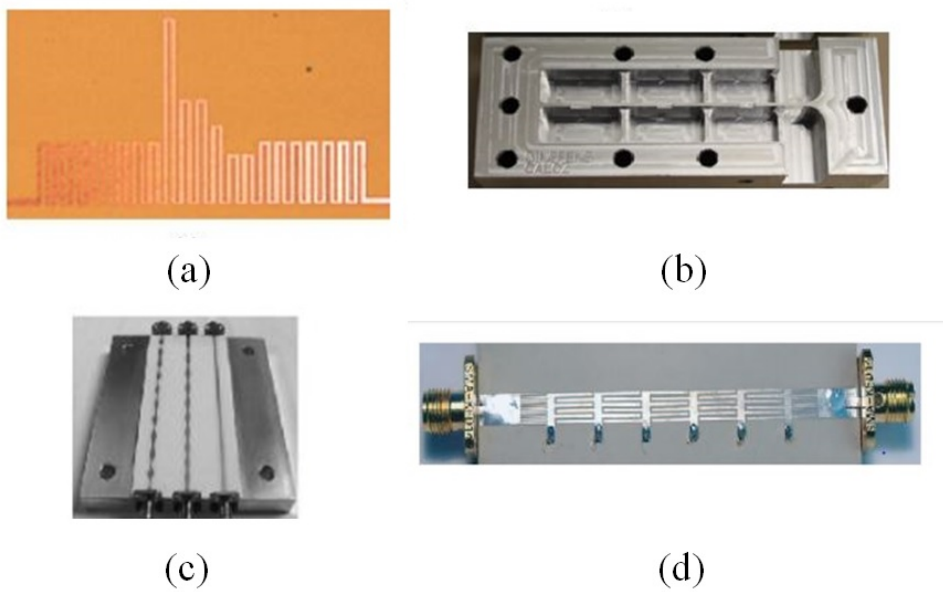

Figure 1.2 Phaser technologies. (a) Cascaded C-section structure [2]. (b) Reflection-type cascaded coupled resonator structure [3]. (c) nonuniform delay line [4]. (d) Metal-insulator-metal (MIM) composite right/left-handed (CRLH) metamaterial structure [5]. (C. Caloz, et, al [1], Microwave Magazine, ©2013 IEEE)

Thanks to these technologies, phasers have been applied in many applications, as shown in Fig. 1.3, including compressive receiving [5], real-time spectrum analysis [6, 26], real-time spectrum sniffing [8], Hilbert transforming [27], SNR enhanced impulse radio transceiving [9], dispersion code multiple access (DCMA) [28], signal encryption [29], and beam scanning in antenna arrays [7].

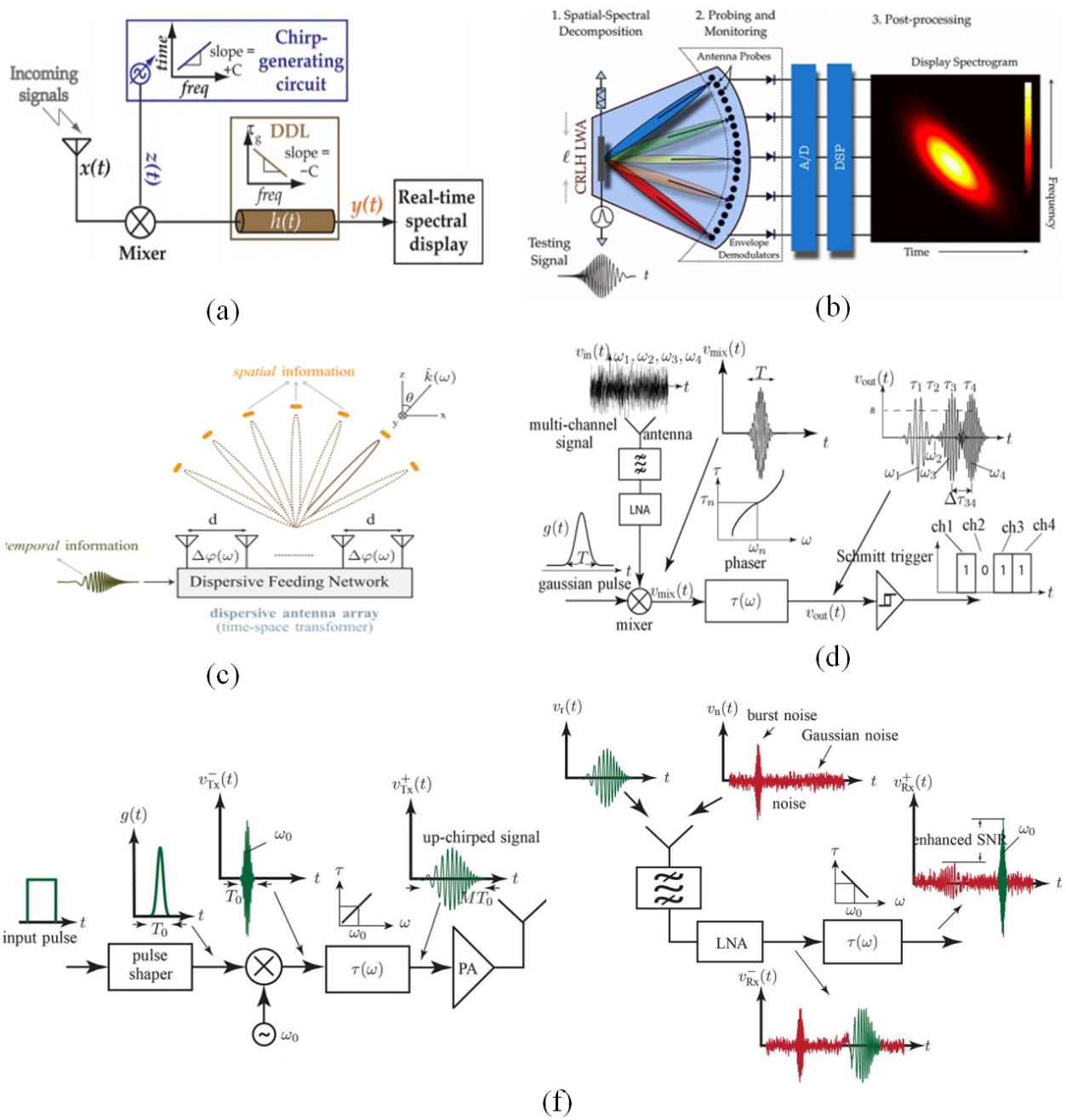

Figure 1.3 Dispersion engineering based R-MSP applications. (a) compressive receiving [5]. (b) Real-time spectrum analysis [6]. (c) Beam scanning array[[7]]. (d) Spectrum sniffing [8]. (e)SNR enhanced impulse radio transceiving [9]. (C. Caloz, et, al [1], Microwave Magazine, ©2013 IEEE)

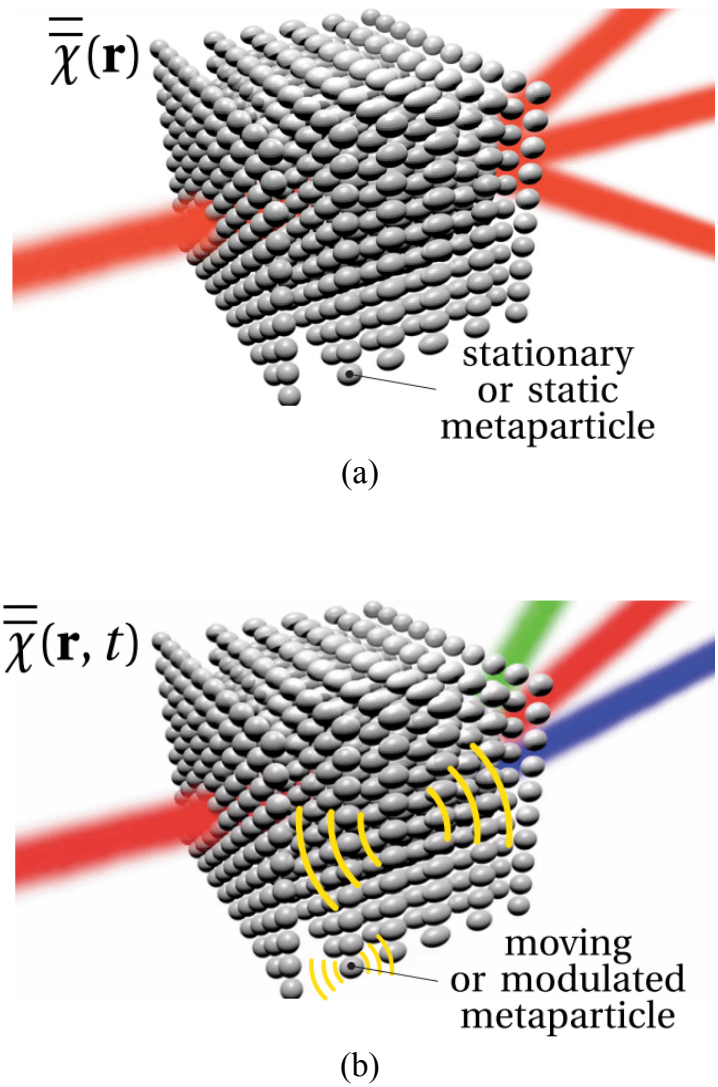

Figure 1.4 Illustration of a time modulated system using the example of a 3-D periodic array. (a) Stationary or static structure,(b) Moving or time-modulated (or space-time modulated) structure. (C. Caloz, et al [10], Trans. Antenn. & Propag., ©2019 IEEE)

1.2.2 Time Modulation

Time modulation based microwave signal processing refers to the signal processing technologies whose properties are time-varying due to the temporal modulation of some of their physical parameters.

Compared to dispersion engineering based technologies, which are time-invariant and limited by their fundamental physical bounds, time modulation technologies naturally break these bounds and allow universal manipulation of the temporal and spatial spectra of electromag-

netic waves and achieve new functionalities [10, 30].

Figure 1.4 shows an example of the comparison between static and time-modulated systems. Figure 1.4(a) represents a stationary system, which scatters diffraction orders from its periodic lattice. Adding a temporal modulation to the spatial variation on the system, and obtaining a hybrid spacetime variation, produces some unique effects, for example, the diffraction orders may be suppressed and new temporal and spatial frequencies are generated [10].

Time modulation has recently been applied in a few applications, shown in Fig. 1.5, such as simplified architecture communication [12, 31–33], direction-of-arrival (DOA) estimation [34], nonreciprocity [14, 35, 36], and analog signal processing [37].

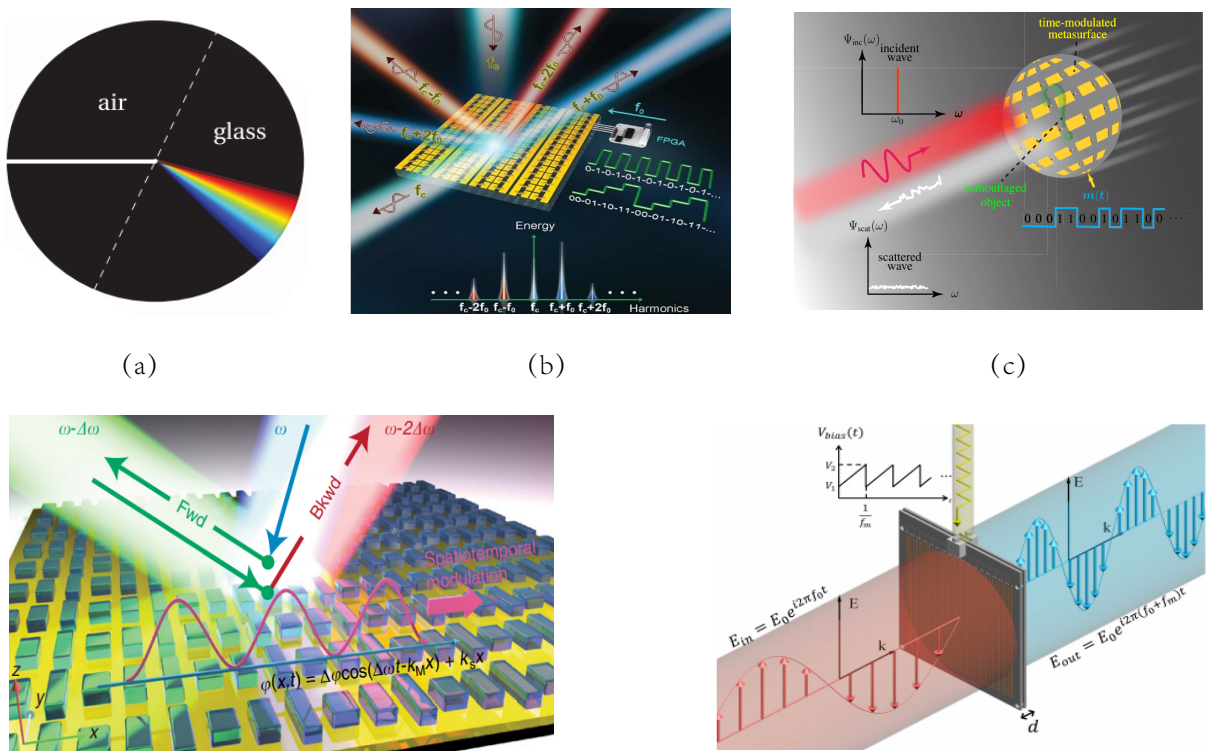

(a) (b) (c)

(d) (e)

Figure 1.5 Time Modulation based R-MSP applications. (a)Inverse prism [11]. (b)Simplified wireless communicaton [12]. (c) Electromagnetic Camouflaging [13]. (d) Nonreciprocity [14]. (e) Frequency translation [15].

1.3 Thesis Major Contributions

This thesis contributes to both of this two aspects of real-time microwave signal processing: dispersion engineering and time modulation. In dispersion engineering technology, two applications, including microwave Hilbert transformer and Rotman lens based spectrum decomposer, are proposed. In time modulation technology, several applications for electromagnetic camouflaging and wireless communication system are studied.

1.3.1 Dispersion Engineering Based Applications for Microwave Hilbert Transformer and Spectrum Decomposition

Microwave Hilbert Transformer

Efficiently performing mathematical operations is central to any type of processing. The Hilbert transformation is a particularly fundamental operation in both physics and engineering. However, the Hilbert transformers reported to date have been exclusively designed in the optical regime using optical fiber structures, which are typically bulky, complex and expensive are not transposable to lower frequencies. Besides they have been mostly described in purely mathematical terms with little insight into the device physics [38].

Chapter 2 presents a branch-line couplers and resonant loops based R-MAP microwave Hilbert transformer, corresponding to the publications [27, 38], and explains the physical operation of this transformer, using both time-domain and steady-state perspectives.

Rotman Lens based Spectrum Decomposition

Spectral Decomposition (SD) is a fundamental optical process according to which white light is spatially split into its constituent frequencies. It is used in various applications, including colorimetry, real-time spectrum analysis, laser wavelength tuning, filtering, wavelength division multiplexing. Most of the conventional SD devices are based on prisms and diffraction gratings, which are three-dimensional components that are bulky, expensive and incompatible with integrated circuit technology. The availability of two-dimensional, or planar, implementations would resolve these issues and hence dramatically widen the range of applications of SD [39].

Chapter 3 presents an enhanced design of the planar Rotman lens spectrum decomposer (RL-SD) in terms of resolution flexibility, input port position arbitrariness and frequency range and resolution tunability, corresponding to publications [39, 40], The resolution flexibility enhancement consists in allowing different frequency sampling functions (decreasing, uniform,

increasing) by properly distributing the output port locations along the frequency-position law of the RL-SD. The input port position arbitrariness is realized by adding a calibration array compensating for the frequency deviation induced by the input modification. The frequency range and resolution tunability is achieved by electronic port switching.

1.3.2 Time Modulation Applications for Electromagnetic Camouflaging

Electromagnetic Camouflaging

Electromagnetic camouflaging refers to concealment technologies whereby objects are made undetectable, which is generally realized by altering the spectrum or power density of the waves scattered by the object to conceal [13]. Such alteration are generally realized in passive technologies, such as including bio-inspired paintings with dazzling or counter-shading patterns [41], absorbing material coatings [42–44], stealth shaping [45].

Chapter 4 presents a time-modulated spread-spectrum metasurface active camouflaging technology, corresponding to publications [13, 46–48]. Compared to conventional camouflaging technologies, which are Linear Time Invariant (LTI) and based on energy absorption or angular spreading, the proposed technology spreads the incident energy in terms of temporal spectrum. Besides, this technology modulates the metasurface with a pseudo-random sequence, which spreads the spectrum of the incident wave into a noise-like spectrum with minimal power spectral density, and hence maximal camouflaging performance; this is much more efficient than the utilization of completely periodic modulation sequence, which distributes the energy over a small number of harmonics. Finally, the proposed technology provides the extra features of selective camouflaging and interference immunity.

CHAPTER 2 MICROWAVE HILBERT TRANSFORMER

R-MSP is a microwave-terahertz-optical technology that consists in manipulating electromagnetic signals in real-time using dispersion-engineered components called phasers [1]. This technology has recently been introduced as a potential high-speed and low-latency alternative to dominantly digital technologies, given its unique features of real-time operation, low-power consumption and low-cost production [1, 49, 50].

Efficiently performing mathematical operations is central to any type of processing. Whereas mathematical operations are completely natural in digital signal processing, they are much less obvious in R-MSP, where they are still essential to help making this technology more flexible and efficient. Fortunately, several real-time analog mathematical operations have already been successfully demonstrated, including differentiation [51], integration [52], expansion and compression [5], time reversal [53], Fourier transformation [4] and Hilbert transformation [54].

The Hilbert transformation is a particularly fundamental operation in both physics and engineering. It has already been implemented in a few R-MSP applications, such as single side-band (SSB) modulation [52, 55], band-pass and band-stop filtering [54] and edge/peak detection [52]. Hilbert transformers have been implemented in different technologies, including impulse-response-sampling filters [56, 57], long-period fiber Bragg gratings [58], optical ring-resonator all-pass filters [52, 59, 60]. However, the Hilbert transformers reported to date have been exclusively designed in the optical regime using optical fiber structures, which are typically bulky, complex and expensive are not transposable to lower frequencies. Besides they have been mostly described in purely mathematical terms with little insight into the device physics.

This chapter presents a real-time microwave Hilbert transformer, based on branch-line couplers and resonant loops, and explains the physical operation of this transformer, using both time-domain and steady-state perspectives. Part of the material in this chapter is excerpt from [27, 38].

2.1 Recall on the Hilbert Transformation

The *Hilbert transformation*, $\mathcal{H}[\cdot]$, is the linear operation depicted in Fig. 2.1. It transforms an input signal $x(t)$ into the output signal $y(t)$ by convolving it with the impulse response

$$h(t) = \frac{1}{\pi t}, \tag{2.1}$$

plotted in Fig. 2.2(a), as [61]

$$y(t) = \mathcal{H}[x(t)] = h(t) * x(t) = \frac{1}{\pi}\,\mathcal{P}.\mathcal{V}.\int_{-\infty}^{+\infty} \frac{x(\tau)}{t-\tau} d\tau, \tag{2.2}$$

where $\mathcal{P}.\mathcal{V}.$ denotes the Cauchy principal value, accommodating for the fact that $h(t)$ is not integrable at $t = 0$.

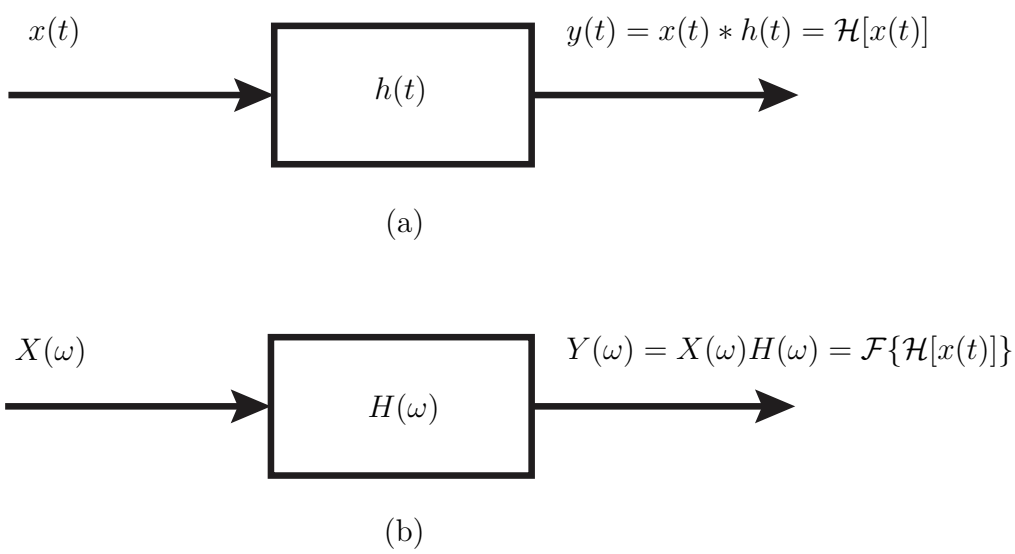

Figure 2.1 Hilbert transformation. (a) Time domain. (b) Frequency domain.

The Fourier transform of (2.2) reads

$$Y(\omega) = H(\omega)X(\omega) = \mathcal{F}\{\mathcal{H}[x(t)]\}, \tag{2.3}$$

where $H(\omega)$ is the transfer function

$$H(\omega) = \begin{cases} i = e^{+\frac{i\pi}{2}}, & \text{if } \omega < 0, \\ 0, & \text{if } \omega = 0, \\ -i = e^{-\frac{i\pi}{2}}, & \text{if } \omega > 0, \end{cases} \tag{2.4}$$

whose magnitude and phase are plotted in Figs. 2.2(b) and 2.2(c), respectively.

The all-pass magnitude and step-rotation phase of $H(\omega)$ in (2.4) are mathematically useful but practically noncausal if t is understood as time. In a physical R-MSP realization, the

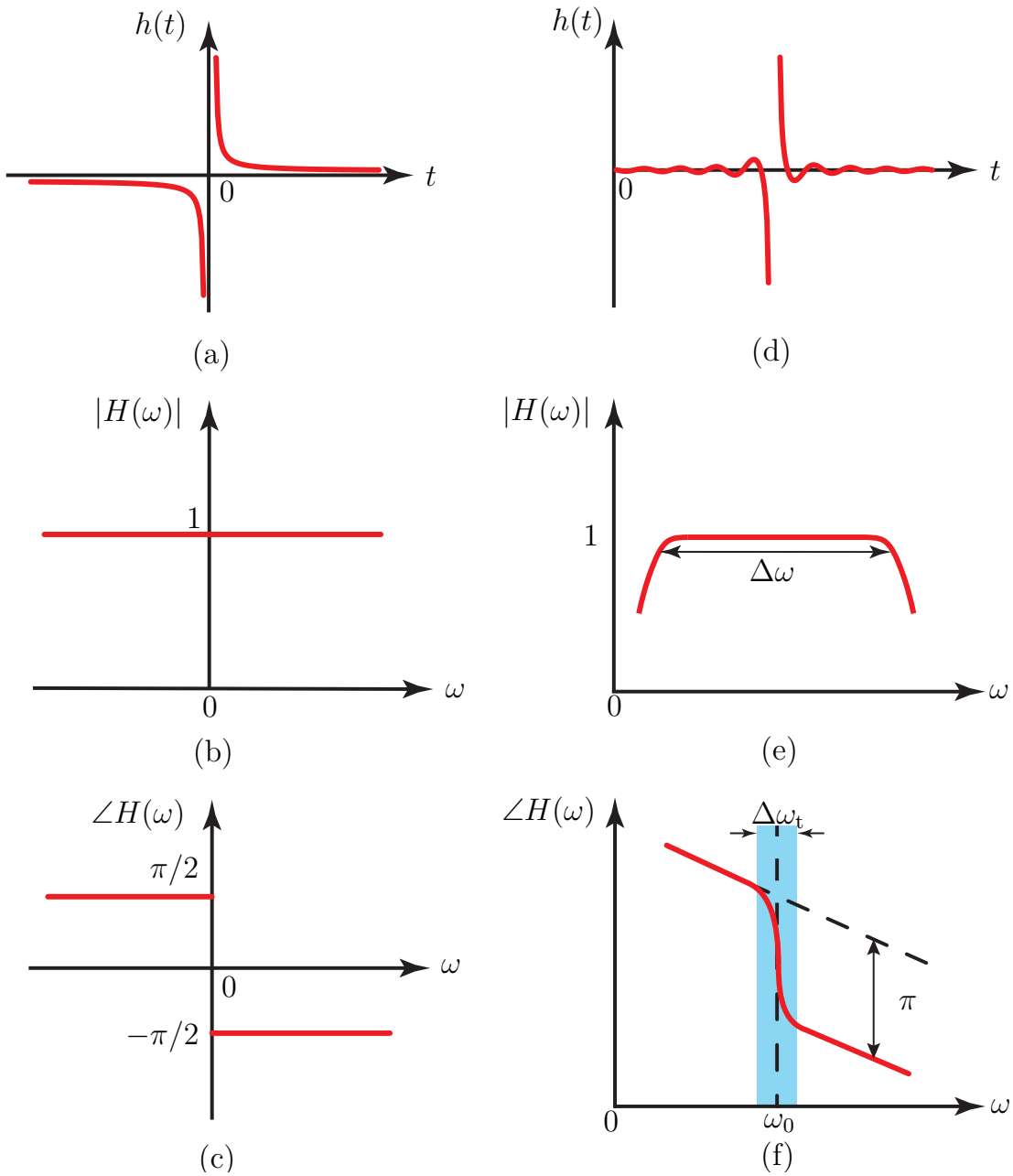

Figure 2.2 Constitutive functions of the mathematical (left) and physical R-MSP (right) Hilbert transform operating around the center frequency of ω_0. (a),(d) Impulse response. (b),(e) Amplitude of the transfer function. (c),(f) Phase of the transfer function.

closest possible magnitude response is the band-pass response shown in Fig. 2.2(e), which features a gradual phase response required by causality and a non-zero phase slope due to physical delay, as shown in Fig. 2.2(f) and corresponding to the impulse function plotted in Fig. 2.2(d). If the signal to process is completely included in the pass-band [Fig. 2.2(e)] of

transformer, then the magnitude limitation is practically not problematic. The consequence of the phase deviation is more subtle, but also not fundamentally problematic in practice. The (nonzero) asymptotic slopes around ω_0 correspond to simple nondispersive delays, which play no processing role other than shifting the entire processed pulse in time. On the other hand, the progressive phase transition is not prohibitive if the signals of interest do not carry energy in that region.

The physical Hilbert transform [Figs. 2.2(e) and (f)] tends to the mathematical Hilbert transform [Figs. 2.2(b) and (c)] if its amplitude bandwidth tends to infinity, or $\Delta\omega \to \infty$, and its π-transition bandwidth tends to zero, or $\Delta\omega_{\mathrm{t}} \to 0$. Since the group delay is the frequency-derivative of the phase, or $\tau(\omega) = -\partial\angle H(\omega)/\partial\omega$, the group delay peaks at ω_0 and its magnitude, $\Delta\tau$, is the proportional to the inverse of the π-transition bandwidth, $\Delta\tau \propto (1/\Delta\omega_{\mathrm{t}})$, one common define the time-bandwidth product as [62]

$$\mathrm{TBP} = \Delta\omega\Delta\tau \propto \Delta\omega/\Delta\omega_{\mathrm{t}}. \tag{2.5}$$

The TBP is a measure of the closeness of the physical transform to its ideal counterpart. If one wishes to realize an transform as close-as-possible to the ideal one, it represent a figure-of-merit of the transform. In practice, one may not necessarily need to realize a close-to-ideal transform and the actual figure-of-merit will need to be defined on case-by-case basis.

Note that applying the Hilbert transform twice restores the initial function except for a negative sign. Indeed,

$$\begin{aligned} \mathcal{H}\{\mathcal{H}[x(t)]\} &= h(t) * [h(t) * x(t)] \\ &= [h(t) * h(t)] * x(t) \\ &= -\delta(t) * x(t) = -x(t). \end{aligned} \tag{2.6}$$

So, once a signal has been processed by a Hilbert transformer, it can be recovered if needed.

2.2 Coupler-Resonator based Hilbert Transformer Analysis

How can one realize a physical component with a transfer function of the type shown in Figs. 2.2(e) and 2.2(f)? Such a component should pass all the signal power in the operation frequency band, according to Fig. 2.2(e), and exhibit a sharp phase rotation, and hence a group delay $[\tau(\omega) = |\partial\phi(\omega)/\partial\omega|]$ peak, at the center frequency ω_0, according to Fig. 2.2(f). The first requirement suggests a waveguide and the second a resonant delay element coupled to it. This leads to the structure shown in Fig. 2.3(a), which is composed of a straight

waveguide connecting the input (①) to the output (②) and coupling to a transmission-line loop resonator (③-④-③) with coupled section ③-④.

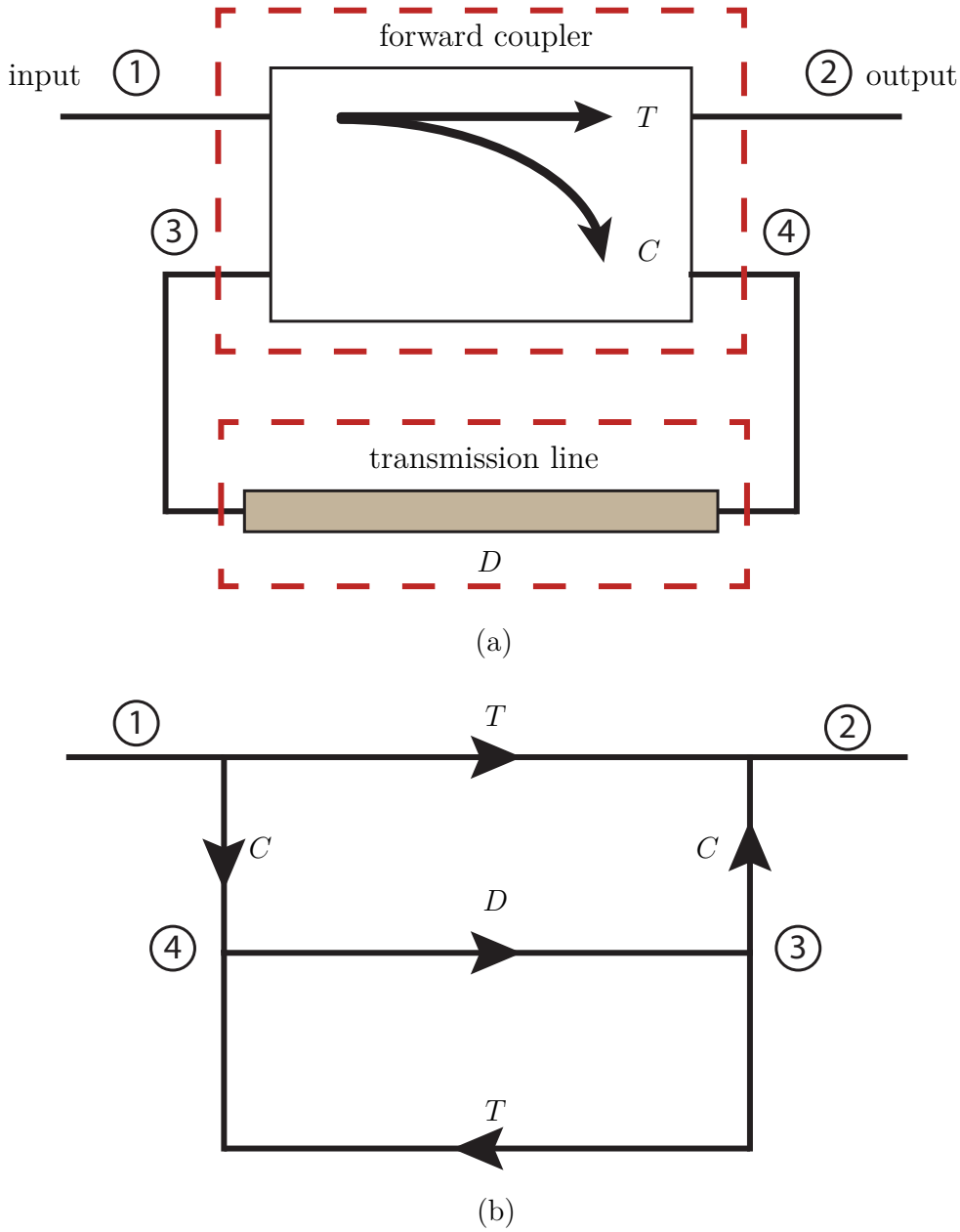

Figure 2.3 Typical implementation of a R-MSP Hilbert transformer. (a) Physical schematics. (b) Signal flow chart.

The structure of Fig. 2.3(a) may be modeled by the signal flow chart drawn in Fig. 2.3(b), where T and C, denote the transmission and coupling coefficients of the coupler, respectively, D denotes the transmission coefficient of the transmission-line loop, and where the coupler isolation is assumed to be infinite. Using standard flow-chart rules [63] yields then the transfer

function

$$S_{21} = T + \frac{C^2 D}{1 - TD}, \tag{2.7}$$

where T, C and D are complex quantities. Assuming that the coupler is passive, power conservation demands

$$|T|^2 + |C|^2 = 1. \tag{2.8}$$

Combining this magnitude relation with the phase relation

$$\angle C = \angle T - \frac{\pi}{2}, \tag{2.9}$$

anticipating the later use of a branch-line coupler [Fig. 2.7(b)], leads to complex relation

$$C^2 = T^2 - e^{j2\theta}, \tag{2.10}$$

where $\theta = \angle T$. Moreover, assuming that the transmission-line loop (minus the part common with the coupler section) is lossless and characterized by the time delay of the τ_0, we have

$$D = e^{-j\omega\tau_0}. \tag{2.11}$$

Substituting (2.10) and (2.11) into (2.7) finally yields the following expression for the transfer function of the Hilbert transformer as a function of the complex quantity T[1]:

$$S_{21}(\omega; T) = \frac{T - e^{-j(\omega_0\tau_0 - 2\theta)}}{1 - Te^{-j\omega\tau_0}}, \tag{2.12}$$

from which the system phase and group delay may be computed as

$$\phi(\omega; T) = \angle \left\{ S_{21}(\omega; T) \right\} \tag{2.13a}$$

and

$$\tau(\omega; T) = -\frac{\partial \phi(\omega; T)}{\partial \omega}, \tag{2.13b}$$

respectively.

If the coupled part of the loop is $\lambda/2$-long, or $\theta = \pi$, as will be the case with the final (cascaded double) branch-line coupler (Fig. 4.9), the shortest possible length of the uncoupled part of

[1]Later studies will investigate the response of the Hilbert transformer in terms of the coupling, which would suggest to express S_{21} as a function of C rather than T. However, it turns out that the latter expression is much more complicated than the former, while offering no specific benefit. For this reason, we have decided to give here S_{21} as a function of T, where $T = \sqrt{1 - |C|^2} e^{j(\angle C + \pi/2)}$ according to (2.8) ($|T| = \sqrt{1 - |C|^2}$) and (2.9) ($\angle T = \angle C + \pi/2$).

the transmission-line loop is $3\lambda/2$, or $\tau_0 = 3\pi/\omega_0$, corresponding to a 2λ resonant loop. Figures 2.4(a) and 2.4(b) plot the phase and group delay obtained by (2.13a) and (2.13b) for this scenario with center frequency $f_0 = \omega_0/(2\pi) = 10$ GHz. These results will be commented in Sec. 2.3 and physically explained in Sec. 2.5.

2.3 Transformer Characterization

As announced in Fig. 2.2(f) and verified in Fig. 2.4(a), the phase response of a R-MSP Hilbert transformer significantly departs from that of the ideal mathematical Hilbert transformer, plotted in Fig. 2.2(c): specifically, 1) the *asymptotic slopes* for $\omega \ll \omega_0$ and $\omega \gg \omega_0$ are *nonzero*, and 2) the *transition bandwidth* between the asymptotic slopes is *nonzero*.

In order to quantitatively characterize physical Hilbert transformers in terms of these two aspects, we define here related quantities, with the help of Fig. 2.5.

We define the *rotated phase* as the phase difference between the tangents to the phase curves at 80% and 120% of ω_0 (40% centered bandwidth), namely

$$\Delta\phi(|C|) = \phi(0.8\omega_0) - \phi(1.2\omega_0) + 0.4\omega_0 \left.\frac{d\phi(\omega)}{d\omega}\right|_{0.8\omega_0}, \tag{2.14}$$

which depends on the coupling level, $|C|$, according to Fig. 2.4.

Moreover, we define the *transition bandwidth*, which is also a function of $|C|$, as the symmetric band delimited by the frequencies ω_{L} and ω_{R} whose slopes depart by a factor α from the asymptotic slopes at 80% and 120% of ω_0, namely

$$\Delta\omega(|C|) = \omega_{\mathrm{R}} - \omega_{\mathrm{L}} = 2(\omega_0 - \omega_{\mathrm{L}}) = 2(\omega_{\mathrm{R}} - \omega_0), \tag{2.15a}$$

where ω_{L} and ω_{R} are defined via

$$\frac{\left.\frac{d\phi(\omega)}{d\omega}\right|_{\omega_{\mathrm{L}}} - \left.\frac{d\phi(\omega)}{d\omega}\right|_{0.8\omega_0}}{\left.\frac{d\phi(\omega)}{d\omega}\right|_{0.8\omega_0}} = \frac{\left.\frac{d\phi(\omega)}{d\omega}\right|_{\omega_{\mathrm{R}}} - \left.\frac{d\phi(\omega)}{d\omega}\right|_{1.2\omega_0}}{\left.\frac{d\phi(\omega)}{d\omega}\right|_{1.2\omega_0}} = \alpha. \tag{2.15b}$$

Note that the definitions (2.14) and (2.15) are not valid at the limit cases $C = 0$ and $|C| = 1$, as may be understood by inspecting Fig. 2.4(a).

Figure 2.6 plots the rotated phase and transition bandwidth versus coupling level. It shows that the rotated phase ($\Delta\phi$) is *inversely proportional* to the coupling level ($|C|$) while the

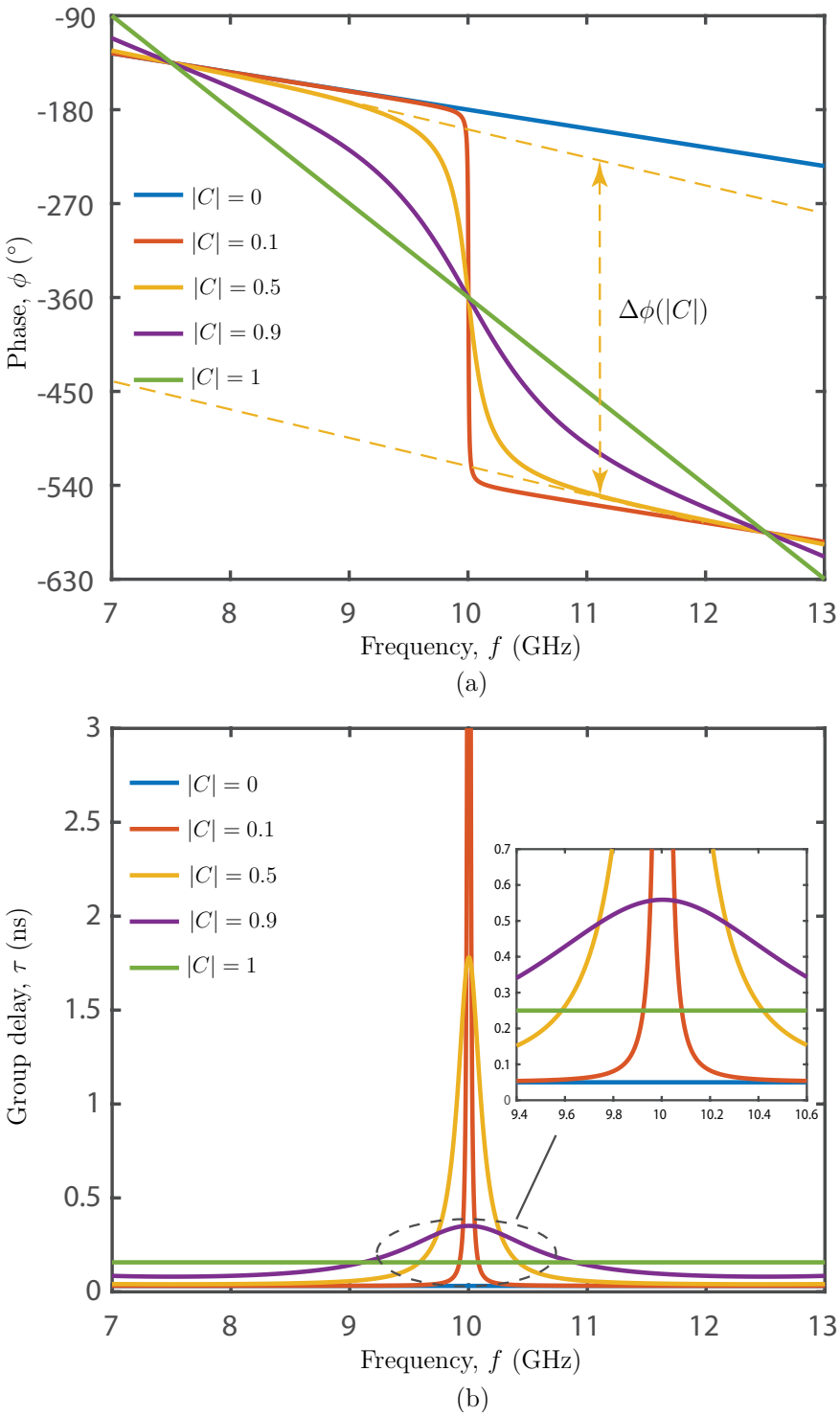

Figure 2.4 Frequency response of the R-MSP Hilbert transformer in Fig. 5.2 for different coupling coefficient magnitudes, $|C|$, and $f_0 = \omega_0/(2\pi) = 10$ GHz and $\tau_0 = 3\pi/\omega_0 = 0.15$ ns. (a) Phase [Eq. (2.13a)]. (b) Group delay [Eq. (2.13b)].

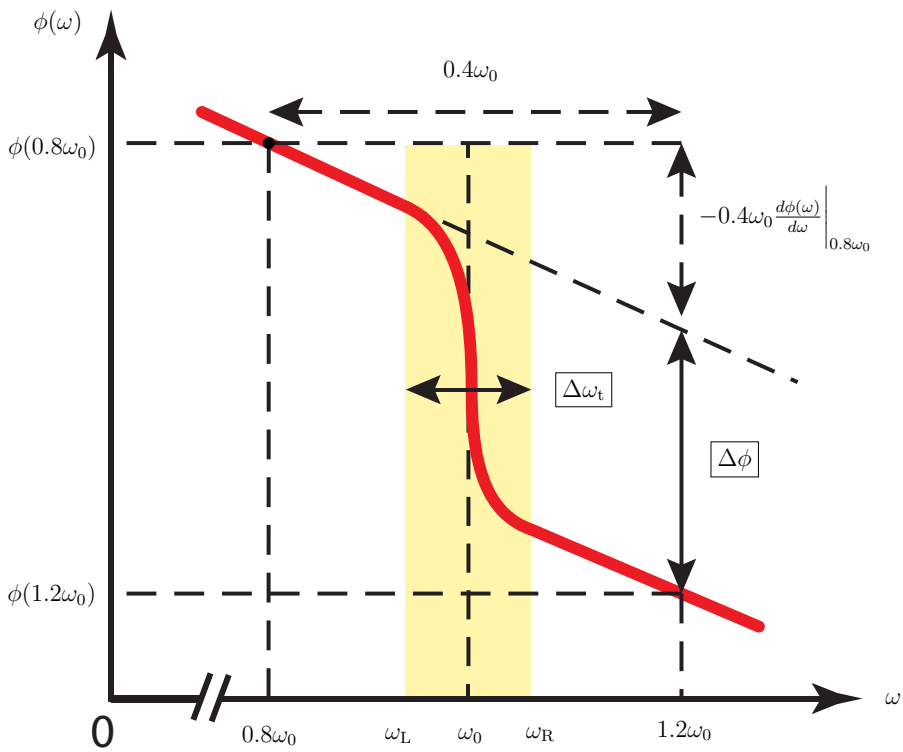

Figure 2.5 Characterization of the R-MSP Hilbert transformer in Fig. 5.2, corresponding to Fig. 2.2(f): rotated phase, $\Delta\phi$, and transition bandwidth, $\Delta\omega_t$.

transition bandwidth ($\Delta\omega_t$), being inversely proportional to the rotated phase, is *proportional* to the coupling level. This may be *mathematically* explained in terms of the group delay, plotted in Fig. 2.4(b): since the phase is the integral of the group delay [Eq. (2.13b)], the transition bandwidth (resp. rotated phase) is necessarily proportional (resp. inversely proportional) to the group delay bandwidth, and hence inversely proportional (resp. proportional) with the coupling level. The physical explanation of the observed group delay response will be provided in Sec. 2.5.

2.4 Microwave Implementation

Figure 2.6 shows that the 180° rotated phase needed for the R-MSP Hilbert transformer [Fig. 2.2(f)] would require a coupling coefficient of $|C| = 0.87$. Such a high coupling level is difficult to attain in microwave couplers. Moreover, also according to Fig. 2.6, it would lead to a relatively large – perhaps undesirably large - transition bandwidth.

To avoid these two issues, we propose to *cascade two identical couplers of lower coupling* (and hence also of smaller transition bandwidth) to realize the required total 180° rotated

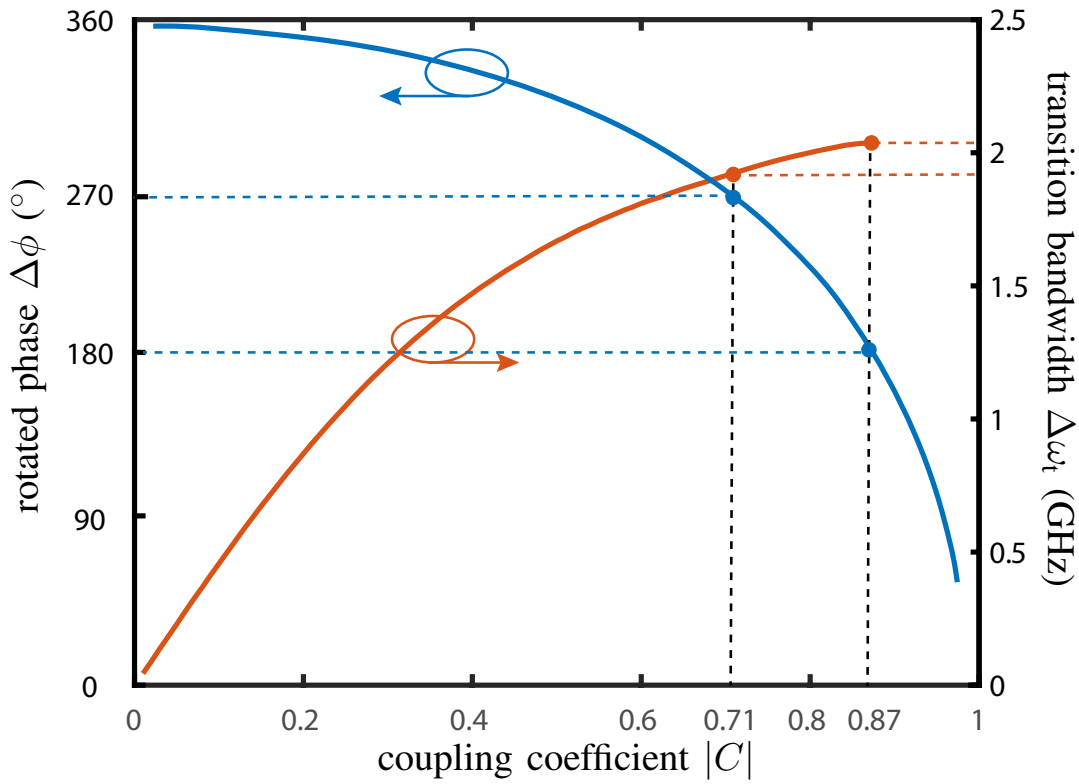

Figure 2.6 Rotated phase [Eq. (2.14)] and transition bandwidth [Eq. (2.15) with $\alpha = 0.35$] versus coupling magnitude $|C|$, for the same parameters as in Fig. 2.4.

phase. Specifically, we choose a single-coupler rotated phase of 270°, corresponding to a total rotated phase of $2 \times 270° = 540°180°$. This, according to Fig. 2.6 corresponds to a coupling coefficient of $|C| = 0.71$, associated with a transition bandwidth that is narrower than that associated with $|C| = 0.87$.

The largest coupling bandwidths at microwaves are provided by coupled-line couplers. However, these couplers are restricted to low coupling levels, typically substantially smaller than 3-dB. Therefore, we decide to use here a *branch-line coupler* [63], whose coupling level of $|C| = 1/\sqrt{2} = 0.707 \approx 0.71$ is the most commonly used in practice.

Figure 2.7 shows the corresponding layout composition for a *single unit*, with the input-output connections, the branch-line coupler itself, the loop resonator and the assembly of the last two given in Figs. 5.2(a), 5.2(b), 5.2(c) and 5.2(d), respectively.

As explained above, the single-unit assembly in Fig. 2.7(d) will be designed to provide a 270° rotated phase, and two such units will be cascaded to achieve the required $2 \times 270° = 540°180°$ rotated phase. However, the relative bandwidth of a branch-line coupler is typically in the order of 15% [63] while the transition bandwidth for the selected coupling level ($|C| = 0.71$)

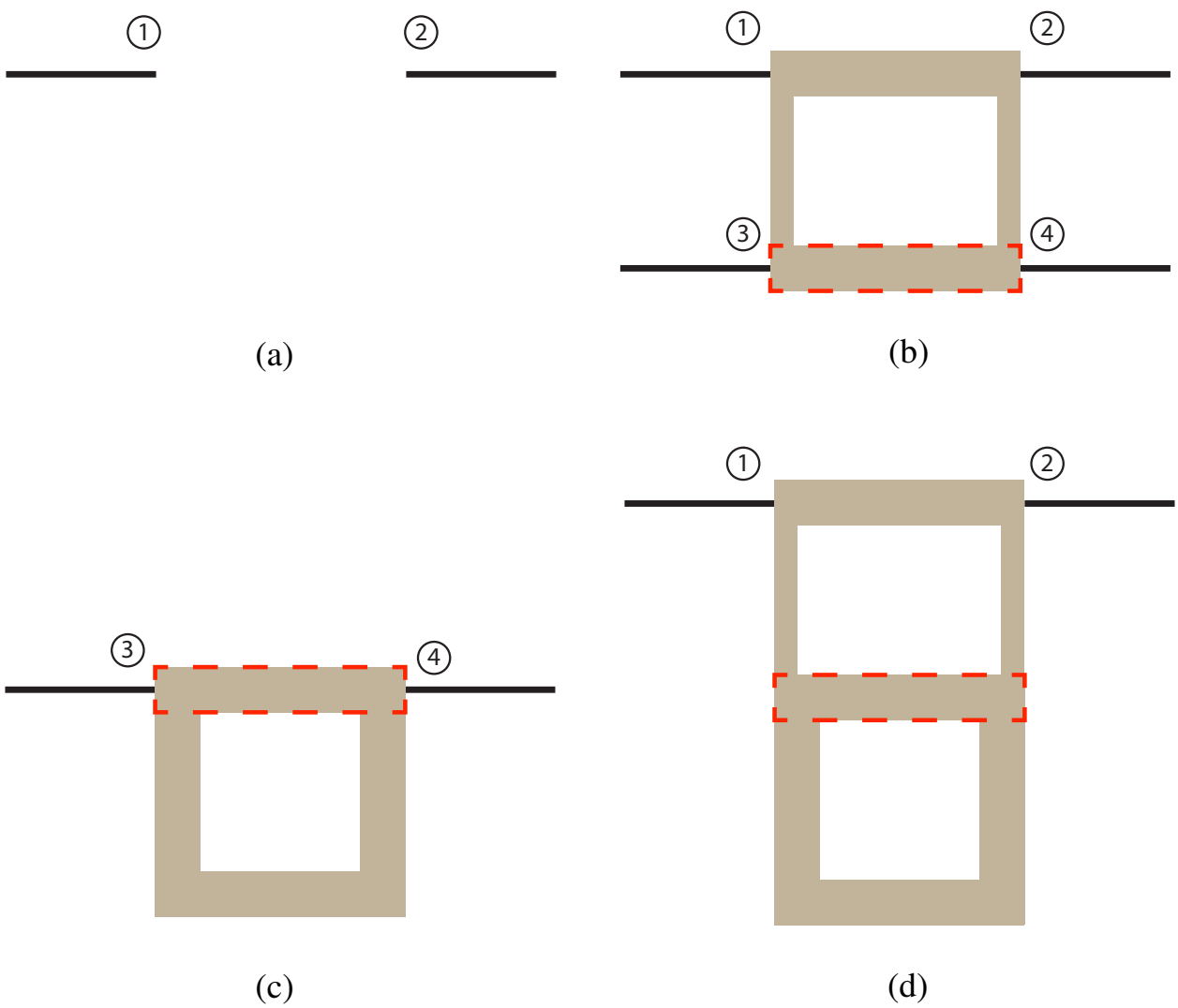

Figure 2.7 Assembly of a unit of the proposed microwave R-MSP Hilbert transformer. (a) Input and output ports. (b) Branch-line coupler. (c) Loop resonator. (d) Assembly. The transmission-line sections within the red boxes in (b) and (c) are merged together in (d).

is of around 20%, according Fig. 2.6. Therefore, we replace the single-section branch-line coupler by a double-section branch-line coupler [63]. Figure 2.8 shows the layout of the overall proposed R-MSP microwave Hilbert transform with its two cascaded units including each a double-section branch-line coupler.

If one wishes to enhance the TBP of the Hilbert transformer, one may, as seen in (2.5), either increase the operating bandwidth ($\Delta\omega$) or decrease the π-transition bandwidth ($\Delta\omega_{\mathrm{t}}$). The former mainly depends on the bandwidth of the coupler, and a multi-section alternative of the coupler would therefore increase it. The latter can be reduced by cascading more

than two sections of the structure in Fig. 2.7(d) with smaller coupling coefficient. Both transformations naturally lead to larger physical size and larger loss.

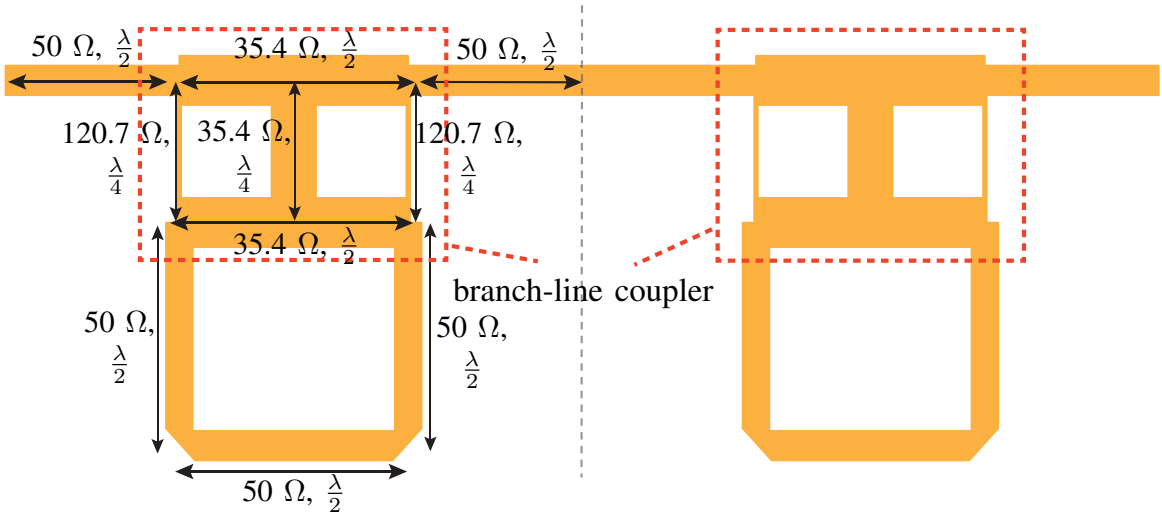

Figure 2.8 Layout of the proposed R-MSP microwave Hilbert transformer, composed of two cascaded units of 270° rotated phase including each a double-section branch-line coupler.

2.5 Physical Explanation

Section 2.2 derived the transfer function and plotted the phase and group delay responses of the R-MSP Hilbert transformer, while Sec. 2.3 characterized the corresponding rotated phase and transition bandwidth responses in term of the coupling level, pointing out how the device response is related to the group delay versus coupling response. This section will provide the physical explanation of this group delay response – and specifically the decrease of the group delay peak $\tau(\omega_0) = \tau_0$ versus coupling level $|C|$, plotted in Fig. 2.9 – for microwave implementations of the type proposed in Sec. 2.3, using both a steady-state regime and a transient regime perspectives.

2.5.1 Steady-State Regime

Table 2.1 compares the steady-state harmonic regime operation of the R-MSP Hilbert transformer at the four different coupling levels indicated in Fig. 2.9. Let us consider these four cases one by one.

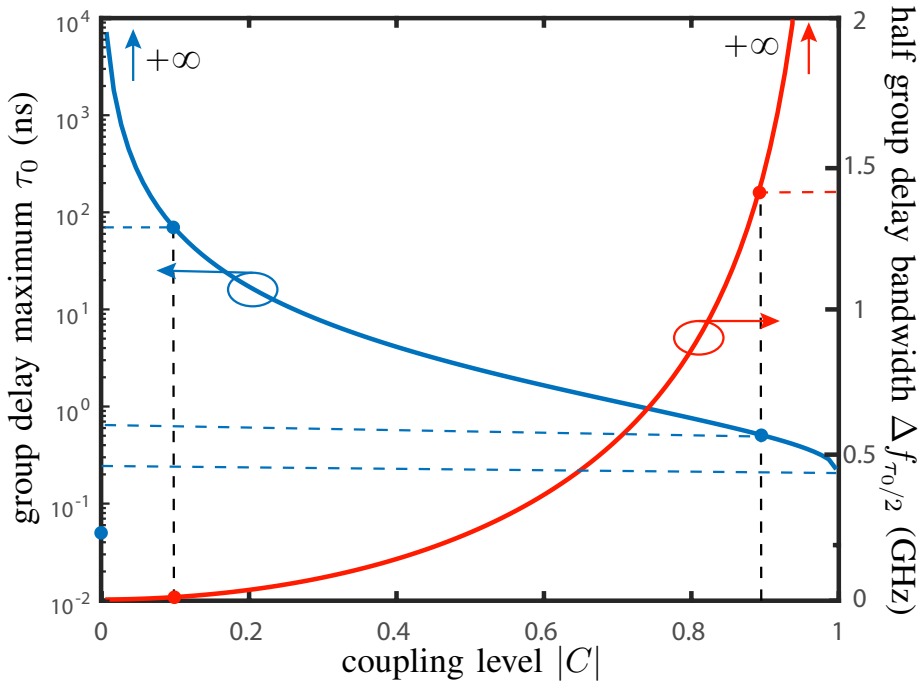

Figure 2.9 Group delay maximum, $\tau(\omega_0) = \tau_0$ (log scale), and half group delay bandwidth, $\Delta f_{\tau_0/2}$ versus coupling level $|C|$.

$C = 0$

This is a very particular case, where the resonant loop brutally becomes invisible (or infinitely far), so that the transformer structure degenerates into a simple straight transmission line. As a result, and according to (2.7), $S_{21}(C = 0) = T$, and hence the group delay is $\tau_0 = (\lambda/2)/(\lambda f_0) = 1/(2f_0) = 0.05$ ns (constant). The bandwidth is naturally infinite, assuming an ideal transmission line.

$|C| = 0.1$

As soon as $C \neq 0$, the system recovers its coupled resonator, and therefore behaves completely differently. Figure 2.9 shows that $\lim_{|C|\to 0} \tau_0 = \infty$. Why is this the case? If $|C|$ is nonzero but very small, a small amount of energy per harmonic cycle (1% for $|C| = 0.1$) couples into the resonant loop, but an even smaller amount of energy (1% of the remainder for $|C| = 0.1$) couples out at each turn, so that most of the coupled energy loops in the resonator for a very long time, hence yielding a very high group delay ($1558\tau_0 = 79.4$ ns for $|C| = 0.1$). Moreover, the bandwidth is very narrow because the resonator is seen by the straight transmission line as a lossy load with loss proportional to coupling, leading to an effective quality factor inversely

Table 2.1 Steady-state explanation for the group delay response of the R-MSP Hilbert transformer.

	Case 1: $\lvert C\rvert = 0$	Case 2: $\lvert C\rvert = 0.1$
wave flow		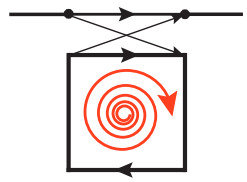
group delay	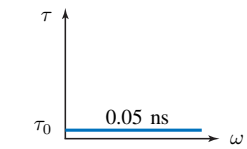	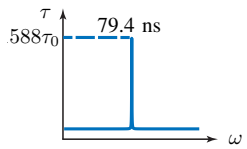
	Case 3: $\lvert C\rvert = 0.9$	**Case 4: $\lvert C\rvert = 1$**
wave flow	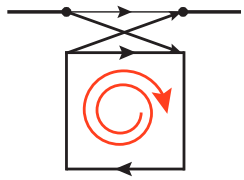	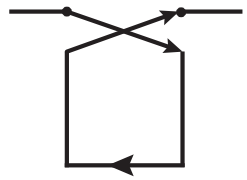
group delay	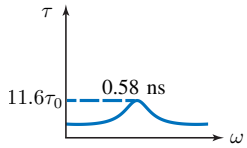	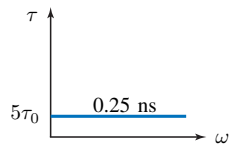

proportional to the coupling level, i.e. $Q \propto 1/\Delta\omega \propto 1/|C|$.

$|C| = 0.9$

At large coupling levels, most of the energy (81% for $|C| = 0.9$) of each harmonic cycle is coupled into the resonant loop, but a lot of energy is still coupled out of it (66% after the first turn for $|C| = 0.9$), so that most of the energy is mostly evacuated after a small number of turns in the loop, yielding a much smaller group delay ($11.6\tau_0 = 0.58$ ns for $|C| = 0.9$). At the same time, the quality factor of the system, $Q \propto 1/|C|$, is now much smaller, and therefore the group delay bandwidth is strongly increased.

$|C| = 1$

In contrast to $C = 0$ with $|C| \to 0$, the case $|C| = 1$ is in continuity with $|C| \to 1$. As $|C| \to 1$, the effect of the straight line gradually diminishes and exactly disappears at$|C| = 1$, where the harmonic cycle energy performs exactly one turn in the loop, corresponding to a constant delay of $5\tau_0 = 0.25$ ns, again with infinite bandwidth.

2.5.2 Transient Regime

The steady-state harmonic regime is most informative, as it corresponds to the operation regime of the R-MSP Hilbert transformer. However, it is somewhat difficult to apprehend the notion of group delay for a continuous wave, since such a wave has neither beginning nor end. Therefore, we offer here an alternative perspective, the transient harmonic regime perpspective, where a continuous wave of frequency ω_0 is injected into the system at time $t = 0$.

Figure 2.10 shows the full-wave simulated evolution of this wave into a simplified (single section with mono-section branch-line couplers) version – for easier visualization – of the microwave Hilbert transformer in Fig. 2.8 for two different coupling levels. In both cases, one sees that the energy first gradually penetrates into the structure, loads the resonant loop, and finally reaches the steady-state regime. However, it is observed – particularly by inspecting the output branch of the structure — that the steady-state regime is reached later in the low-coupling transformer and earlier in the high-coupling transformer. Moreover, the time taken by the harmonic wave to reach the steady state is found to be close to the simulated group delay, taken here as the maximal delay (τ_0). This time corresponds indeed to the transmission time of a harmonic-wave "packet" within the observation time, and is hence an an excellent proxy for the group delay.

2.6 Experiment Demonstration

Figure 2.11(a) shows a fabricated X-band R-MSP Hilbert transformer prototype with the design and dimensions given in Fig. 2.8. It is fabricated on a Rogers 6002 substrate with thickness 0.508 mm and dielectric constant 2.94, and microstrip line sections of impedances 35.4 Ω, 50 Ω and 120.7 Ω corresponding to the widths 2.11 mm, 1.25 mm, and 0.20 mm, respectively (λ_{eff} =8.19 mm at 10 GHz). The corresponding magnitude and phase responses are plotted in Figs. 2.11(b) and 2.11(c), respectively. The simulated and measured results are in fair agreement with each other. The passband extends from 7.8 GHz to 12.2 GHz, except for a notch at the center frequency, 10 GHz. This notch is due to the losses of the

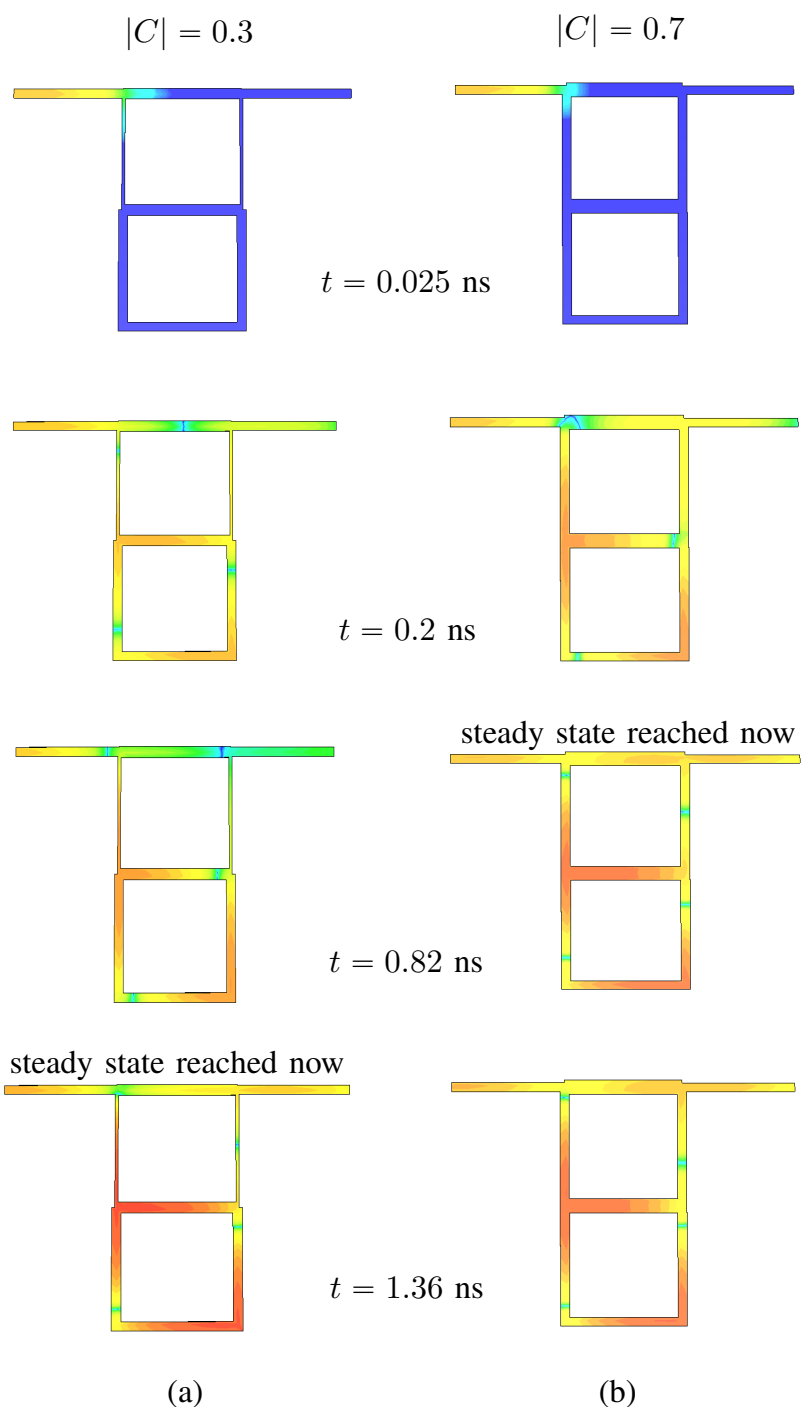

Figure 2.10 Transient full-wave explanation performed with the CST Studio Suite for the group delay in a R-MSP Hilbert transformer. (a) Small coupling coefficient, $|C| = 0.3$, corresponding to large group delay of $\tau_{\text{sim.}} = 0.83$ ns. (b) Large coupling coefficient, $|C| = 0.7$, corresponding to small group delay of $\tau_{\text{sim.}} = 1.30$ ns.

material and microstrip line radiation, which are naturally maximal at the frequency, where energy is stored in the structure for the longest time (group delay peak), i.e. the resonance frequency. However, if no energy is injected in its frequency range, this notch does not pose any practical problem. Table 2.2 compares the proposed Hilbert transformer implementation with previous designs.

Table 2.2 Comparison of Hilbert transformer implementation between previous and our design

Ref.	operating domain	TBP	cost	size
[61]	digital	unlimited	medium	small
[54–60]	optical	large	high	large
our work	microwave	small	low	small

2.7 Applications

In order to illustrate the usefulness of the proposed microwave R-MSP Hilbert transformer, we present here three applications of it. In each case, the results have been obtained by applying the scattering matrix of the experimental prototype of Fig. 2.11 to the test signals.

2.7.1 Edge Detection

The Hilbert-transformer is essentially an *edge detector*, and can thus be used for instance to increase contrast in image processing or enhance the signal-to-noise ratio in differential-modulation communication schemes.

The detection operation can be mathematically demonstrated by convolving the input rectangular pulse

$$x(t) = \Pi(t) = \begin{cases} 1, & \text{if } |t| \leq 1, \\ 0, & \text{if } |t| > 1 \end{cases} \tag{2.16}$$

with the impulse function $h(t)$ in (2.1), according to the definition (2.2), which yields

$$\begin{aligned} y(t) =& \frac{1}{\pi}\mathcal{P}.\mathcal{V}.\int_{-\infty}^{+\infty} \Pi(\tau)\frac{1}{t-\tau}d\tau = \frac{1}{\pi}\mathcal{P}.\mathcal{V}.\int_{-1}^{1}\frac{1}{t-\tau}d\tau \\ =& \frac{1}{\pi}\mathcal{P}.\mathcal{V}.\int_{t+1}^{t-1}\frac{1}{u}d(-u) \quad (\text{substitution } u = t-\tau) \\ =& -\frac{1}{\pi}\ln|u|\Big|_{t+1}^{t-1} = \frac{1}{\pi}\ln\left|\frac{t+1}{t-1}\right| = \mathcal{H}[\Pi(t)]. \end{aligned} \tag{2.17}$$

Figure 2.12 plots both (2.16) and (2.17), and clearly shows the announced edge detection

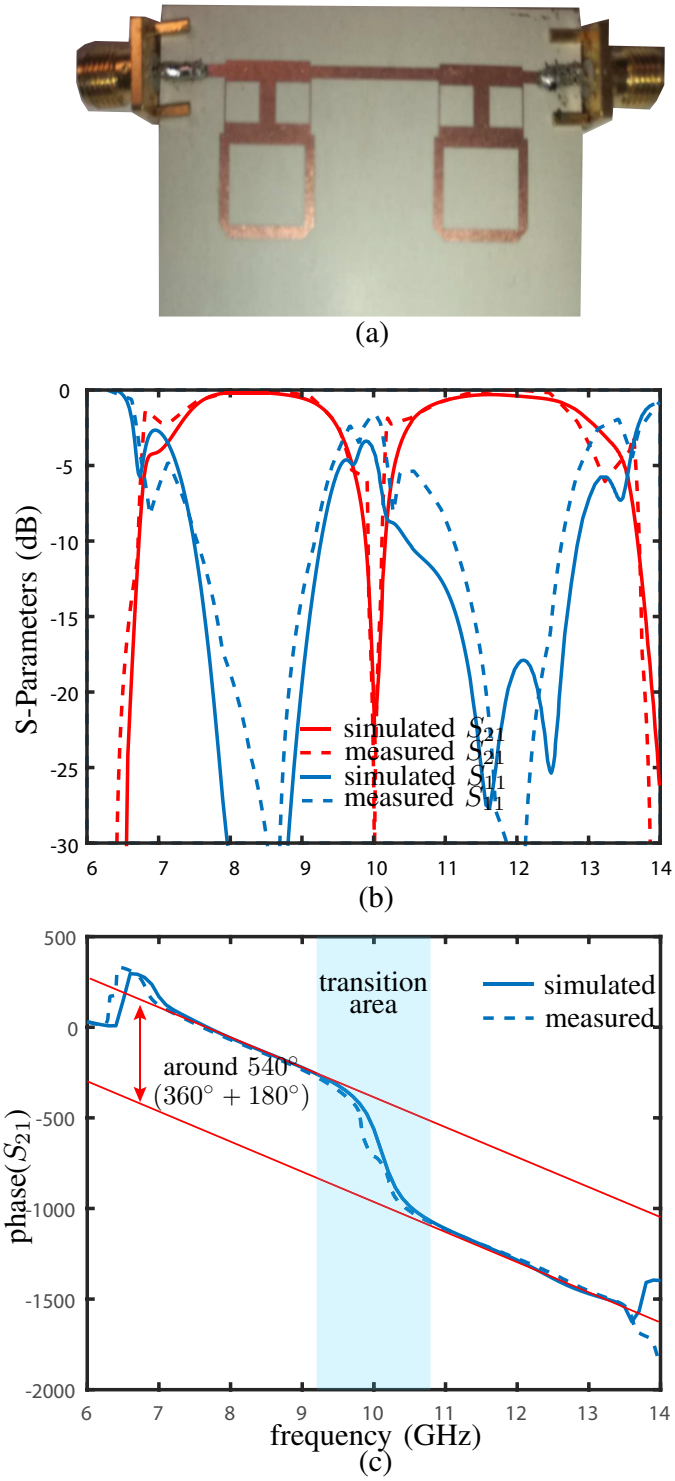

Figure 2.11 Experiment demonstration of proposed R-MSP Hilbert transformer. (a) Prototype. (b) Simulated and measured S-parameters. (c) Phase response.

effect, associated with the poles of (2.17) at $t = \pm 1$.

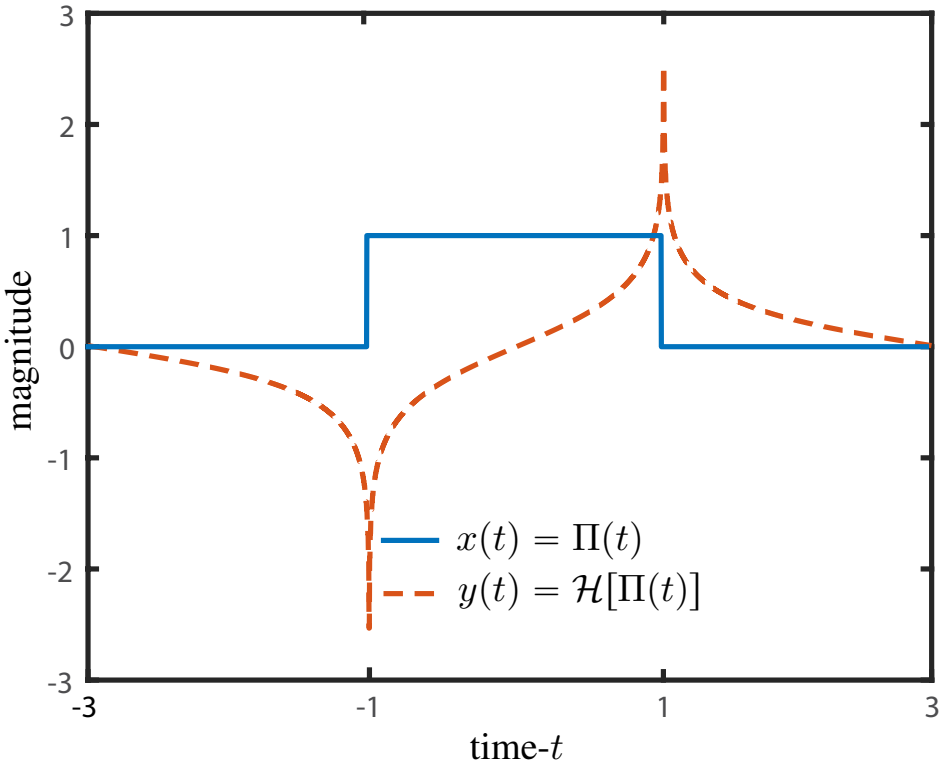

Figure 2.12 Hilbert transform of a square pulse [Eqs. (2.16) and (2.17)].

Figure 2.13 offers an intuitive explanation for the edge detection just mathematically demonstrated. The pulse function $x(t) = \Pi(t)$ may be constructed as a continuous superposition of Dirac functions across the duration of the pulse, as suggested in Fig. 2.13(a), since $\Pi(t) = \Pi(t) * \delta(t) = \int_{-1}^{1} \delta(t - t')dt'$. But one knows from (2.2) that $y(t) = h(t)$ [Eq. (2.1)] for $x(t) = \delta(t)$. Therefore, by superposition (linearity), the response $y(t)$ is the (continuous) sum of the functions $h(t - t')$ with $t' \in [-1, 1]$. Since $h(t - t')$ is odd, the signal within the range vanishes due to mutually canceling opposite branches of h, and only the edge branches remain, as shown in Fig. 2.13(b), consistently with Fig. 2.12.

Figure 2.14(b) shows the response of the R-MSP Hilbert transformer in Fig. 2.11 to the modulated periodic rectangular pulse train in Fig. 2.14(a). Since, in contrast to the case of Fig. 2.13, the pulse is modulated, the detected edges have no specific polarity, but the experiment perfectly shows the edge detection operation of the Hilbert transformer.

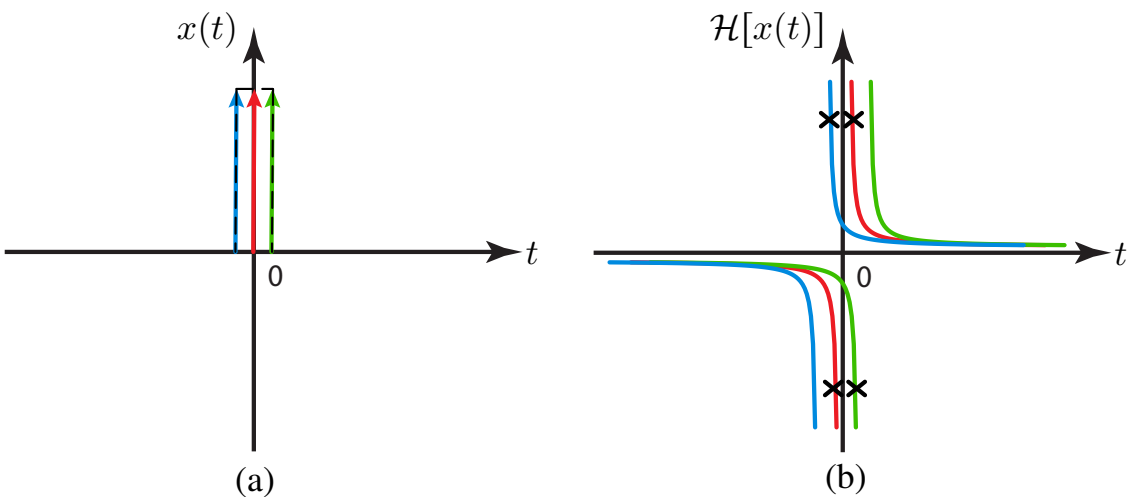

Figure 2.13 Intuitively explanation of the square pulse edge detection in Fig. 2.12. (a) Input signal rectangular pulse $x(t) = \Pi(t)$ expressed as a (continuous) superposition of Dirac functions. (b) Formation of the Hilbert transform of (a) using the fact that $y(t) = h(t)$ [Eq. (2.1)] for $x(t) = \delta(t)$.

2.7.2 Peak Clipping

The Hilbert-transformer is also a *peak clipper*, and can thus be used as a peak-to-average ratio reducer in radar and switched power amplifiers, where the peak information can be recovered by a second Hilbert transformation, according to (2.6). The clipping effect naturally exists in Fig. 2.12, where the center of the rectangular pulse is mapped onto zero, but the effect is not very significant there due to the flatness of the pulse.

To better appreciate it, let us consider the triangular input signal

$$x(t) = \mathrm{tri}(t) = \begin{cases} t+1, & \text{if } -1 \le t < 0, \\ -t+1, & \text{if } 0 \le t \le 1, \\ 0, & \text{otherwise.} \end{cases} \tag{2.18}$$

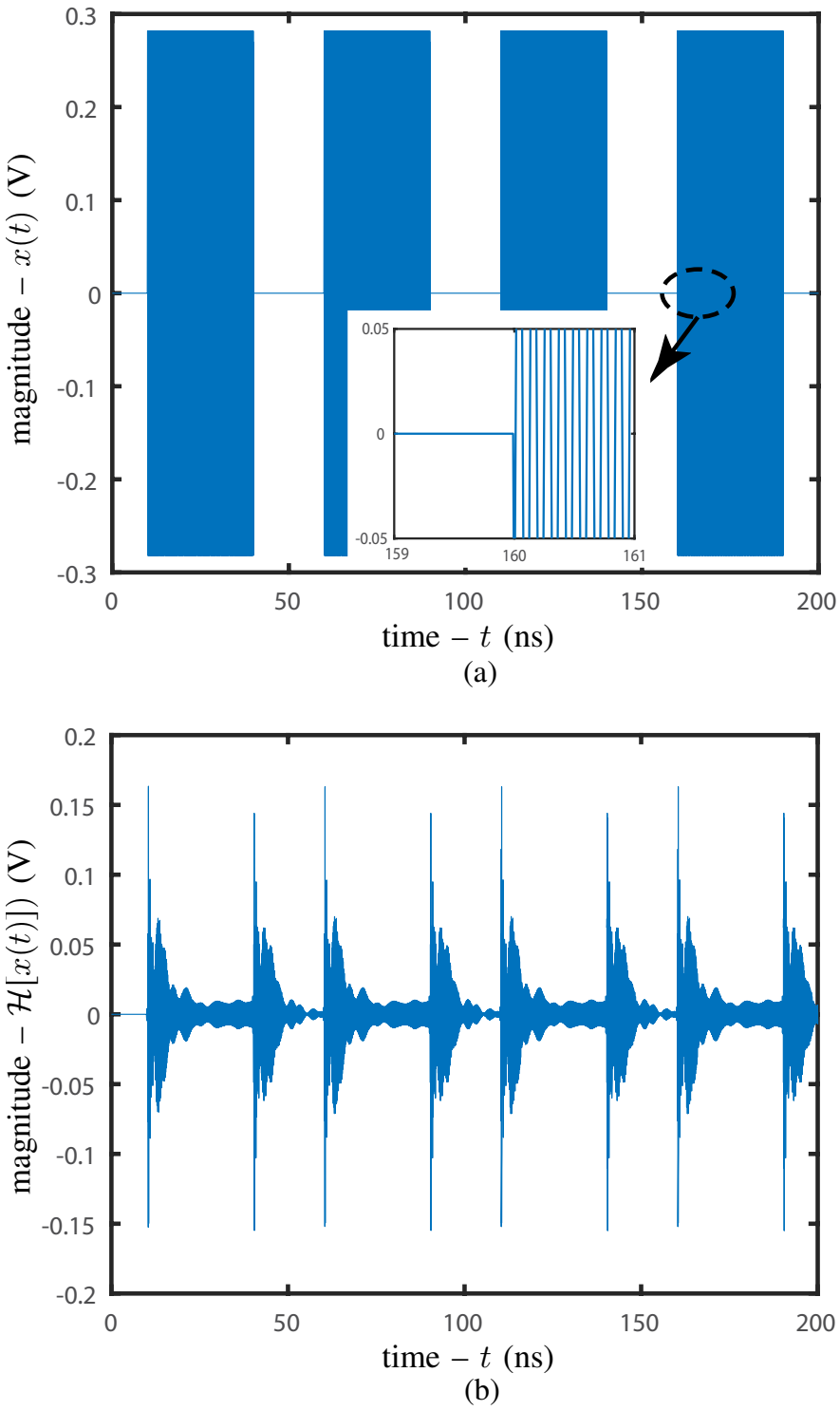

Figure 2.14 Edge detection verification for the R-MSP Hilbert transformer in Fig. 2.11. (a) Input rectangular pulse train modulated at $f_0 = 10$ GHz. (b) Output signal with edge detection.

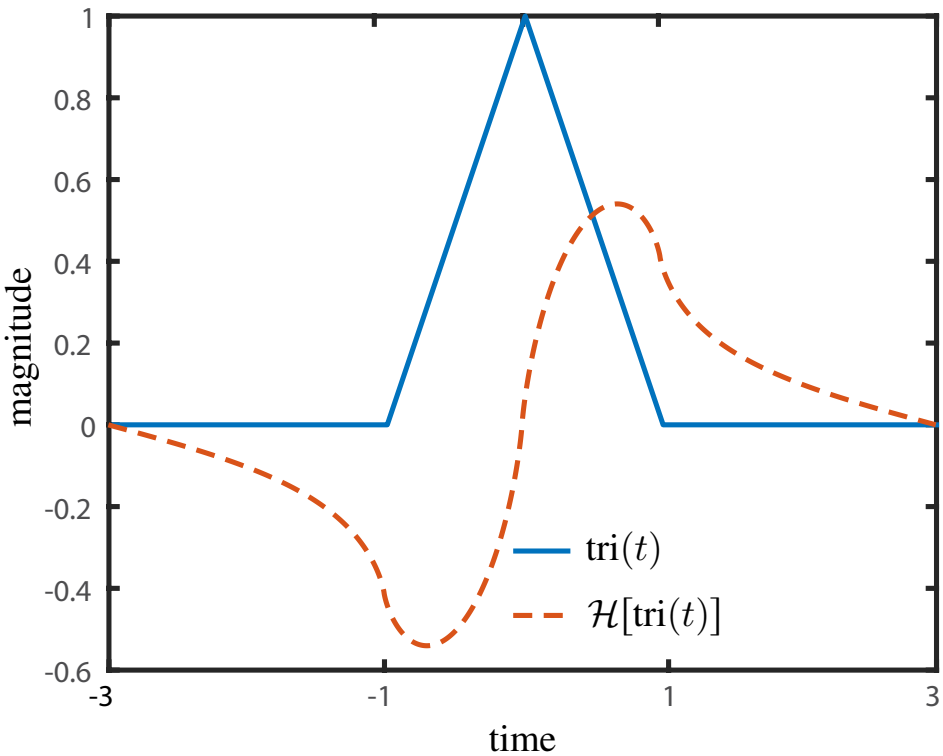

Figure 2.15 Hilbert transform of a triangular pulse [Eqs. (2.18) and (2.19)].

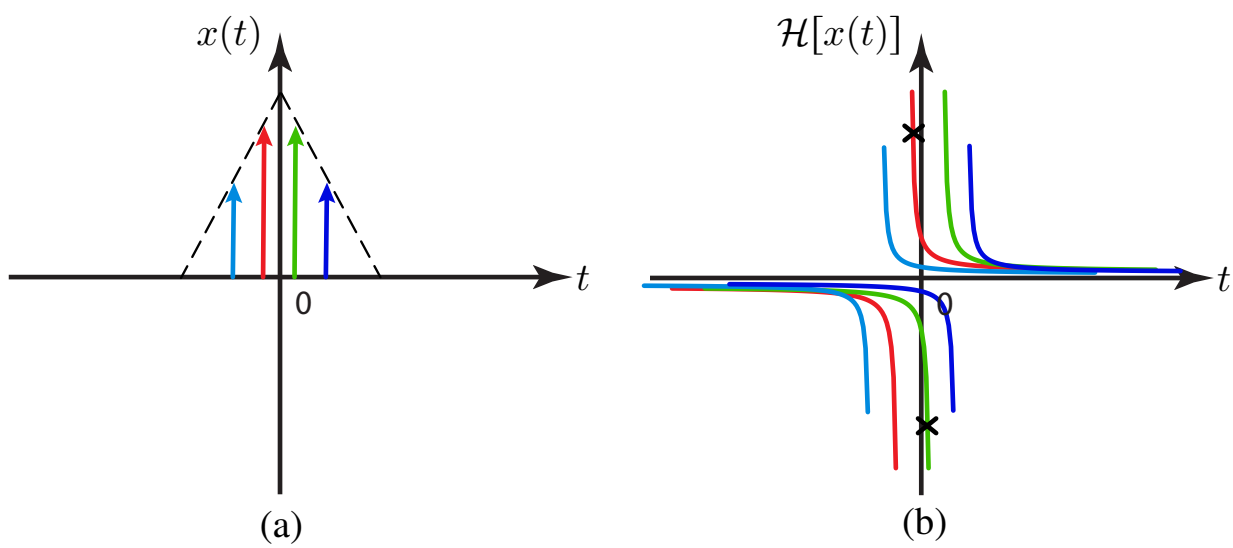

Figure 2.16 Intuitively explanation of the triangular pulse peak suppression in Fig. 2.15. (a) Input signal triangular pulse $x(t) = \text{tri}(t)$ expressed as a (continuous) superposition of triangularly weighted Dirac functions. (b) Formation of the Hilbert transform of (a) using the fact that $y(t) = h(t)$ [Eq. (2.1)] for $x(t) = \delta(t)$.

Computing the mathematical Hilbert transform of this function yields

$$
\begin{aligned}
y(t) =& \frac{1}{\pi}\mathcal{P}.\mathcal{V}.\int_{-\infty}^{+\infty} \mathrm{tri}(\tau)\frac{1}{t-\tau}d\tau \\
=& \frac{1}{\pi}\left(\mathcal{P}.\mathcal{V}.\int_{-1}^{0}\frac{\tau+1}{t-\tau}d\tau + \mathcal{P}.\mathcal{V}.\int_{0}^{1}\frac{-\tau+1}{t-\tau}d\tau\right) \\
=& \frac{1}{\pi}\left(\mathcal{P}.\mathcal{V}.\int_{-1}^{0}\frac{t+1}{t-\tau}d\tau - \int_{-1}^{0}1d\tau\right. \\
& \qquad\qquad \left. +\mathcal{P}.\mathcal{V}.\int_{0}^{1}\frac{1-t}{t-\tau}d\tau + \int_{0}^{1}1d\tau\right) \\
=& \frac{1}{\pi}\left(\mathcal{P}.\mathcal{V}.\int_{t+1}^{t}\frac{t+1}{u}d(-u) + \mathcal{P}.\mathcal{V}.\int_{t}^{t-1}\frac{1-t}{u}d(-u)\right) \\
=& -\frac{1}{\pi}\left((t+1)\ln\left|\frac{t}{t+1}\right| + (1-t)\ln\left|\frac{t-1}{t}\right|\right) \\
=& -\frac{1}{\pi}\left(\ln\left|\frac{t-1}{t+1}\right| + \frac{t}{1}\ln\left|\frac{t^2}{t^2-1}\right|\right) = \mathcal{H}[\Pi(t)],
\end{aligned}
\tag{2.19}
$$

which maps $x(0)$ into $y(0)$, and thus indeed suppresses the peak value, as shown in Fig. 2.15. Figure 2.16 intuitively explains the peak suppression produced by the Hilbert transformer, following the same logics as for edge detection.

Figure 2.17(b) shows the response of the R-MSP Hilbert transformer in Fig. 2.11 to the modulated periodic triangular pulse train in Fig. 2.17(a). Again, the response exhibits no specific polarity due to its modulated nature, but the experiment perfectly shows the peak suppression operation of the Hilbert transformer. Finally, Fig. 2.17(c) shows the response of the waveform of Fig. 2.17(b) after a second R-MSP Hilbert transformer has been cascaded to the structure in Fig. 2.11. Despite small notches, due to imperfect 3-π phase separation, and amplitude reduction due to the magnitude dip at the center frequency (Fig. 2.11), it is getting reasonably close to the initial triangular signal of Fig. 2.17(a), as expected.

2.7.3 Single-Sideband (SSB) Modulation

The Hilbert transformer may be combined with a delay line to provide a single side-band (SSB) modulator, as shown in Fig. 2.18. In this application, the transformer center frequency is set at the middle of the two initial sidebands. It reverses the sign of one of the two sidebands and combines the result with a delayed copy of the input signal, as shown in the figure, which results in the suppression of the undesired sideband. The effect is identical to that of a low-pass (lower SSB) or high-pass (upper SSB) filter, but this implementation allows much easier SSB switching by simply tuning the length of the transmission line using a U-shaped detour loaded by a PIN diode.

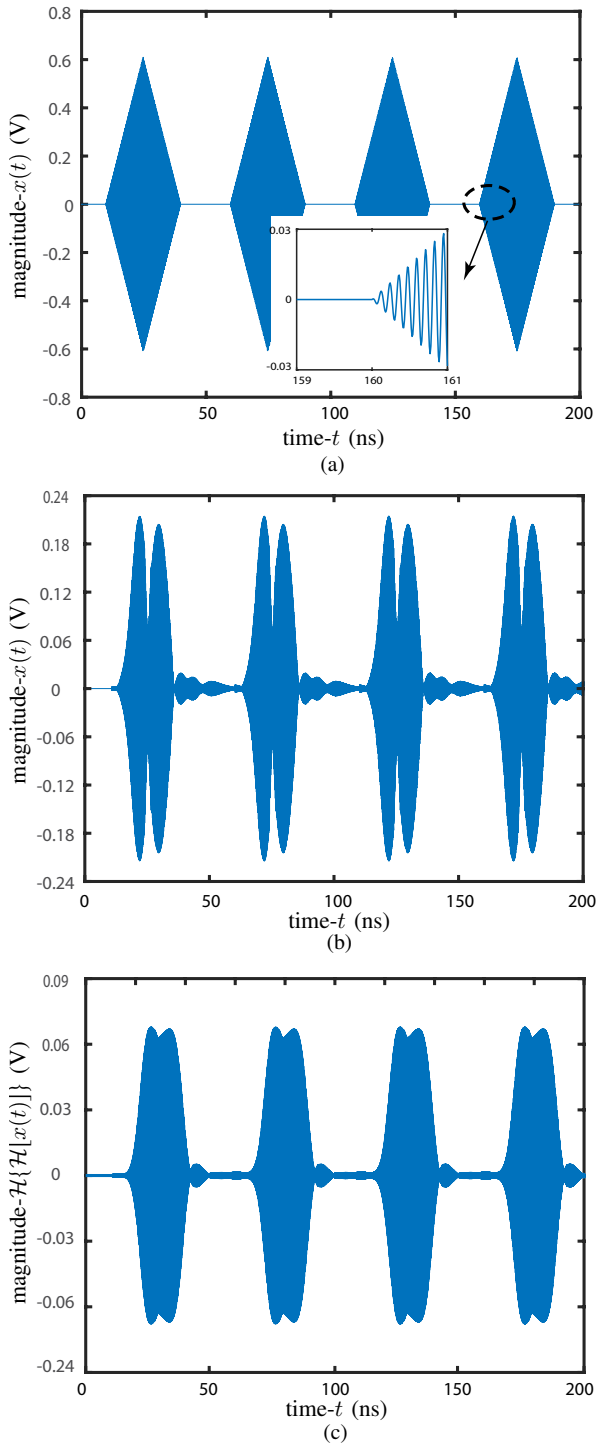

Figure 2.17 Peak suppression verification for the R-MSP Hilbert transformer in Fig. 2.11. (a) Input triangular pulse train modulated at $f_0 = 10$ GHz. (b) Output signal with peak suppression. (c) peak recovered output signal after a second Hilbert transformer.

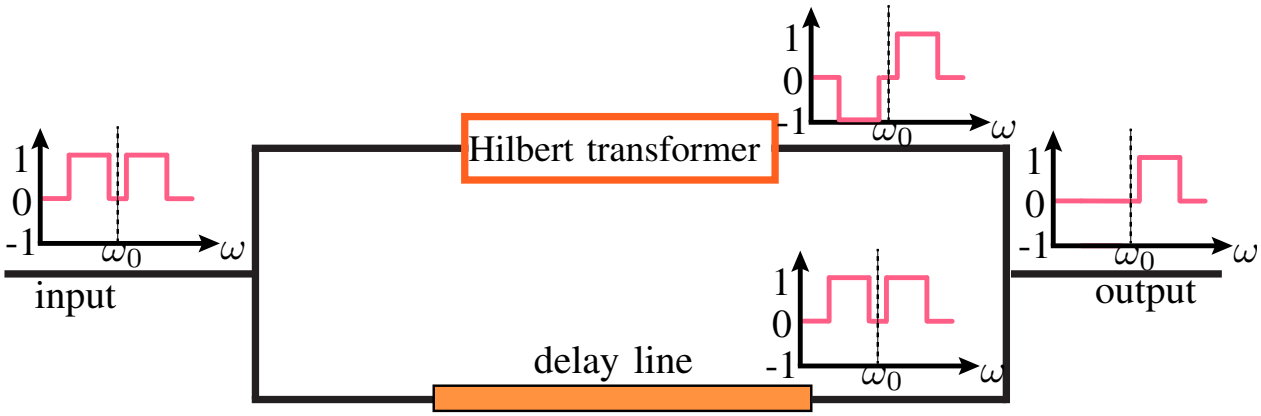

Figure 2.18 Schematic of a SSB modulation based on a R-MSP Hilbert transformer.

The response of the Hilbert transformer based SSB modulator is experimentally demonstrated in Fig. 2.19. The parallel combination of the Hilbert transformer and of the delay line in Fig. 2.18 results in a a high-pass response. This response includes a few dips in the Hilbert-transformer transition band, whereas one may a priori exact a smooth transition. These dips may be understood by examining the phase transition in Fig. 2.11: this specific design does not feature a π phase difference but an equivalent 3π one, which leads to double alternance between destructive and constructive interference between the Hilbert transformer and delay line paths. The sideband switching operation is trivial and is hence not presented here.

2.8 Conclusion

A microwave Hilbert transformer, based on the combination of a branch-line coupler and a loop resonator, has been introduced, characterized, physically explained, and applied to edge detection, peak suppression and single side-band modulation. The device represents a new component for Real-time Microwave Analog Processing, and is hence expected to help the development of this technology in the forthcoming years.

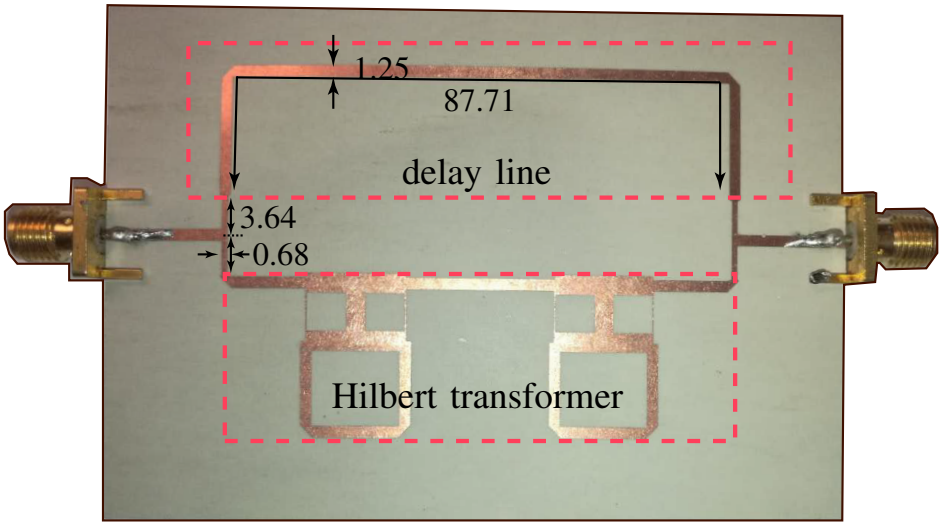

(a)

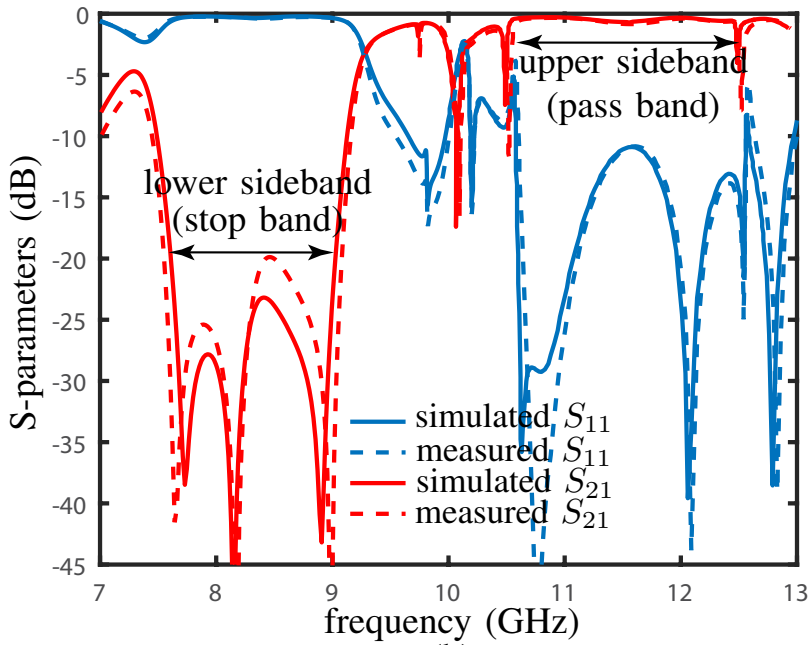

(b)

Figure 2.19 Experiment demonstration of a SSB modulator based on a R-MSP Hilbert transformer. (a) Fabricated prototype (all values are in mm), for upper SSB operation. (b) Simulated and measured high-pass filtering S-parameters.

CHAPTER 3 ROTMAN LENS BASED SPECTRUM DECOMPOSITION

Spectral Decomposition (SD) is a fundamental optical process according to which white light is spatially split into its constituent frequencies. It is widely found in natural phenomena, such as in rainbows, which are caused by the interplay of reflection, refraction and dispersion of light in water droplets [64], or in soap bubbles and gas spills, which are caused by interferences due thin film thickness gradients [65]. It is also produced by human-made devices, such as prisms and diffraction gratings [66,67], and may be achieved in any part of the electromagnetic spectrum. SD devices are used in various applications, including colorimetry [68], real-time spectrum analysis [69], laser wavelength tuning [70, 71], filtering [72, 73], wavelength division multiplexing [74, 75], and antenna array beam forming [76].

Most of the conventional SD devices are based on prisms and diffraction gratings, which are three-dimensional components that are bulky, expensive and incompatible with integrated circuit technology. The availability of two-dimensional, or planar, implementations would resolve these issues and hence dramatically widen the range of applications of SD. Several efforts have been dedicated to realize planar SD devices, particulary using lumped-element structures [77,78] and leaky-wave antennas [69,79]. The most practical attempt has probably been the SD reported by Zhang and Fusco [16], which transforms the beam forming operation of a Rotman lens (RL) into an SD operation using a reflecting transmission line array, where the reflecting transmission line array plays the same role as the optical fibers at the center of a conventional array waveguide grating (AWG) [80], i.e. assigning different phase gradients to the different frequencies composing the spectrum of the signal to analyze.

In [16], the emphasis was on generating orthogonal spectrally decomposed waveforms. It uses the same port distribution as in the conventional Rotman lens beam former, which leads to a non-uniform spectrum resolution, and does not provide any information on how to achieve an other type of results. In this chapter, we enhance the SD capability of the RL-SD in terms of resolution flexibility, input port position arbitrariness and frequency-range tunability, by manipulating the output port locations, inserting a calibration array and introducing port switching, respectively. With all such enhancements, the RL-SD becomes a promising device for integrated systems involving real-time spectrum analysis. Part of this chapter is excerpted from the author's works [13, 46–48].

3.1 Proposed Enhanced RL-SD

3.1.1 Recall of Rotman Lens (RL)

RLs are planar lenses that are generally used as beamforming feeding networks in antenna arrays. Given their combination of wide bandwidth, following from their true time delay nature [81], and low-cost beam switching capability, compared to expensive continuous-scanning systems, they suit applications such as ultra-wide band communication systems, collision avoidance radars, and remote-piloted vehicles [82–87]. Figure 3.1 shows the geometry and parameters of an RL. It is essentially a parallel-plate waveguide structure, with a substrate of permittivity ϵ_{r}, delimited by two geometrical contours: a left (L) contour, supporting the beamformer input ports (not shown explicitly in this figure), and a right (R) contour, branching out to an array of transmission lines feeding the antenna array elements. The angle α locates the position of the input ports, and $w(y_{\mathrm{a}})$ denotes the transmission line length at the output y_{a}, with $w_0 = w(y_{\mathrm{a}} = 0)$. Excitation of the port located at an angle α leads the antenna array to radiate at the angle ψ, and switching between different ports provides beam scanning. The lens is designed by considering plane wave excitation from the right of the RL structure, for convenient application of geometrical optics. In this situation, F_1, F_2 and F_3 are three perfect focal points along the left contour, with respective focal lengths f_1, f_2 and $f_3 = f_2$, and focal angles 0, α_0 and $-\alpha_0$, where α_0 corresponds to ψ_0. Perfect focalization is achieved at F_1, F_2 and F_3 if the optical path from the incident wave (from the right, corresponding to inverted blue arrows in Fig. 3.1) phase front to each of these points is the same for all the points $P(x_{\mathrm{R}}, y_{\mathrm{R}})$ connected to the antenna array on the right contour, particularly to the optical path from the center ($y = 0$) antenna element, i.e.

$$F_1 : w(y_{\mathrm{a}})\sqrt{\epsilon_{\mathrm{e}}} + \overline{PF_1}\sqrt{\epsilon_{\mathrm{r}}} = w_0\sqrt{\epsilon_{\mathrm{e}}} + f_1\sqrt{\epsilon_{\mathrm{r}}}, \tag{3.1a}$$

$$F_2 : y_{\mathrm{a}} \sin\psi_0 + w(y_{\mathrm{a}})\sqrt{\epsilon_{\mathrm{e}}} + \overline{PF_2}\sqrt{\epsilon_{\mathrm{r}}} = w_0\sqrt{\epsilon_{\mathrm{e}}} + f_2\sqrt{\epsilon_{\mathrm{r}}}, \tag{3.1b}$$

$$F_3 : -y_{\mathrm{a}} \sin\psi_0 + w(y_{\mathrm{a}})\sqrt{\epsilon_{\mathrm{e}}} + \overline{PF_3}\sqrt{\epsilon_{\mathrm{r}}} = w_0\sqrt{\epsilon_{\mathrm{e}}} + f_3\sqrt{\epsilon_{\mathrm{r}}}, \tag{3.1c}$$

where ϵ_{e} is the effective permittivity of the transmission lines. This represents a system of three equations in three unknowns, x_{R}, y_{R} and w, for the right contour $[x_{\mathrm{R}}(y_{\mathrm{a}}), y_{\mathrm{R}}(y_{\mathrm{a}})]$ and transmission line lengths $[w(y_{\mathrm{a}})]$. For the left contour, there is much design freedom. The simplest option is an arc of a circle, but other shapes, such as elliptical [83,88], hyperbolic [89] and non-canonical numerically-designed curves [90] may also be used to minimize phase aberrations and maximizing the scanning range. We opted for a circular arc here. Let us

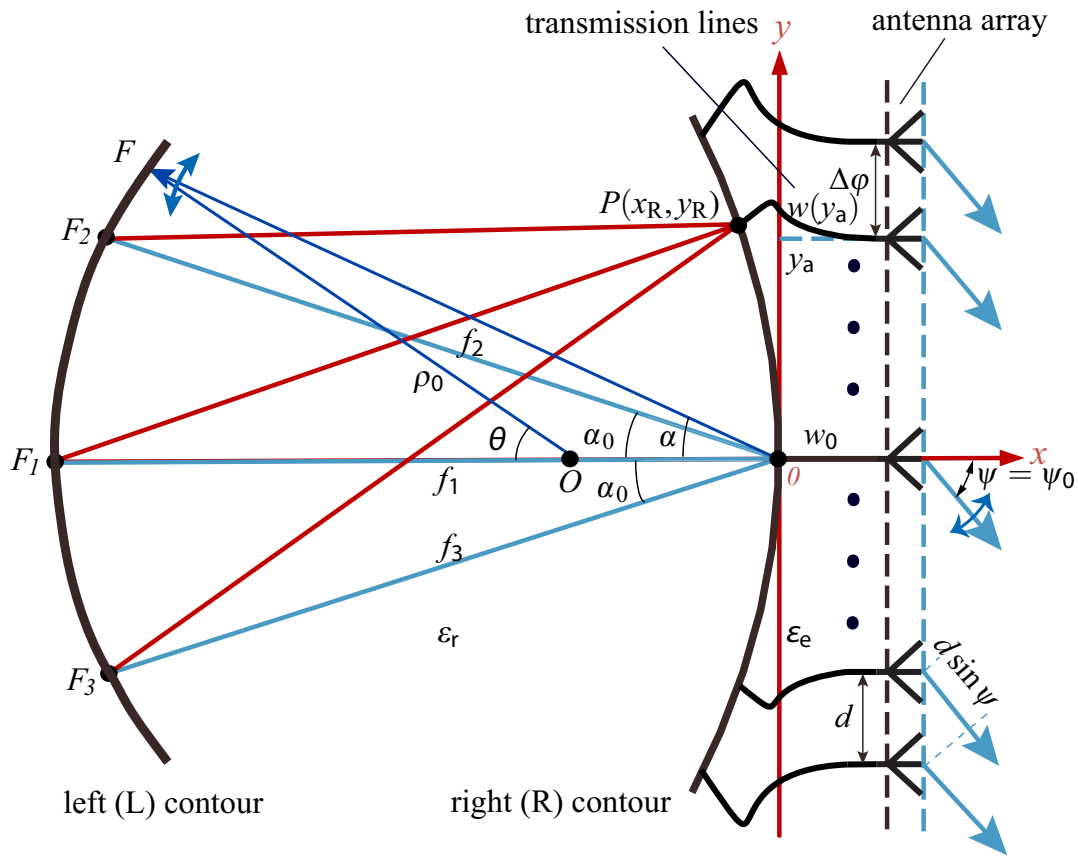

Figure 3.1 Geometry and parameters of the Rotman lens (RL).

finally define, for later use, the parameter

$$\gamma = \frac{\sin\psi_0}{\sin\alpha_0} \approx \frac{\sin\psi}{\sin\alpha}, \tag{3.2}$$

that relates the input port position angle (α) and the beam steering angle (ψ) [82]. In (3.2), the approximation and equality account for the fact that the beamforming operation is generally approximate, while being perfect only at the pairs $(0,0)$ and $(\pm\alpha_0, \pm\psi_0)$, corresponding to the aforementioned perfect focal points F_1, F_2 and F_3, respectively. The validity of the approximation in (3.2) is determined by several factors, including α_0, ψ_0, f_1 and f_2. In general, the accuracy of the approximation decreases as α_0 increases. The parameters of the Rotman lens should be sequentially controlled to ensure satisfactory approximation accuracy.

3.1.2 Basic RL-SD Description

The Zhang-Fusco RL-SD [16] is depicted in Fig. 3.2. In this device, the antenna array in Fig. 3.1 has been replaced by an open-ended reflecting transmission line array (R-TLA), and

the output ports with decomposed frequencies are on the left contour of the RL, as the input port, which is kept fixed for a specific spectral analysis.

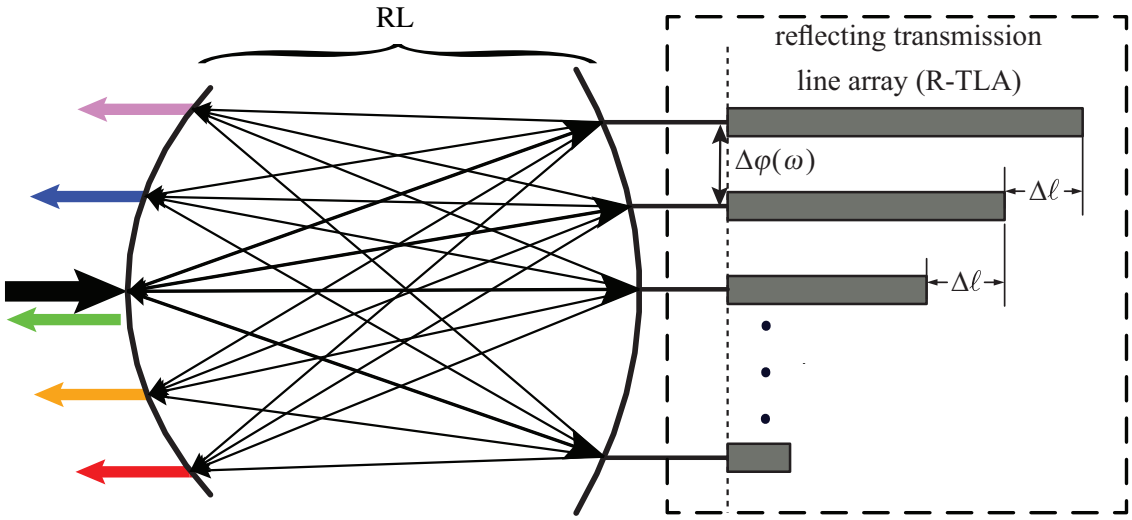

Figure 3.2 Rotman lens spectrum decomposition (RL-SD) reported in [16]. The connecting line segments between the lens and the RLTA represent here, and in all forthcoming figures, ideal connections with zero electrical length.

Assuming that the length difference between adjacent transmission lines is $\Delta\ell$, as shown in Fig. 3.2, the corresponding phase difference after reflection from the R-TLA is

$$\Delta\phi(\omega) = 2\beta_{\mathrm{e}}(\omega)\Delta\ell, \tag{3.3}$$

where the factor 2 accounts for the reflection round trip and $\beta_{\mathrm{e}}(\omega)$ is the effective wavenumber of the transmission lines,

$$\beta_{\mathrm{e}}(\omega) = k_0\sqrt{\epsilon_{\mathrm{e}}} = \frac{\omega}{c}\sqrt{\epsilon_{\mathrm{e}}}. \tag{3.4}$$

Calling the frequency and wavelength of the output central port (green arrow in Fig. 3.2) ω_0 and λ_0, respectively, and assuming that

$$\Delta\ell = N\frac{\lambda_0}{2} = N\frac{\pi c}{\sqrt{\epsilon_{\mathrm{e}}}\omega_0}, \quad N = 1, 2, 3, ... \tag{3.5}$$

leads, upon substitution of (3.4) and (3.5) into (3.3), to the frequency-dependent phase shift response

$$\Delta\phi(\omega) = 2\beta_{\mathrm{e}}(\omega)\Delta\ell = 2\pi N\frac{\omega}{\omega_0}. \tag{3.6}$$

The overall operation of the RL-SD may now be understood as follows. The signal to be

spectrally analyzed (represented by the black arrow in Fig. 3.2) is injected at the central port of the device. The corresponding wave propagates towards the right across the lens and hence splits to reach all the points of the right contour of the lens. At this stage, each split wave includes the entire spectrum of the input signal. Next, these waves are reflected by the R-TLA, which spectrally decomposes them according to the phase shift function (3.6). From (3.6), the frequency $\omega = \omega_0$ of the input signal corresponds to the phase gradient $\Delta\phi(\omega_0) = 2\pi N$, and the corresponding reflected waves will therefore constructively interfere at the central focal point, F_1, so that the part of the signal spectrum with $\omega = \omega_0$ emerges at that port (green arrow). The parts of the signal spectrum with $\omega > \omega_0$ and $\omega < \omega_0$ essentially correspond to phase gradients $0 < \Delta\phi(\omega) < \pi$ and $-\pi < \Delta\phi(\omega) < 0$, respectively, hence leading to spectral decomposition to the upper and lower ports of the device, respectively, as illustrated in Fig. 3.2.

3.1.3 Resolution and Input Port Diversification

In 3.1.2, we have not specified the locations of the output ports on the left contour of the RL. In [16], these ports were placed equidistantly in terms of the angle α in Fig. 3.2, i.e. such that $\alpha_{k+1} - \alpha_k =$ constant. Such a choice leads to non-uniform spectral resolution, as will be shown shortly, and fails to exploit the inherent flexibility of the RL. Moreover, in [16], the input port is collocated with one of the output ports, which inconveniently requires the utilization of a circulator to separate the input wave from the output wave at the same point. This paper resolves these two issues, and hence enhances the performance of the RL-SD.

Enhancing the resolution of the RL-SD will essentially consist in properly designing its frequency resolution function, $\varrho(\omega)$. Figure 3.3 shows the type of spectrum analysis performed by both the RL-SD of Fig. 3.2 and proposed enhanced versions of it to an arbitrary signal with spectrum $\Psi_{\text{in}}(\omega)$. Given the discrete nature of the ports, the spectral analysis will be a discrete version or, more precisely, a quantized version of $\Psi_{\text{in}}(\omega)$, and the resolution function is then [1]

$$\varrho(\omega) = \frac{1}{\Delta\omega(\omega)}, \tag{3.7}$$

where $\Delta\omega(\omega)$ represents the frequency varying distance between adjacent sampling points. This section only describes the general idea, to highlight the contribution of the paper, while the exact analysis will be provided in Sec. 3.2.

Figure 3.3(a) shows the response of an RL-SD with uniform angular port distribution ($\Delta\alpha =$

[1] The resolution $\varrho(\omega)$ cannot be infinite, it is also limited by the physical structure of the RL-SD, once the RL-SD is determined, the largest value of $\varrho(\omega)$ will be fixed.

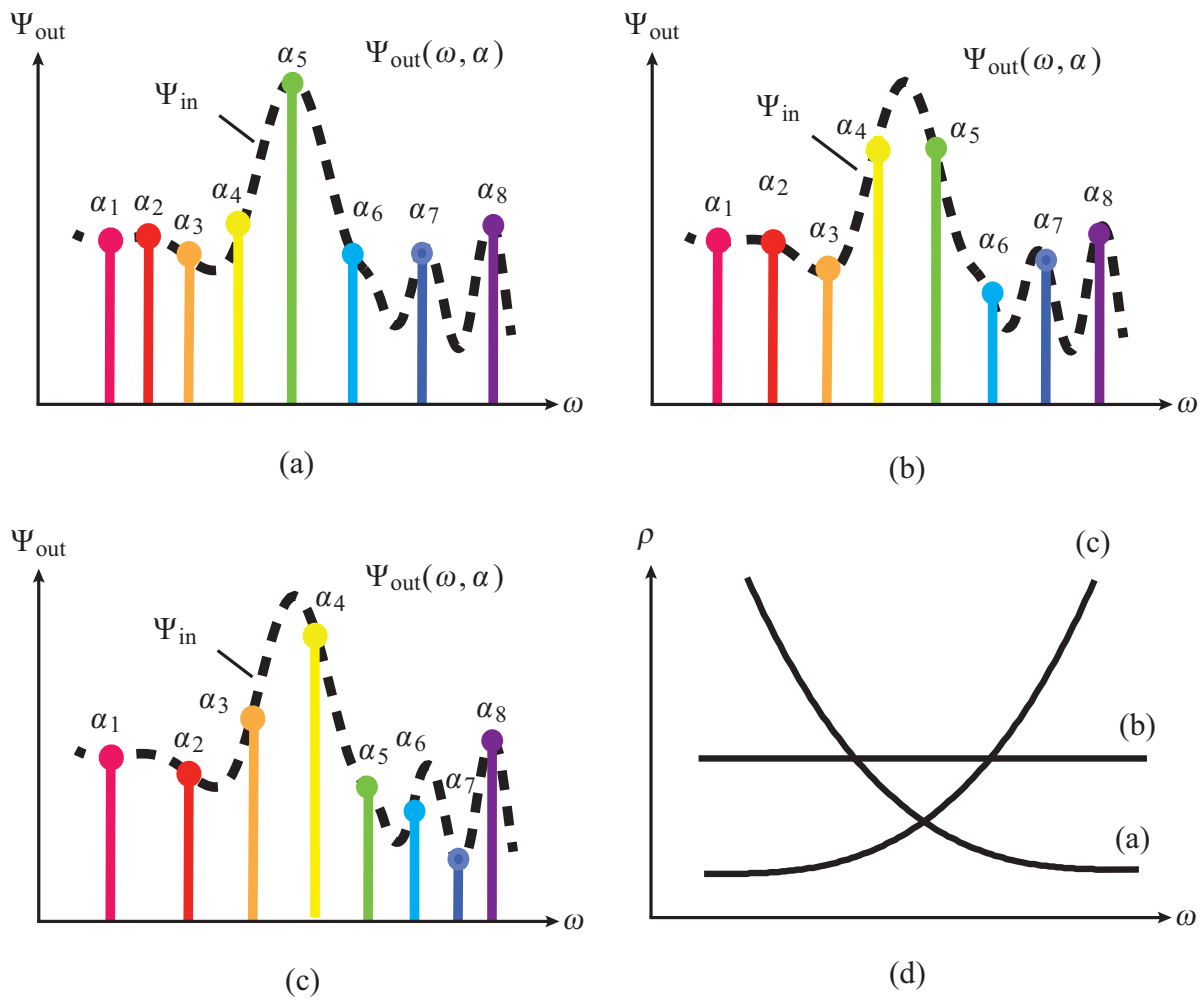

Figure 3.3 Spectrum analysis performed by different RL-SDs. (a) Conventional RL-SD (Fig. 3.2) with uniform port distribution ($\Delta\alpha$ = const.), leading to decreasing resolution ($\varrho = 1/\Delta\omega$) with increasing frequency ($\partial\varrho/\partial\omega < 0$). (b) RL-SD with nonuniform port distribution designed for uniform resolution ($\partial\varrho/\partial\omega = 0$ or $\Delta\omega$ = const.). (c) RL-SD with nonuniform port distribution designed for reversed resolution compared to (b), i.e. increasing resolution with increasing frequency ($\partial\varrho/\partial\omega > 0$). (d) Resolution ($\varrho$) versus frequency ($\omega$) for the RL-SDs (a), (b) and (c).

const.), as implicitly assumed in Fig. 3.2, a resolution that decreases with increasing frequency, or $\partial\varrho/\partial\omega < 0$, as shown in Fig. 3.3(d) [16]. In the particular case of the signal $\Psi_{in}(\omega)$ in Fig. 3.3, this leads to over-sampling and under-sampling the lower and higher parts, respectively, of the signal spectrum.

Since the signal to analyze is generally unknown, no a priori assumption can be made on its spectrum, and therefore designing the device for uniform resolution would generally be the best strategy. As a uniform port distribution leads to nonuniform resolution [Fig. 3.3(a)],

we can deduce that the ports must be properly *nonuniformly* distributed to provide uniform resolution, corresponding to $\partial\varrho/\partial\omega = 0$, as shown in Figs. 3.3(b) and 3.3(d).

In the case where there would be some a priori knowledge on the general shape of signal spectrum, as for instance if one would know that there is higher variations at the higher part of the spectrum as in Fig. 3.3, then one could deliberately distort the resolution function so that $\partial\varrho/\partial\omega > 0$, as shown in Figs. 3.3(c) and 3.3(d), where the resolution function leads to the best frequency sampling for the given input signal.

Thus, uniformizing or manipulating the resolution function, $\varrho(\omega)$, of the RL-SD, is highly desirable. We will show in Sec. 3.2 how exactly this can be achieved by adjusting the position of the output ports, as represented in Fig. 3.4, since $\omega = f(\alpha)$.

Another desirable enhancement of the RL-SD would be to provide flexibility in the location of the input port, for the following two reasons. First, when the desired resolution function leads to a design with an output port at the same location as the input port, as for instance in Fig. 3.2, a circulator or directional coupler is required to separate the input signal and output decomposed signal. Second, the resolution-enhanced design may have no output ports and no room for an input port at the center of the structure. Such an enhancement can be realized by the insertion of a calibration transmission line array (C-TLA) between the lens and the R-TLA, as shown in Fig. 3.4 with $\omega = f(\alpha; \alpha_{\text{in}})$ and as will be detailed in Sec. 3.2.2.

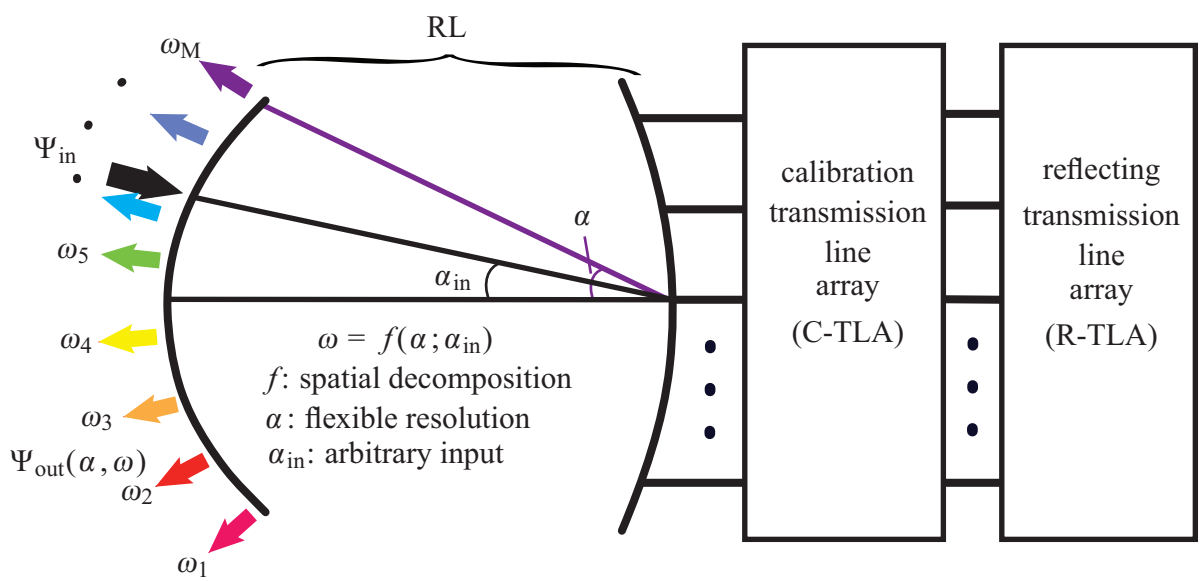

Figure 3.4 Proposed concept of flexible-resolution and arbitrary-input RL-SD.

3.2 Synthesis

3.2.1 Frequency-Position Relationship

The relationship existing between the spectral component ω and the position α on the left contour of the RL may be found by equating the function $\Delta\phi(\omega)$ corresponding to the R-TLA in Fig. 3.2, which is given by (3.6) and may be generalized to

$$\Delta\phi(\omega) = 2\pi N\left(\frac{\omega}{\omega_0}\right) - 2\pi N, \tag{3.8}$$

and the function $\Delta\phi(\omega)$ corresponding to the RL beamforming in Fig. 3.1, which is given, according to antenna array theory, by

$$\Delta\phi(\omega) = \frac{\omega}{c} d \sin\psi = \frac{\omega}{c} d\gamma \sin\alpha, \tag{3.9}$$

where (3.2) has been used in the last equality. Equating (3.8) and (3.9), and solving the resulting equation for ω yields the sought after relationship:

$$\omega(\alpha) = \frac{2\pi N\omega_0 c}{2\pi N c - \omega_0 d\gamma \sin\alpha}. \tag{3.10}$$

Assuming that the RL-SD output port angle α is limited to $[-\alpha_0, \alpha_0]$, the maximal frequency and minimal frequency are found by replacing α in (3.10) with α_0 and $-\alpha_0$, respectively, which yields

$$\omega_{\max} = \frac{2\pi N\omega_0 c}{2\pi N c - \omega_0 d\gamma \sin\alpha_0}, \tag{3.11a}$$

$$\omega_{\min} = \frac{2\pi N\omega_0 c}{2\pi N c + \omega_0 d\gamma \sin\alpha_0}, \tag{3.11b}$$

respectively.

The function $\omega(\alpha)$ in (3.10) is plotted in Fig. 3.5 for different values of N. It clearly appears that ω is a monotonically increasing function of α within the range $[-\alpha_0, \alpha_0]$. The figure also reveals that N provides a parameter to trade off bandwidth and resolution, since the α variable will eventually be restricted to the discrete output ports. In Fig. 3.5, the operating bandwidth decreases from 25.0 GHz to 5.8 GHz as N increase from 1 to 4, while the resolution is enhanced by the same factor (on average in case of nonuniform port distribution).

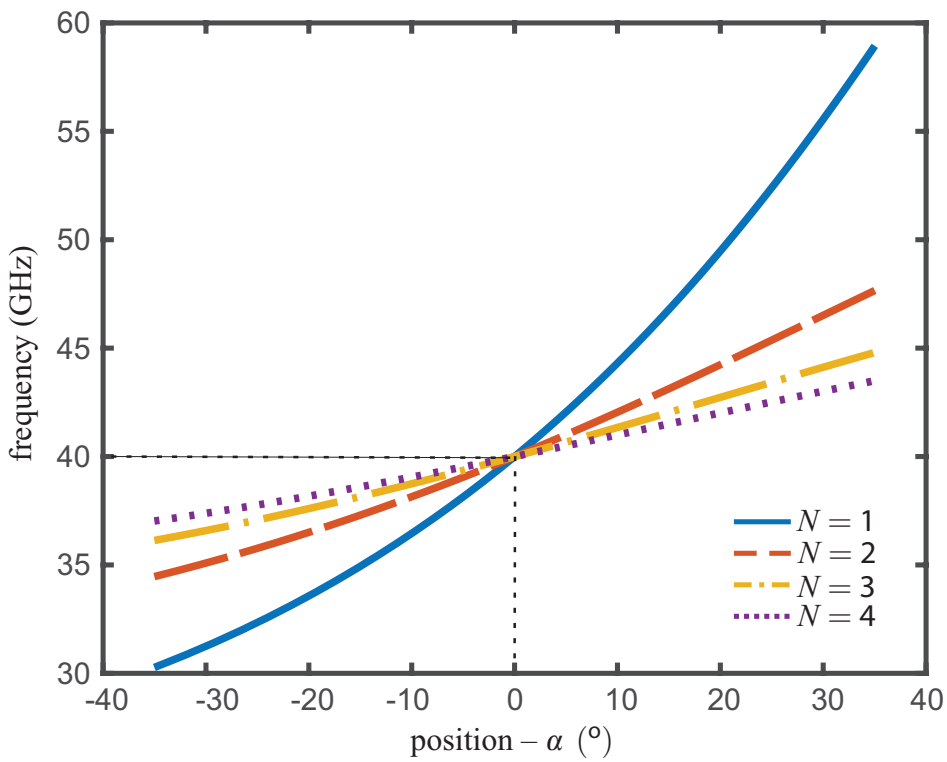

Figure 3.5 Decomposition of frequency versus position on the left contour of the RL-SD in Fig. 3.2, determined by the angle α (Fig. 3.1), for different values of N [Eq. (3.5)], with $2\pi\omega_0 = 40$ GHz and $d = \lambda_0/2$.

3.2.2 Calibration Transmission Lines for Arbitrary Input Position

Changing the position of the input port in the RL-SD of Fig. 3.2, as illustrated in Fig. 3.6(a), would naturally modify the optical path lengths across the structure and hence alter its response. According to (3.2), $\alpha_{\text{in}} = 0$ (Fig. 3.2) corresponds to $\psi = 0$. Therefore, since the sine function in (3.2) is monotonous in its range of interest about 0, $\alpha_{\text{in}} \neq 0$ corresponds to $\psi = \psi' \neq 0$. Such nonzero angle, would correspond in the beamformer to the phase shift function $\Delta\phi_{\text{in}} = \frac{\omega}{c}\gamma d \sin\alpha_{\text{in}}$. This is a phase term that must now be added to (3.8) in order to account for the effect of the displacement of the input port. Thus, Eq. (3.8) generalizes to

$$\Delta\phi(\omega) = 2\pi N\left(\frac{\omega}{\omega_0}\right) - 2\pi N - \frac{\omega}{c}\gamma d \sin\alpha_{\text{in}}. \tag{3.12}$$

Equating (3.12) to (3.9), and solving the resulting equation for ω yields the following generalization of (3.10):

$$\omega(\alpha) = \frac{2\pi N\omega_0 c}{2\pi N c - \omega_0 d\gamma(\sin\alpha + \sin\alpha_{\text{in}})}. \tag{3.13}$$

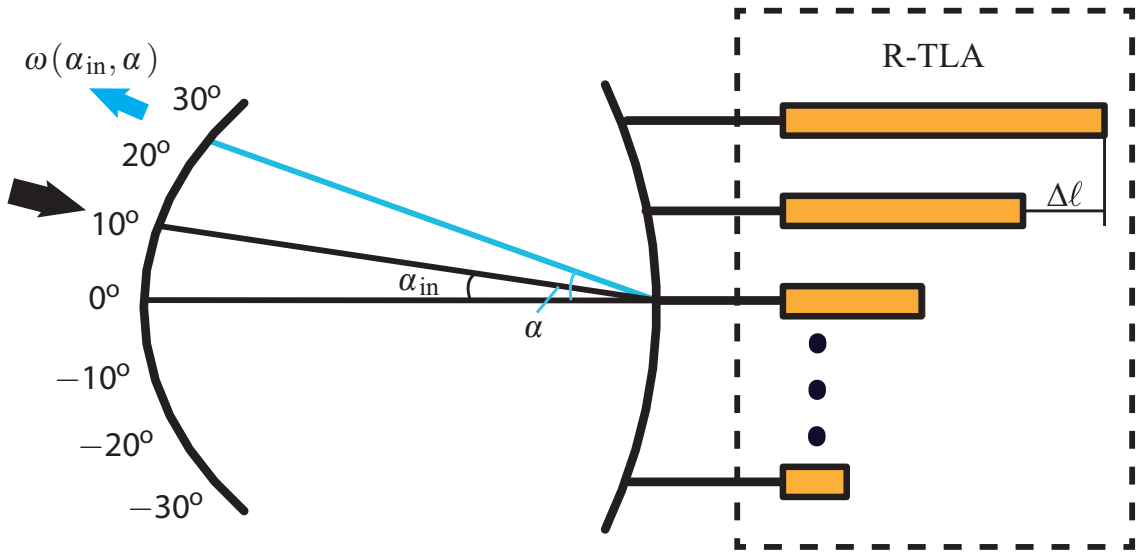

(a)

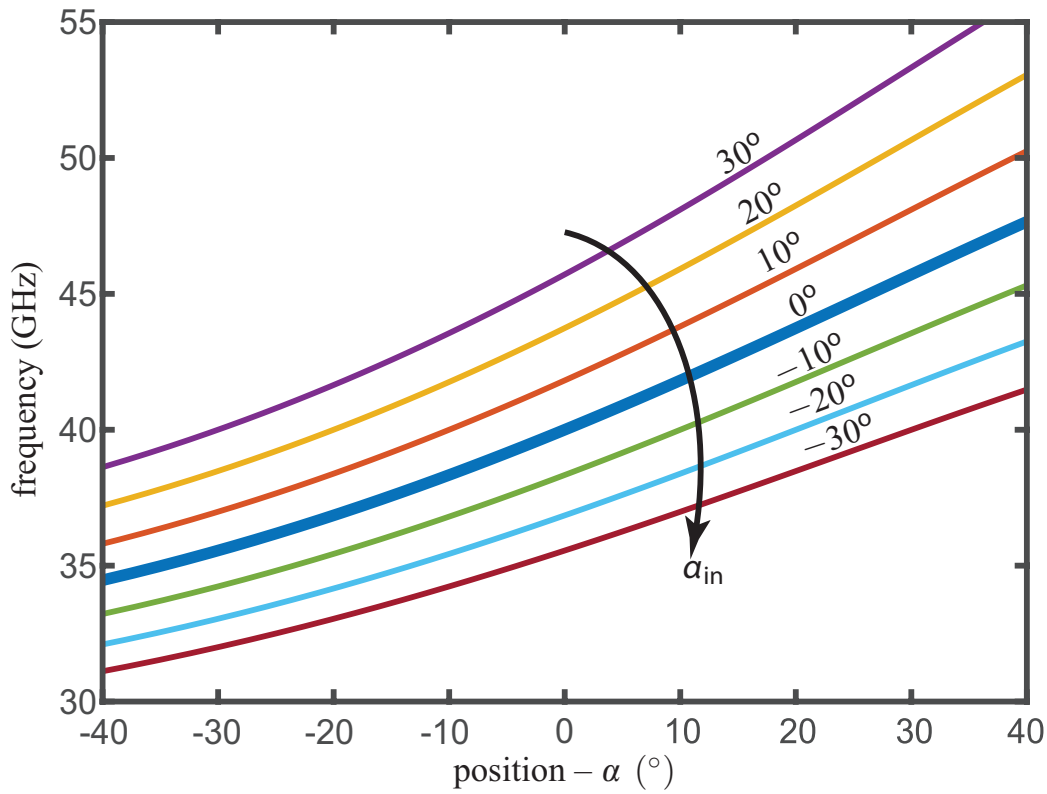

(b)

Figure 3.6 Frequency deviation [Eq. (3.13)] caused by displacement of the input port from the middle ($\alpha_{\text{in}} = 0$, thick curve) of the RL-SD structure. (a) Input port location α_{in} and decomposition function $f(\alpha, \alpha_{\text{in}})$. (b) Frequency versus position for $\alpha_{\text{in}} = 0^o, \pm 10^o, \pm 20^o, \pm 30^o$.

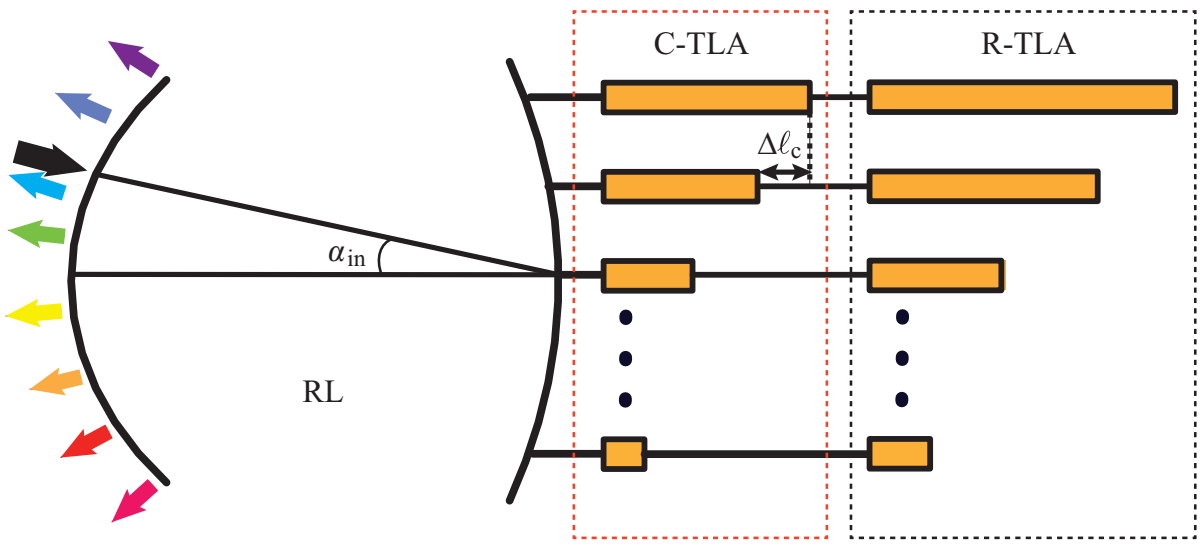

Figure 3.7 Incorporation of calibration transmission line array (C-TLA) for suppressing the deviation effect in Fig. 3.6, i.e. merging all curves $\alpha_{in} \neq 0$ to the curve $\alpha_{in} = 0$ in that figure.

The frequency deviation computed by this relation is plotted in Fig. 3.6(b). The graph also shows that the decomposition frequency range is shifted, towards higher and lower frequencies for positive and negative values of α_{in}, respectively. In order to avoid this shift, we insert a calibration transmission line array (C-TLA) between the lens and the R-TLA, as shown in Fig. 3.7, to exactly compensate for the negative $\Delta\phi_{in}$ in (3.12). For this condition to be satisfied, the C-TLA must add the phase shift $+\frac{\omega}{c}\gamma d \sin\alpha_{in}$, and its lengths difference, $\Delta\ell_c$, must therefore satisfy the relation

$$2\beta_e(\omega_0)\Delta\ell_c = \frac{\omega}{c}\gamma d \sin\alpha_{in}, \tag{3.14}$$

which yields

$$\Delta\ell_c = \frac{d}{2}\gamma\sqrt{\frac{1}{\epsilon_e}}\sin\alpha_{in}. \tag{3.15}$$

After such calibration, the relevant formula for the frequency-position law is again back to (3.10).

3.2.3 Frequency-Position Sampling for Flexible Resolution

Equation (3.10) confirms and quantifies the dependence between the output port position and the frequency, that was qualitatively described in Sec. 3.1.3. Figure 3.8 shows how this relation, which is independent of the input port location after calibration, can be manipulated

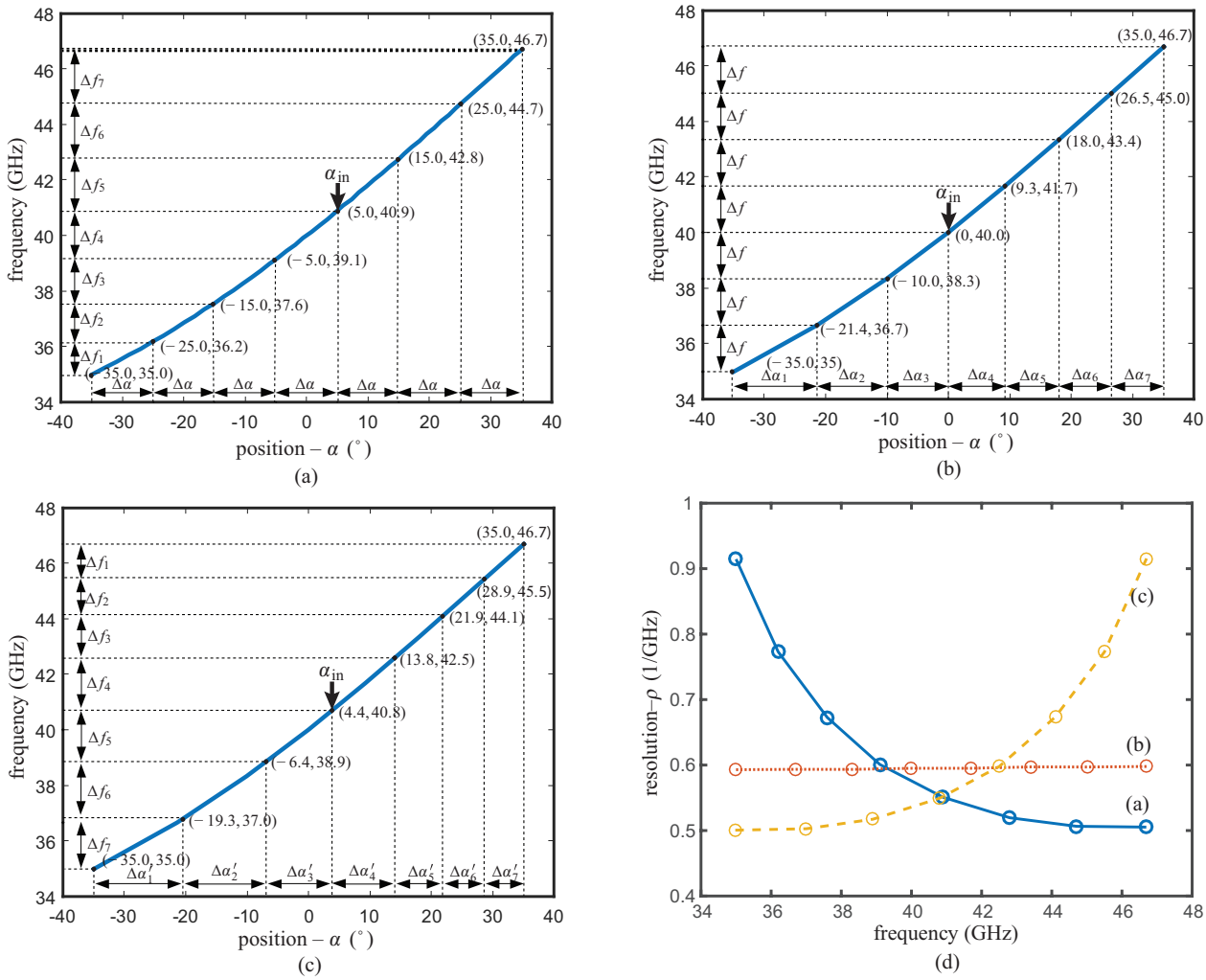

Figure 3.8 Resolution diversification of the RL-SD via modulation of the position distribution α_m, $m = 1, 2, 3, ..., M$ for the following parameters: $2\pi\omega_0 = 40$ GHz, $d = \lambda_0/2$ and $N = 2$. (a) Uniform port distribution ($\Delta\alpha$ = const.) leading to nonuniform spectrum resolution ($\varrho \neq$ const.) [Fig. 3.3(a)]. (b) Nonuniform port distribution ($\Delta\alpha \neq$ const.) leading to uniform spectrum resolution (ϱ = const.) [Fig. 3.3(b)]. (c) Nonuniform port distribution ($\Delta\alpha \neq$ const.) leading to reversed spectrum resolution of uniform port distribution [Fig. 3.3(c)]. (d) Resolution (ϱ) versus frequency (ω) for the RL-SDs in (a) (b) and (c). (Note that the curves in (a), (b) and (c) are exactly the same, only the (ω, α) sampling and position of input port (α_{in}) differs between them.)

to provide the spectrum analysis diversification illustrated in Fig. 3.3.

Figure 3.8(a) shows the case of uniform angular port distribution ($\Delta\alpha = \text{const.}$), leading to decreasing resolution with increasing frequency ($\partial\varrho/\partial\omega < 0$) and corresponding to Fig. 3.3(a). Figure 3.8(b) shows the case the nonuniform angular port distribution ($\Delta\alpha \neq \text{const}$) that leads to uniform resolution ($\partial\varrho/\partial\omega = 0$), corresponding to Fig. 3.3(b). Figure 3.8(c) shows a case of nonuniform angular port distribution leading to reversed resolution compared to Fig. 3.8(a), ($\partial\varrho/\partial\omega > 0$) and corresponding to Fig. 3.3(c). The resolution versus frequency curves for the three cases are compared in Fig. 3.8(d), corresponding to the qualitative result of Fig. 3.3(d).

3.2.4 Range and Resolution Tuning by Input Switching

Once the RL-SD has been built for the desired frequency range and resolution, according to the methodology outlined in the previous sections, we may be interested, for applications requiring adaptivity, to tune these parameters. Such a tunability functionality may be added by introducing port switching.

This may be seen following a procedure that is similar to that used in Sec. 3.2.2 for calibration transmission lines. According to (3.2), $\sin(\psi_{\text{in}}) = \gamma\sin(\alpha_{\text{in}})$. Therefore, switching from the input located at α_{in} to the port located at $\alpha_{\text{in}}+\Delta\alpha_{\text{in}}$, leads to $\sin(\psi_{\text{in}}+\Delta\psi) = \gamma\sin(\alpha_{\text{in}}+\Delta\alpha_{\text{in}})$. These two cases correspond to the beamformer phase shift functions $\Delta\phi_{\text{a}} = \frac{\omega}{c}\gamma d\sin\alpha_{\text{in}}$ and $\Delta\phi_{\text{b}} = \frac{\omega}{c}\gamma d\sin(\alpha_{\text{in}} + \Delta\alpha_{\text{in}})$, respectively, which leads to the phase difference $\Delta\phi_{\text{b}} - \Delta\phi_{\text{a}} = \frac{\omega}{c}\gamma d[\sin(\alpha_{\text{in}} + \Delta\alpha_{\text{in}}) - \sin\alpha_{\text{in}}]$, and hence to the new phase function

$$\Delta\phi(\omega) = 2\pi N\left(\frac{\omega}{\omega_0}\right) - 2\pi N - \frac{\omega}{c}\gamma d[\sin(\alpha_{\text{in}} + \Delta\alpha_{\text{in}}) - \sin\alpha_{\text{in}}]. \tag{3.16}$$

Equating this relation to (3.9) yields the tuning law

$$\omega(\alpha) = \frac{2\pi N\omega_0 c}{2\pi Nc - \omega_0 d\gamma[\sin\alpha + \sin(\alpha_{\text{in}} + \Delta\alpha_{\text{in}}) - \sin\alpha_{\text{in}}]}. \tag{3.17}$$

Figure 3.9(a) plots this $\omega(\alpha)$ relation, after calibration, under input port switching tuning from $\alpha_{\text{in}} = 5°$. The curve $\Delta\alpha_{\text{in}} = 0°$ in this figure corresponds to the (unique) curve in Fig. 3.8, while the curves $\Delta\alpha_{\text{in}} = \pm 10°$ represent shifted curves resulting from switching from $\alpha_{\text{in}} = 5°$ to $\alpha_{\text{in}} + \Delta\alpha_{\text{in}} = 15°$ and $\alpha_{\text{in}} + \Delta\alpha_{\text{in}} = -5°$. As may be seen, port switching results in frequency *range* tuning ($[f_{\text{min}}, f_{\text{max}}]$). Figure 3.9(b) shows the port switching tuning achieved for different sampling strategies, and indicates that port switching also leads to resolution ($[\varrho(\alpha)]$) variation. Note that the frequency range and resolution tunings are not independent

from each other: the resolution variation follows the reverse trend as the range.

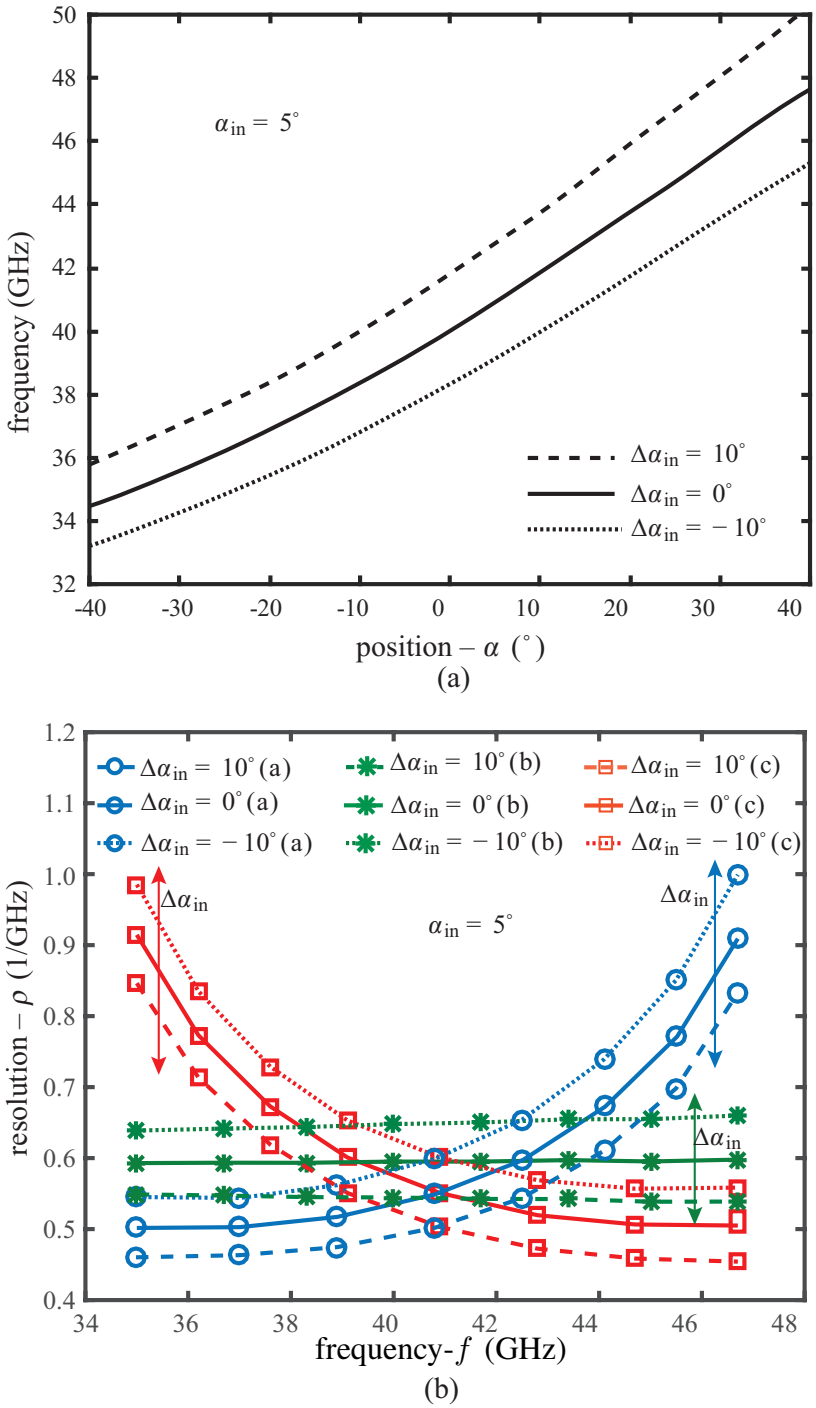

Figure 3.9 Tuning obtained by switching the input port (or vary $\Delta\alpha_{\text{in}}$) from the starting $\alpha_{\text{in}} = 5°$ using (3.17). (a) Frequency range tuning achieved with $\Delta\alpha_{\text{in}} = -10°, 0°, 10°$. (b) Application of the three sampling strategies shown in Fig. 3.8 for each of the three port-switched curve in (a), showing also frequency resolution tuning.

3.3 Design Procedure

The overall design procedure of the flexible-resolution, arbitrary-input and tunable RL-SD is as follow:

1. Specify the operating frequency range $[f_{\min}, f_{\max}]$.

2. Choose the focal lengths f_1 and f_2 based on trade-off between device size and number of ports (and hence resolution). This selection involves a tradeoff between the shape of the contours, and hence the available space for the ports, the loss and the phase error of the Rotman lens. For instance, larger f_1 obviously leads to a larger lens and hence larger path loss. Another point is that increasing the ratio f_1/f_2 changes the lens shape, opening the left contour and closing the right contour, which affects the location of the ports.

3. Select a set of parameters ω_0, N, d, α_0 γ to accommodate the $[f_{\min}, f_{\max}]$ according to (3.11). One should be very careful when selecting α_0 and γ, as excessive α_0 and γ may lead to excessive phase error.

4. Determine the RL geometry in terms of its transmission line lengths, left contour and right contour, respectively.

5. Determine a number of ports based on the room available, the isolation requirement and the position of the ports on the left contour using (3.10). The resolution of the RL-SD for a designed frequency range is determined by the ports position on the left contour, while the isolation of the decomposed spectrum is mainly determined by the number of ports on the right contour. For a fixed shape of the contour, the more transmission lines there are on the right contour, the higher the spectrum isolation is.

6. Calculate the transmission line width for 50 Ω characteristic impedance and connect all the output points to the output ports with these lines using a taper for broadband impedance matching.

7. Calculate transmission line length differences $\Delta\ell$ of the R-TLA according to (3.5) and $\Delta\ell_{\mathrm{c}}$ of the C-TLA according to (3.15).

8. Interconnect the C-TLA, R-TLA and RL.

3.4 Results

In order to demonstrate the concepts developed in the previous sections, we present here the design, simulation, fabrication and measurement of two RL-SD prototypes, corresponding to the frequency-position sampling strategies to Fig. 3.8(a) and Fig. 3.8(b), namely a prototype with uniform port distribution and nonuniform spectrum resolution and a prototype with nonuniform port distribution and uniform spectrum resolution. Figure 3.10 shows the photographs of the two prototypes, with Fig. 3.10(a) and Fig. 3.10(b) corresponding to Fig. 3.8(a) and Fig. 3.8(b), respectively. The two designs have the following parameters in common. They are fabricated on a 0.254 mm (10 mil) thick Rogers 6002 dielectric substrate with dielectric constant 2.94 and loss tangent 0.0012, for the frequency range [35, 46.7] GHz and $f_0 = 40$ GHz. They include 8 output ports and 15 RL transmission lines with corresponding C-TLA and R-TLA designed for the specified spectrum resolution and isolation requirements. The two designs also share the same RL symmetry, with $f_1 = 28.4$ mm, $f_2 = 25.6$ mm, $\alpha_0 = \psi_0 = 35°$ and $d = \lambda_0/2$, where f_1 and f_2 are chosen so as to ensure sufficient space to accommodate the ports on both left and right contour of the Rotman lens, $\alpha_0 = \psi_0$ is designed to minimize the phase error of the Rotman lens, and a relative large $\alpha_0 = 35°$ is selected to place all the ports of the left contour within the angle range $[-\alpha_0, \alpha_0]$. The R-TLA transmission line length difference in the two designs is $\Delta\ell = 4.8$ mm with $N = 2$. All the transmission line widths in both designs are 0.66 mm wide.

The first prototype [Fig. 3.10(a)] has uniformly distributed output ports with port 4 as the input port at $\alpha_{\text{in}} = 5°$ and C-TLA lines length difference $\Delta\ell_{\text{c}} = 0.066$ mm according to (3.15). The second prototype [Fig. 3.10(b)] has nonuniformly distributed ports for uniform resolution with port 5 as the input port with $\alpha_{\text{in}} = 0°$ and C-TLA lines length difference $\Delta\ell_{\text{c}} = 0$.

The RL-SDs are simulated with the help of full-wave simulation solver ANSYS Electronics 2015. Figures 3.11 plots the simulated and measured scattering parameters for the designs. The main beams are centered at the expected frequency with an isolation in the order of 10 dB to the parasitic side-lobes, corresponding to leakage to other ports, due to port coupling. The measured results feature about 2 dB more loss than the simulation results, due to larger material loss [91] and impedance mismatched. The measured results also exhibit lower isolation, below −8.3 dB and −7.6 dB for all the beams in the first and second designs, respectively. In order to verify the reasons leading to the 2 dB loss mismatch, a simulating tolerance analysis is performed for the uniform resolution design by sweeping 3 main parameters (tangent loss of the substrate, effective conductivity of copper and port impedances) that may influence the discrepancy between measurements and simulation, respectively.

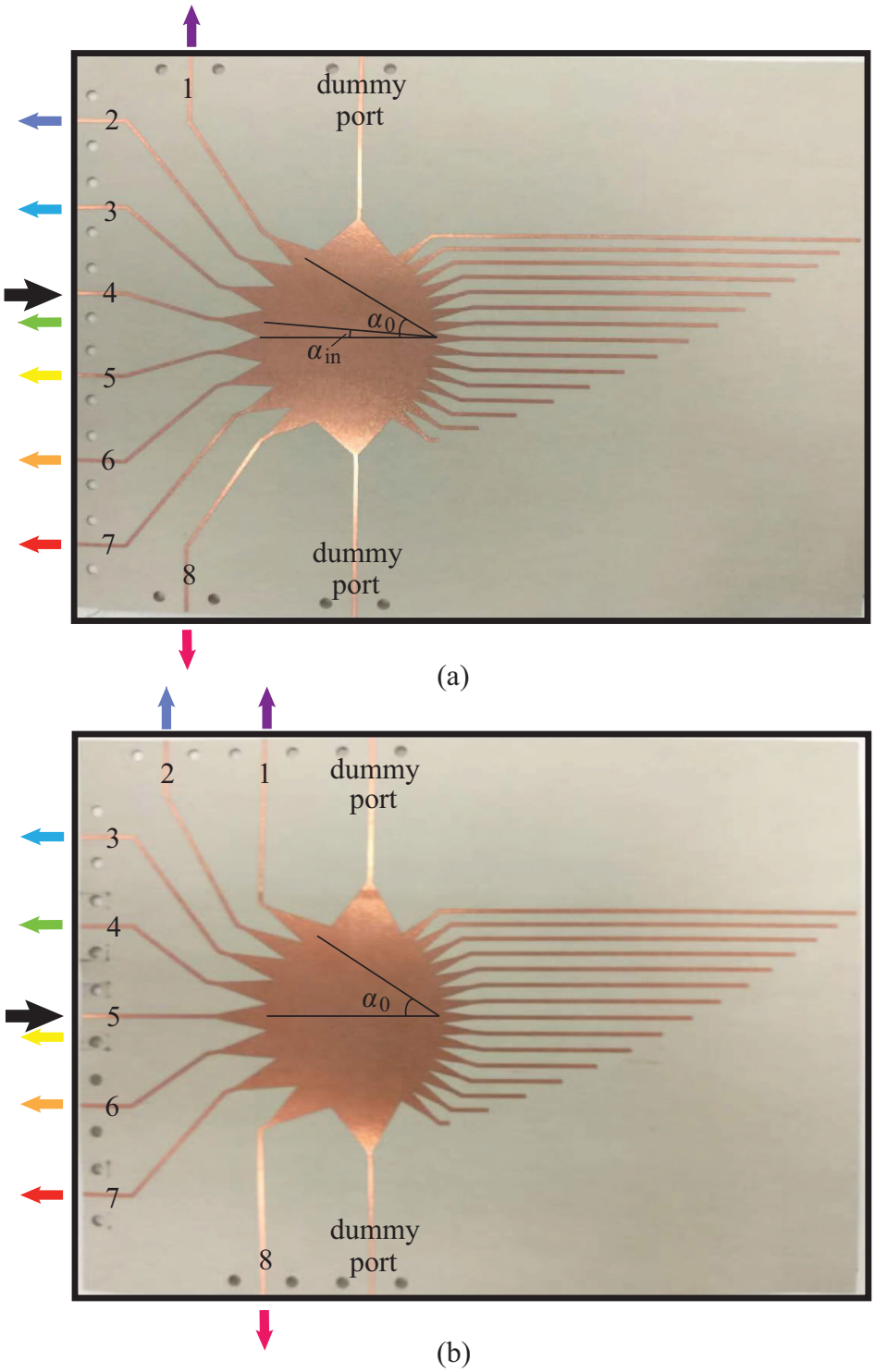

Figure 3.10 RL-SD prototypes. (a) Uniform port distribution with off-axis input [Fig. 3.8 (a)]. (b) Uniform spectrum resolution [Fig. 3.8 (b)].

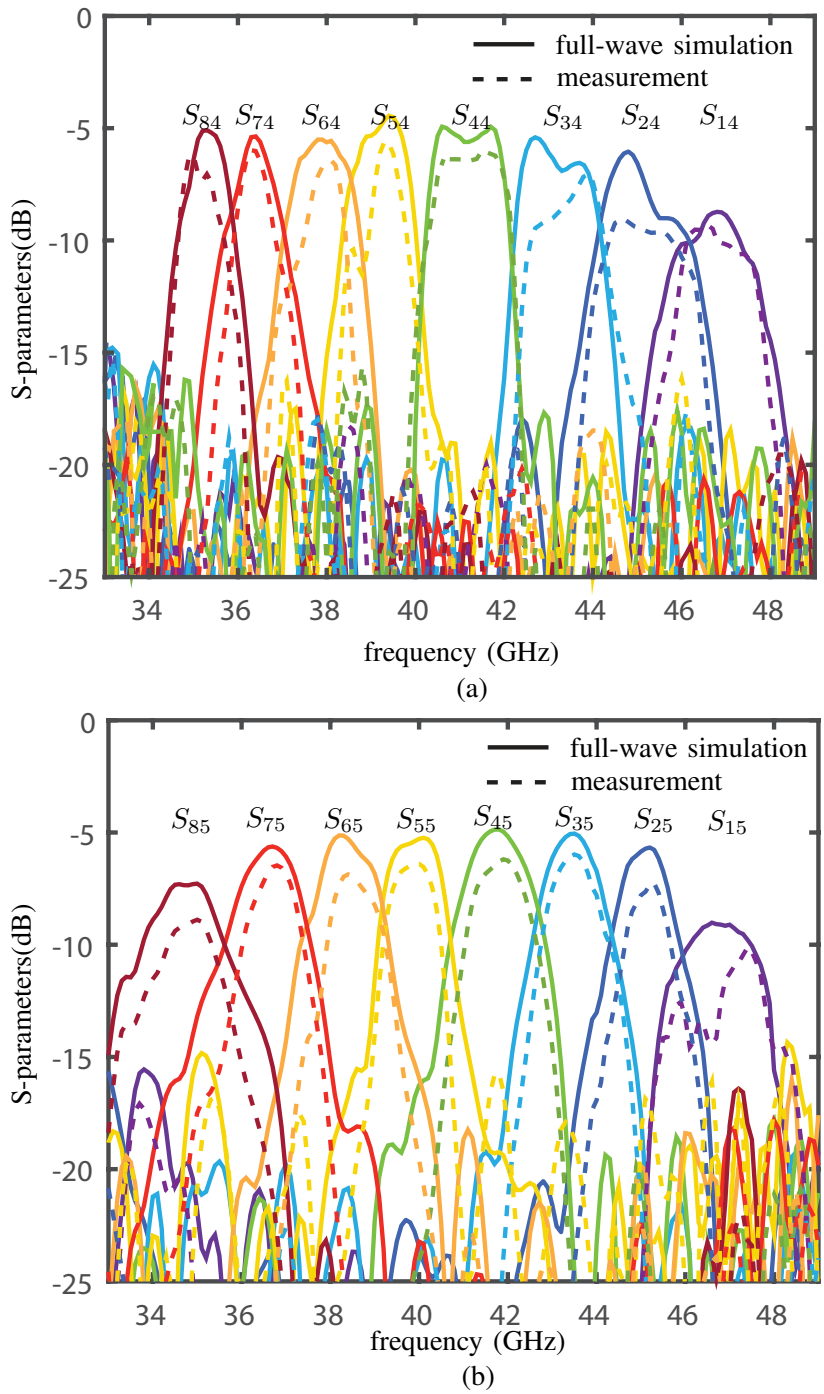

Figure 3.11 Comparison of full-wave simulated and measured scattering parameters. (a) Uniform port distribution with off-axis input [Fig. 3.8(a)]. (b) Uniform spectrum resolution [Fig. 3.8(b)]. Each color corresponds to the spectrum reaching an output port and should not be confused with the port colors in Fig. 3.10 that represent only the maximal spectral energy.

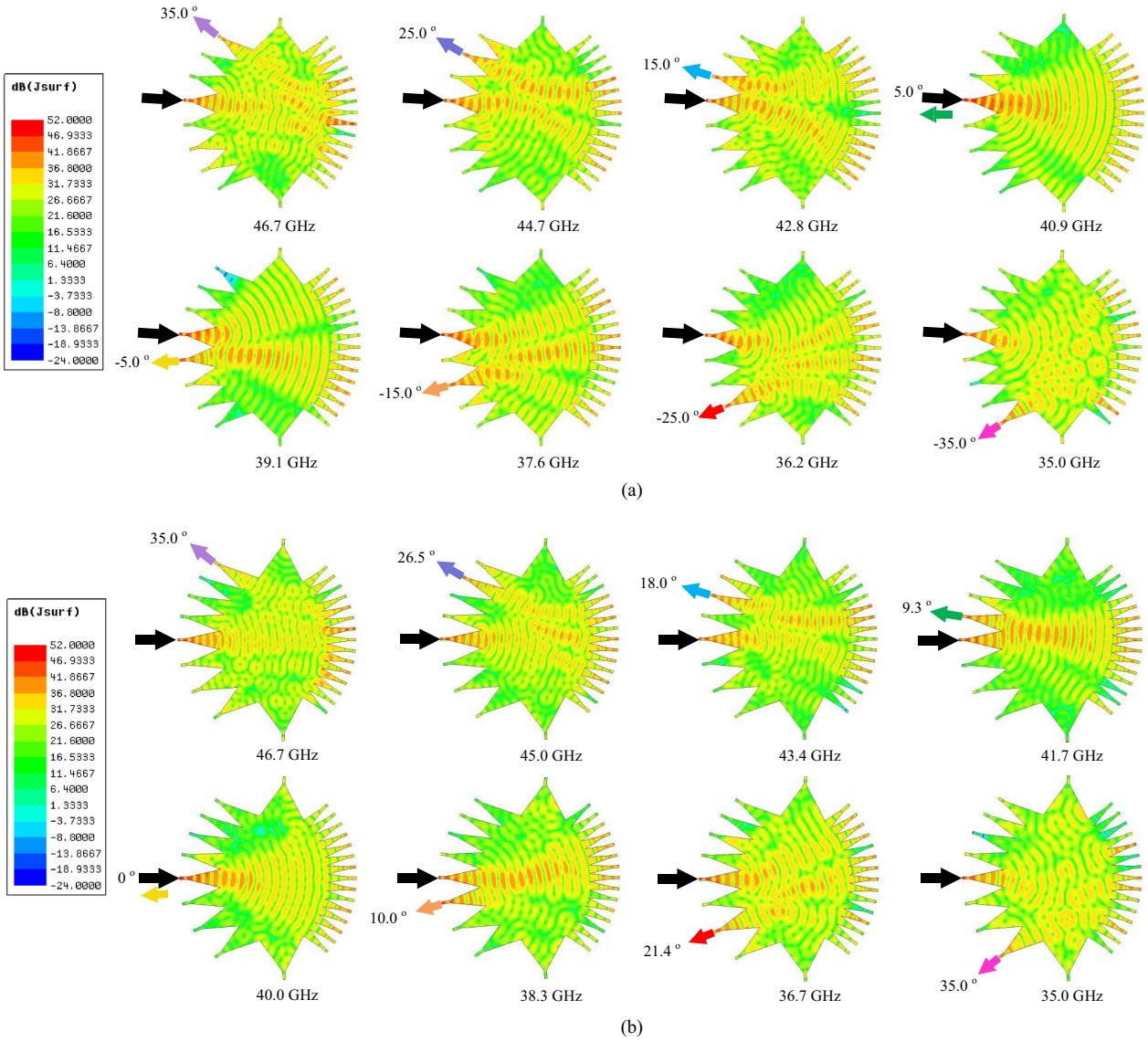

Figure 3.12 Current distribution. (a) Current distribution in RL-SD with uniform port distribution, nonuniform spectrum resolution and $\alpha_{\text{in}} = 5^o$ [Fig. 3.8(a)]. (b) Current distribution in RL-SD with nonuniform port distribution, uniform spectrum resolution and $\alpha_{\text{in}} = 0^o$ [Fig. 3.8(b)].

Finally, Fig. 3.12(a) and (b) show the simulated current distributions in the RL part of the RL-SD of the two prototypes. They clearly show that the currents flow to the expected output ports, corresponding to the designs in Fig. 3.8(a) and Fig. 3.8(b). The specified and simulated (from S-parameters) mid-band (3-dB) frequencies are compared in Table 3.1. This comparison shows that the simulated results are in good agreement with the specifications. The small discrepancy that is attributed to the approximation in Eq. (3.2) and simulation

Table 3.1 Comparison between specified and simulated (from S-parameters) mid-band (3-dB) frequencies (GHz).

RL-SD with uniform port distribution [Fig. 3.10(a) and 3.11(a)]								
Spec.	35	36.2	37.6	39.1	40.9	42.8	44.7	46.7
Sim.	35.1	36.2	37.4	39.2	41.1	42.7	44.6	46.9

RL-SD with uniform spectrum resolution [Fig. 3.10(a) and 3.11(a)]								
Spec.	35	36.7	38.3	40.0	41.7	43.4	45	46.7
Sim.	35	36.6	38.1	40.1	41.8	43.5	45.1	46.6

tolerance.

Moreover, to verify the tunability of the RL-SD, we plot in Fig. 3.13 the simulated S-parameters involved upon input switching in the uniform-resolution prototype of Fig. 3.10(b). The results shows that uniform resolution is almost maintained, while the overall frequency range has been shifted according to the chosen input port.

3.5 Application for Real-time Spectrum Sniffing

Future wireless communication systems will need drastic enhancements to accommodate anticipated end-user speed and reliability requirements. Reconfiguration strategies, globally referred to as *cognitive radio* [92], may become a pivotal approach to address this challenge in forthcoming 5G systems, especially in applications with extremely high throughput, such as UHD and 3D video [93].

Cognitive radio consists in two main operations: first sensing – or "*sniffing*" – the ambient spectrum so as to identify white (free) bands in it, and next reconfigure the radio system to exploit these white bands for optimal spectral efficiency at all times.

The spectrum sniffing operation has been traditionally performed in a digital manner, using energy detection, matched-filter detection, cyclostationary-feature detection or spatio-temporal spectrum occupation detection [94–97]. However, as the operating frequency gets higher and the operating bandwidth becomes wider, as is typically the case in the millimeter-wave regime, spectrum sniffing should be realized in an *ultra-fast* fashion. In such situations, digital approaches may be just too slow, or excessively expensive and power hungry, and an *alternative technology is hence required*.

Recently, an energy-detection Real-Time Spectrum Sniffer (RTSS) based on a mixer and a coupled-line phaser with stair-case group delay response has been reported in [98]. However, this sniffer is limited by the following features: requirement for an auxiliary pulse generator

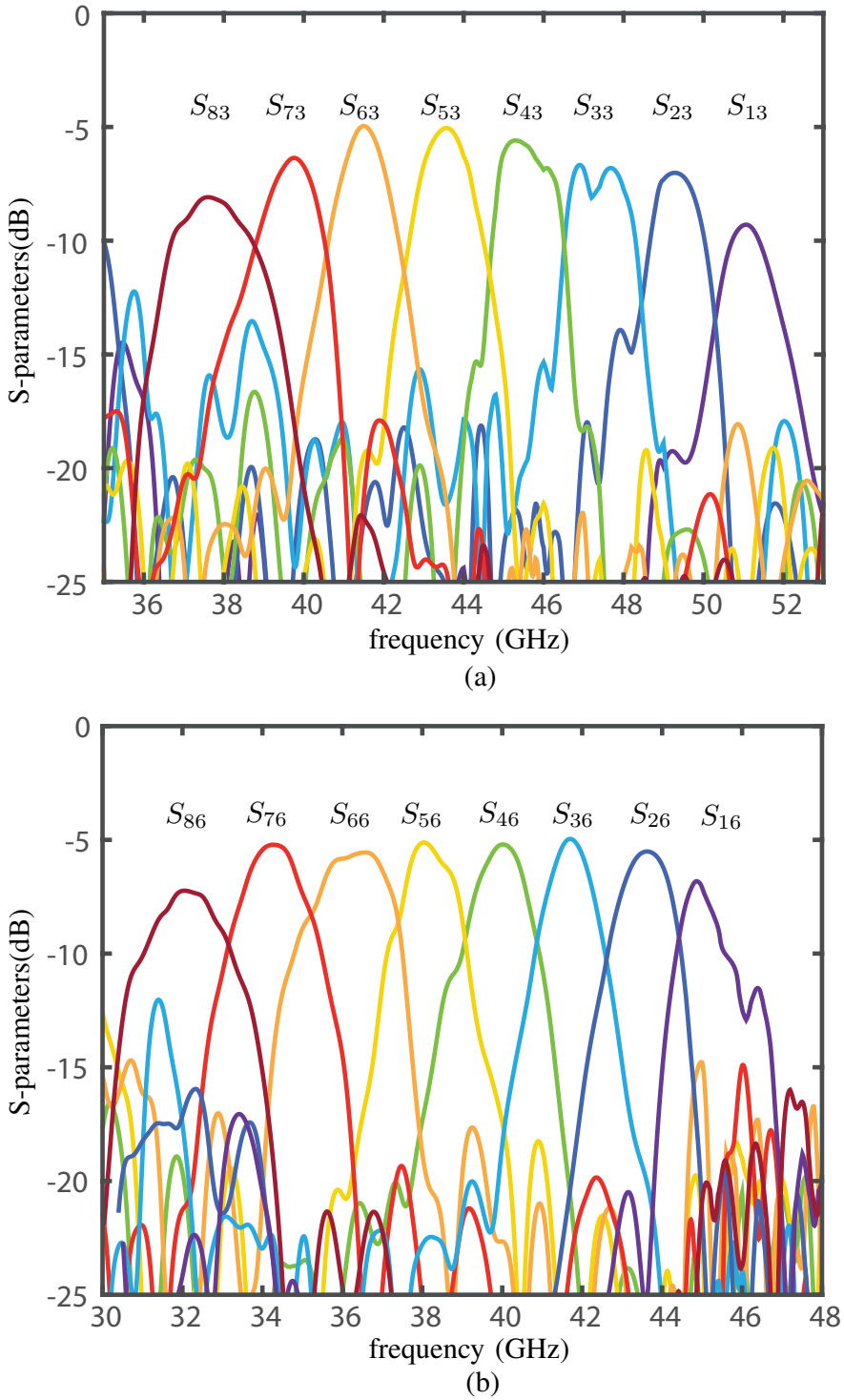

Figure 3.13 Simulated S-parameters involved upon input switching in the uniform frequency resolution design of Fig. 3.10(b). (a) Input at port 3 [overall frequency up-shift, Fig. 3.9(a)]. (b) Input at port 5 [overall frequency down-shift, Fig. 3.9(a)].

and of a local oscillator source for mixing, high design complexity and lack of tunability, restricted bandwidth, and small number of channels.

In this section, we present an alternative energy-detection RTSS, based on an Rotman Lens Spectrum Decomposer (RLSD) [16, 99] . This device resolves all the aforementioned issues of the RTSS in [98], and is hence very promising for future communication systems: 1) it is based on a simple passive structure, the RLSD, requiring neither mixers nor sources, and it is hence inexpensive; 2) it is easy to design and may be tuned in real-time using PIN diodes and switches; 3) it exhibits a very broad bandwidth, due to its true-time delay nature; 4) it may accommodate a great number of channels.

The principle of the proposed real-time spectrum sniffer (RTSS) is presented in Fig. 3.14. The broadband-spectrum (multi-channel) ambient signal to sniff is picked up by an omnidirectional antenna, amplified and passed through a real-time spectrum decomposer (RTSD). The RTSD operates like a prism, i.e. separates out in space, towards different output ports, (and in real-time) the different frequencies composing the input signal are corresponding to different communication channels. The so-separated output signals are then detected by power detectors, from which the binary information on the activity (bit 1) or inactivity (bit 0) of all the channels is instantaneously provided in the base-band domain.

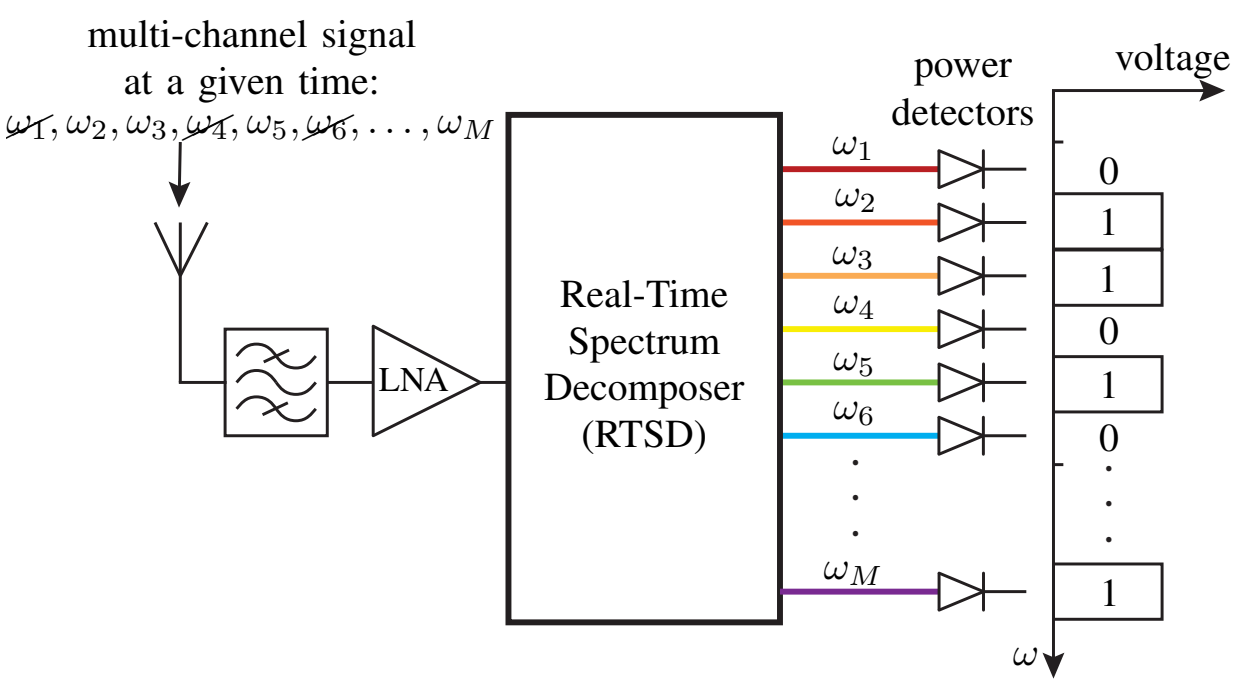

Figure 3.14 Principle of the proposed real-time spectrum sniffer (RTSS).

Figure 3.15(a) shows the prototype while Fig. 3.15(b) plots the corresponding measured spectrum versus output port number, which agrees very well with the theoretical prediction at least down to −15 dB.

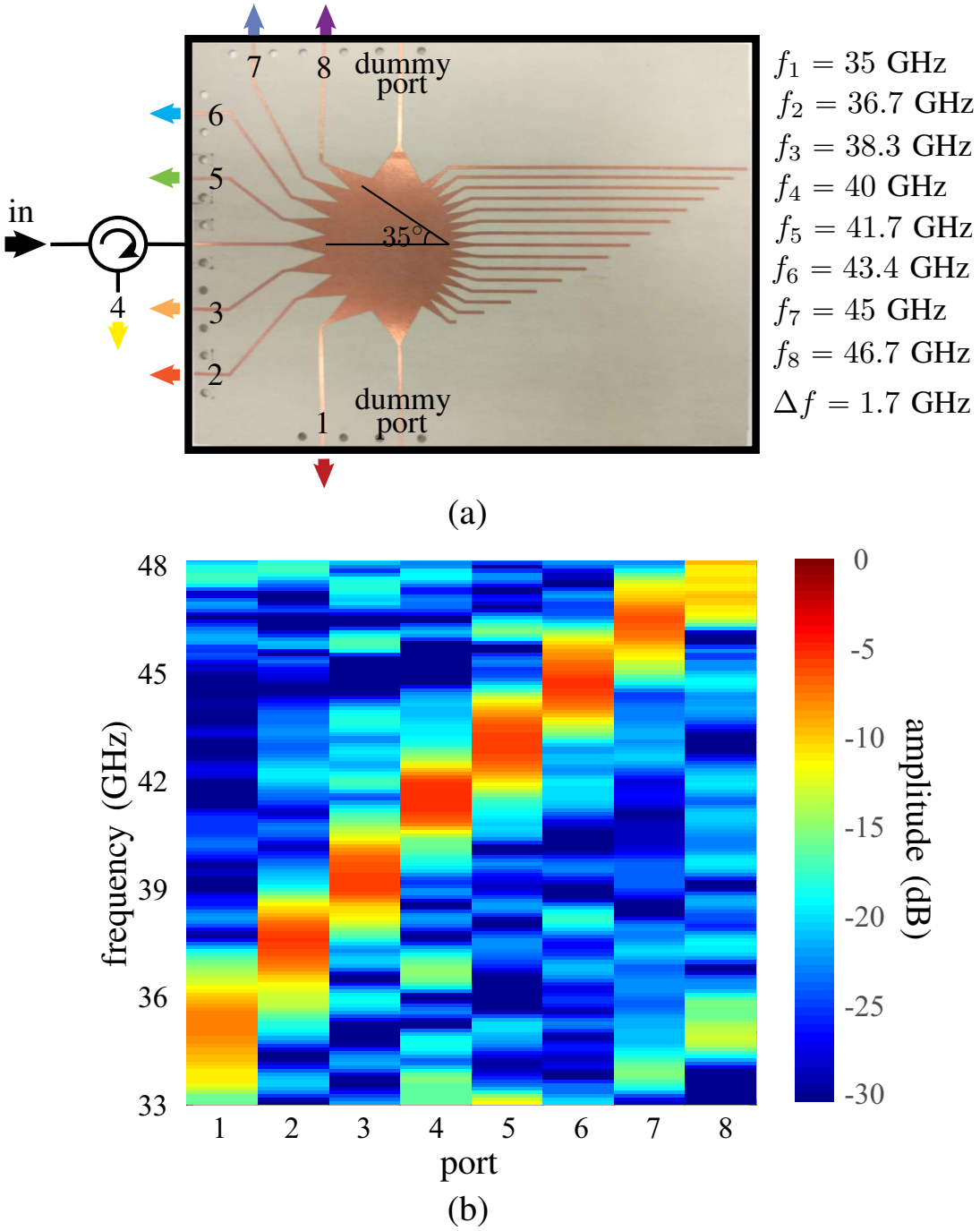

Figure 3.15 Spectral decomposition provided by the lens RTSD ($M = 8$) with $N = 2$ and uniform resolution. (a) Fabricated prototype. (b) Measured spectrum distribution versus lens port number.

Figure 3.16(a) plots the spectra of the signals to detect[2] at the input of the RTSS (Fig. 3.14), corresponding to the 4 active channels $f_2 = 36.7$, $f_3 = 38.3$, $f_5 = 41.7$ and $f_8 = 46.7$ GHz. Figure 3.16(b) plots the spectra of the signals at all the output ports of the fabricated prototype (Fig. 3.15) just before the detectors. It may be observed that each port exhibits an energy peak at the frequency of the corresponding channel if active, as expected, but also includes some energy from other active channels. This is a result of port-to-port leakage due to lens imperfection. For example port 2 (red color), essentially emanating from channel 2 (or f_2) , has an energy peak around f_2, but it also includes some energy at f_2, f_5 and f_8, which correspond to leakage from the active channels 2, 5 and 8. This leakage effect translates into "detection noise" in the overall RTSS. Finally, Fig. 3.16(c) plots the energy detected at all the ports, with successful channel detection ensured with a threshold ideally placed near -9 dB below the level of the strongest signal.

3.6 Conclusion

Given these additional features, adding upon the planar, low-cost, integrable and frequency-scalable features, the RL-SD may find wide applications across the entire electromagnetic spectrum from microwaves through THz to optics using appropriate[3] waveguide structures and technologies.

[2]In a real spectrum sniffing scenario, these signals are all mixed together and are hence indistinguishable from each other.

[3]The design in Fig. 3.10 cannot be straightforwardly transposed to optics. However, it may be *adapted* to this regime using diffused waveguide technology.

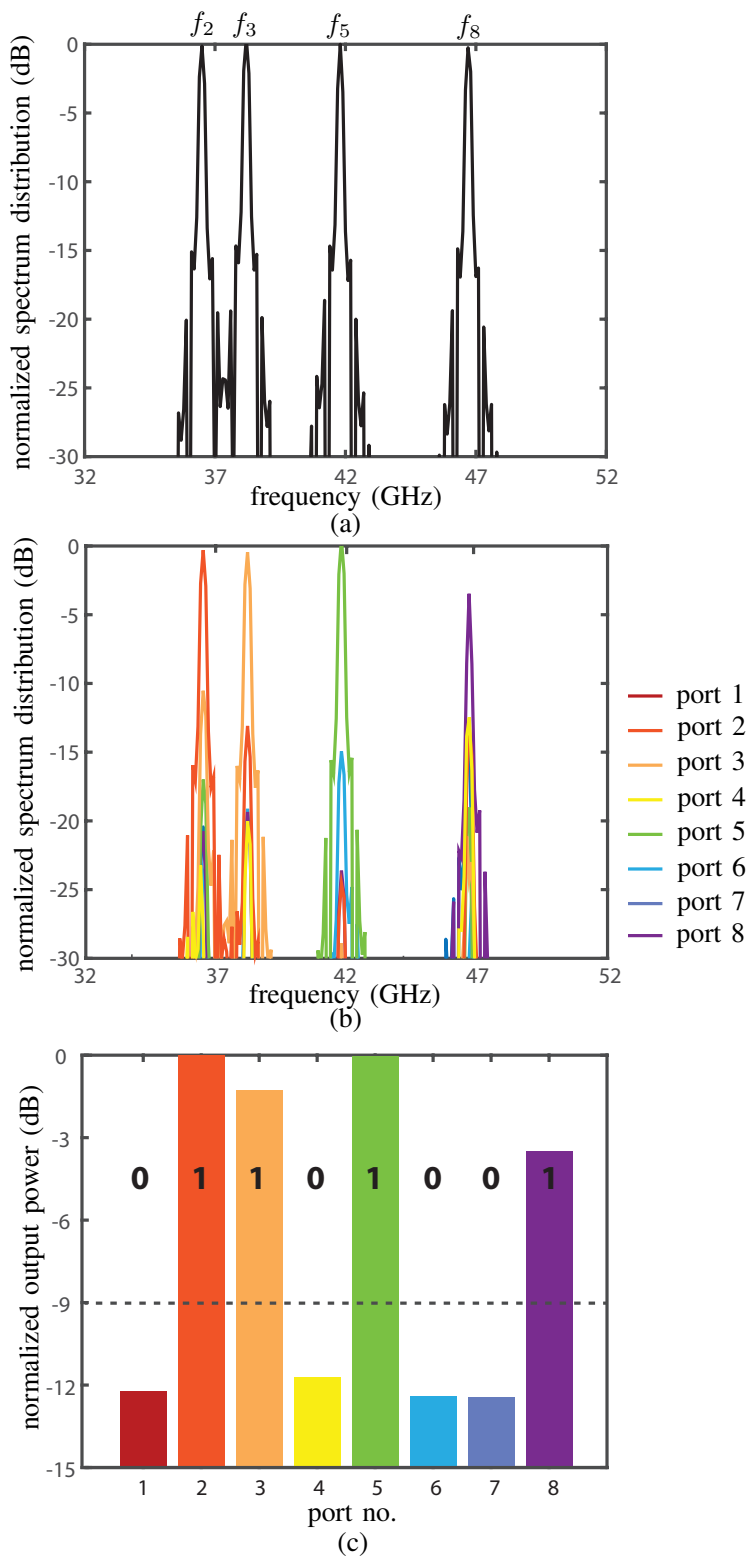

Figure 3.16 Experimental results for the RTSS (Fig. 3.14) with the lens RTSD prototype in Fig. **??**. (a) Spectrum of the multi-channel input signal, with active channels $f_2 = 36.7$ GHz, $f_3 = 38.3$ GHz, $f_5 = 41.7$ GHz and $f_8 = 46.7$ GHz. (b) Spetra of the output signals just before the detectors in Fig. 3.14. (c) Normalized energy of the output signals at all the ports, obtained by integrating the spectra corresponding to each of the ports in (b).

CHAPTER 4 TIME-MODULATED METASURFACE FOR ELECTROMAGNETIC CAMOUFLAGING

Electromagnetic camouflaging refers to concealment technologies whereby objects are made undetectable [100, 101]. It is widely present in nature, for instance in butterflies with wings mimicking leaves, jellyfishes with quasi-transparent bodies, and chameleons that adapt their colors and patterns to the environment [100]. It is also produced by humans, for instance in hunting or military suits and in radar-stealth aircraft and warships [101].

Camouflaging is generally realized by altering the spectrum or power density of the waves scattered by the object to conceal. Such alteration may be accomplished in different manners, including bio-inspired paintings with dazzling or counter-shading patterns [41], absorbing material coatings [42–44], stealth shaping [45], and spectral power redistribution [102, 103].

In past decade, metasurfaces, the two-dimensional counterparts of voluminal metamaterials, have spurred major interest in both the scientific and engineering communities owing to their attractive features of small form profile, low loss, easy fabrication and unprecedented flexibility in controlling the amplitude, phase and polarization of electromagnetic waves [104]. A great diversity of metasurface applications have been reported to date, including for instance polarization transformation [105], wavefront manipulation [106–109], holography [110, 111], nonreciprocity [112, 113], optical force carving [114, 115], and analog computing [116].

Given their multiple benefits, metasurfaces have naturally been considered for electromagnetic camouflaging, based on absorption [117–120], scattering redirection [121, 122], and cloaking [123–125]. However, these technologies are typically limited by issues such as narrow bandwidth, large aperture [122], camouflaging size limitation [126], and camouflaging indifferentiation.

These issues are largely related to the time-invariant nature of the corresponding systems and the related fundamental physical bounds. Revoking the time invariance contraint in time-modulated metasurfaces opens up the possibility to break these bounds and achieve new functionalities. A few related applications have already been reported, such as simplified architecture communication [12, 31–33], direction-of-arrival (DoA) estimation [34], nonreciprocity [14, 35, 36], and analog signal processing [37], to mention a few.

In this chapter, we present a time-modulated spread-spectrum metasurface active camouflaging technology, which was introduced in [127]. Compared to conventional camouflaging technologies, which are Linear Time Invariant (LTI) and based on energy absorption or an-

gular spreading, the proposed technology spreads the incident energy in terms of temporal spectrum. Besides, this technology modulates the metasurface with a pseudo-random sequence, which spreads the spectrum of the incident wave into a noise-like spectrum with minimal power spectral density, and hence maximal camouflaging performance; this is much more efficient than the utilization of completely periodic modulation sequence, which distributes the energy over a small number of harmonics. Finally, the proposed technology provides the extra features of selective camouflaging and interference immunity. Part of this chapter is excerpted from the author's works [13, 46–48].

4.1 General Concept

The proposed concept of spread-spectrum time-modulated metasurface camouflaging is illustrated in Fig. 5.2. The object to be detected in free space is covered by a metasurface that is modulated by a temporal sequence $m(t)$, where t is time, and that exhibits therefore the reflection coefficient $\tilde{R}(t, \omega)$, where ω is the angular frequency corresponding to the dispersive resonant nature of the scattering particles forming the metasurface. When a harmonic wave $\tilde{\psi}_{\text{inc}}(\omega)$ impinges on this structure, its spectrum gets spread out by the time variation into a noise-like signal, $\tilde{\psi}_{\text{scat}}(\omega)$, with extremely low power spectral density, so that the scattered wave is undetectable to any radar detector without the modulation knowledge.

In addition to its basic camouflaging operation, the spread-spectrum time-modulated metasurface concept offers the smart functionality of selectivity, whereby the object can made detectable by friends (legal detectors) while being camouflaged to foes (illegal detectors). The functionality is provided by leveraging the demodulation scheme of spread-spectrum used in wireless communications, with the spread-spectrum key corresponding to the time-varying reflection coefficient $\tilde{R}(t, \omega)$. Moreover, the spectrum spreading principle makes the illegal detection highly robust to interference.

4.2 Theory

4.2.1 Spectrum Spreading

The time-modulated metasurface spectrum spreading principle may be understood with the help of Fig. 4.2, assuming a time-harmonic incident wave of angular frequency ω_0. If the metasurface reduces to a static perfect electric conductor, as shown in Fig. 4.2(a), the incident wave is scattered back at ω_0 after experiencing phase reversal on the reflector. Similarly, if the metasurface is a static perfect magnetic conductor, as shown in Fig. 4.2(b), the incident

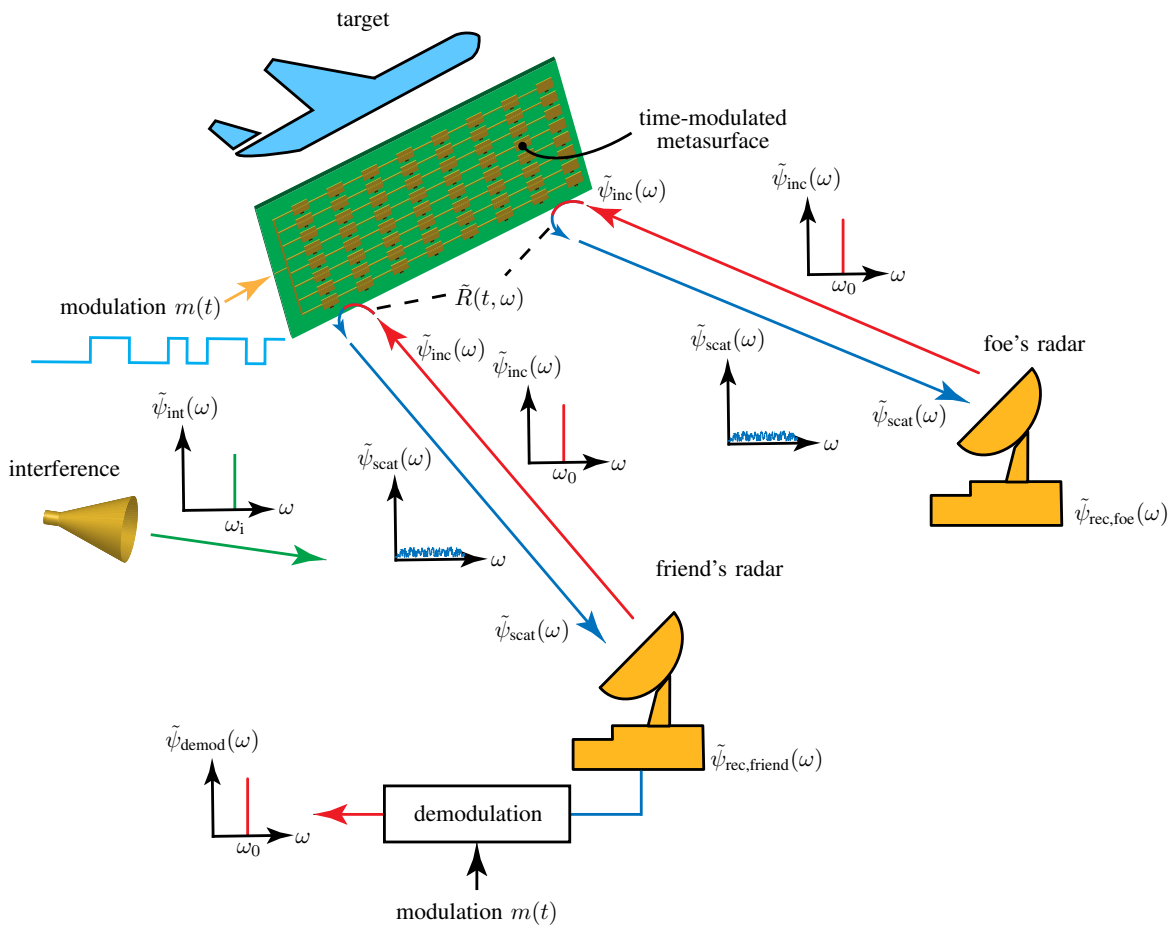

Figure 4.1 Proposed spread-spectrum time-modulated metasurface camouflaging.

wave is scattered back at ω_0, but without experiencing any phase alteration on the reflector. If the metasurface is now modulated so as to repeatedly switch between a PEC reflector and a PMC reflector, as shown in Fig. 4.2(c), it becomes dynamic, or time-varying, with reflection coefficient $R = R(t)$ varying between -1 and $+1$ at minimum time intervals T_{b}, where 'b' stands for 'bit'. The scattered waveform is still a time-harmonic wave of frequency ω_0, but with phase reversal discontinuities that correspond to the switching between the PEC and PMC states.

Considering an incident wave with waveform

$$\psi_{\text{inc}}(t) = A(t)e^{j\omega_0 t}, \tag{4.1}$$

where $A(t)$ is the envelope, and assuming that the metasurface has the constant reflection

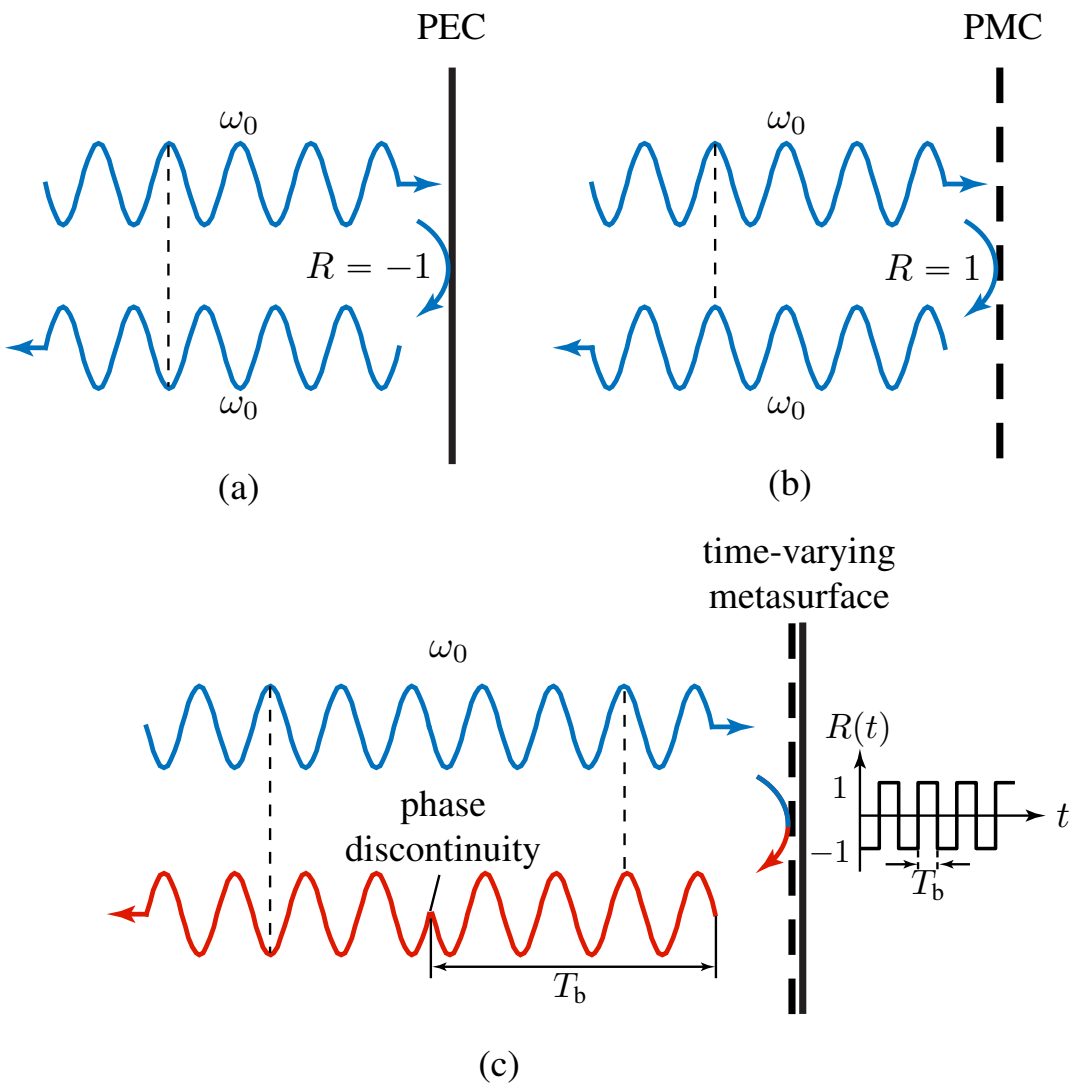

Figure 4.2 Principle of spectrum spreading by the time-modulated metasurface in Fig. 5.2, assuming a time-harmonic interrogating wave of angular frequency ω_0. (a) Static PEC reflector, with reflection coefficient $R = -1$. (b) Static PMC reflector, with reflection coefficient $R = 1$. (c) Time-varying metasurface reflector formed by repeatedly switching the reflection coefficient between the states (a) and (b), so as to make it dynamic, $R = R(t)$.

coefficient $R(t, \omega_0)$ across the bandwidth of $\psi_{\text{inc}}(t)$. The waveform of the scattered wave may be written as

$$\begin{aligned} \psi_{\text{scat}}(t) &= \tilde{R}(t, \omega_0)\psi_{\text{inc}}(t) \\ &= \tilde{R}(t, \omega_0)[A(t)e^{j\omega_0 t}] \\ &= [\tilde{R}(t, \omega_0)e^{j\omega_0 t}]A(t), \end{aligned} \tag{4.2}$$

whose spectrum is

$$\begin{aligned}\tilde{\psi}_{\text{scat}}(\omega) &= \tilde{\tilde{R}}(\omega,\omega_0) * \tilde{\psi}_{\text{inc}}(\omega) \\ &= \tilde{\tilde{R}}(\omega,\omega_0) * \tilde{A}(\omega-\omega_0) \\ &= \tilde{\tilde{R}}(\omega-\omega_0,\omega_0) * \tilde{A}(\omega),\end{aligned} \tag{4.3}$$

where $\tilde{\tilde{R}}(\omega,\omega_0)$ is the Fourier transform of $\tilde{R}(t,\omega_0)$ and $\tilde{A}(\omega)$ is the Fourier transform of $A(t)$. The second equality in (4.3) shows that the spectrum of the scattered wave is the convolution of the spectra of the metasurface reflection coefficient and of the incident wave. Note that although $A(t)$ may a priori represent an arbitrary modulation scheme, some very broadband modulation schemes, such as pulse modulation, would require metasurface bandwidths that may be challenging to realize practically with currently available technology. This thesis focuses on narrow-band $A(t)$. In the particular case where the bandwidth of $A(t)$ reduces to 0, i.e., $A(t) = 1$, Eq. (4.3) reduces to $\tilde{\tilde{R}}(\omega-\omega_0,\omega_0)$, which is the Fourier transform of metasurface reflection coefficient, shifted to the frequency of the incident wave. Therefore, the spectrum of the incident wave is spread out into the spectrum of the modulation, with center frequency ω_0 and power spectral density corresponding to $\tilde{R}(t,\omega_0)$, the spreading corresponding to the introduction of the aforementioned phase discontinuities. Camouflaging according to specification will then be realized by properly designing $\tilde{R}(t,\omega_0)$ in terms of the parameters of the modulating sequence $m(t)$. Note that for (4.2) to be valid, T_b must be much larger than the period of the incident harmonic wave, as will be explained in Sec. 4.2.4.

4.2.2 Selectivity

A friend radar, knowing the spread-spectrum key of the metasurface, $\tilde{R}(t,\omega_0)$, may demodulate the spread signal $\psi_{\text{scat}}(t)$ by the simple post-processing division assuming proper synchronization between the key and scattered signals

$$\psi_{\text{demod}}(t) = \psi_{\text{scat}}(t)\frac{1}{\tilde{R}(t,\omega_0)} = A(t)e^{j\omega_0 t} = \psi_{\text{inc}}(t), \tag{4.4}$$

where the second equality follows from (4.2). Thus the friend radar detects the object that is camouflaged to foe radars, which do not possess the metasurface spread-spectrum key. The proposed metasurface camouflaging technology is thus selective in the sense that it may be restricted to undesired interrogators.

4.2.3 Interference Immunity

The demodulation used for selectivity automatically brings about the extra useful feature of immunity to interference. In the presence of an interfering signal, $\psi_{\text{int}}(t)$, the signal detected by the foe radar is

$$\begin{aligned}\psi_{\text{foe}}(t) &= \psi_{\text{scat}}(t) + \psi_{\text{int}}(t) \\ &= \tilde{R}(t,\omega_0)\psi_{\text{inc}}(t) + \psi_{\text{int}}(t),\end{aligned} \tag{4.5}$$

and the interference further alters the signal received by the foe radar.

In contrast, the signal detected by the friend radar, after its demodulation section, is

$$\begin{aligned}\psi_{\text{friend}}(t) &= \psi_{\text{foe}}(t)\frac{1}{\tilde{R}(t,\omega_0)} \\ &= \left(\tilde{R}(t,\omega_0)\psi_{\text{inc}}(t) + \psi_{\text{int}}(t)\right)\frac{1}{\tilde{R}(t,\omega_0)} \\ &= \psi_{\text{inc}}(t) + \frac{\psi_{\text{int}}(t)}{\tilde{R}(t,\omega_0)} \\ &= \psi_{\text{inc}}(t) + \psi_{\text{int}}(t)\tilde{Y}(t,\omega_0),\end{aligned} \tag{4.6a}$$

with

$$\tilde{Y}(t,\omega_0) = \frac{1}{\tilde{R}(t,\omega_0)}, \tag{4.6b}$$

where the effect of camouflaging is removed, as shown in Sec. 4.2.2, and the interfering wave is multiplied by the inverse of the reflection coefficient. Assuming that $\tilde{R}(t,\omega_0)$ oscillates between -1 and $+1$, as mentioned in Sec. 4.2.1, so does $\tilde{Y}(t,\omega_0)$, and the two functions are exactly the same, i.e., $\tilde{Y}(t,\omega_0) = \tilde{R}(t,\omega_0)$. As a result, the spectrum of the signal detected by the friend radar reads

$$\begin{aligned}\tilde{\psi}_{\text{friend}}(\omega) &= \tilde{\psi}_{\text{inc}}(\omega) + \tilde{\tilde{Y}}(\omega,\omega_0) * \tilde{\psi}_{\text{int}}(\omega) \\ &= \tilde{\psi}_{\text{inc}}(\omega) + \tilde{\tilde{R}}(\omega,\omega_0) * \tilde{\psi}_{\text{int}}(\omega).\end{aligned} \tag{4.7}$$

This results shows that if the bandwidth of the interfering signal is smaller than that of the modulation, as is most common in practice, then that signal is spread out and gets "camouflaged" to the friend, and thence practically harmless to it.

In practice, as will be seen in the experimental part, the magnitude of the reflection coefficient is slightly less than 1 due to dissipative loss, i.e., $|\tilde{R}(t,\omega_0)|$ is slightly smaller than 1, and therefore, $|\tilde{Y}(t,\omega_0)|$ is slightly larger than 1, which tends to increase the effect of the

interference. So, there is an antagonism between the reduction of the interference effect from the demodulation process and the increase of the interference effect due to the issue just mentioned. A good design, with $|\tilde{R}(t,\omega_0)|$ close to 1 will ensure that the former effect largely dominates the latter.

4.2.4 Validity Condition of the Reflection Coefficient Description

Particular attention must be paid to the precise meaning of the function $\tilde{R}(t,\omega_0)$. This expression seems *a priori* absurd since it is meant to represent a *time-varying transfer function*, whereas the concept of transfer function is fundamentally restricted to linear *time-invariant* systems [128]. However, the expression $\tilde{R}(t,\omega_0)$ *does* make perfect sense under the condition that the metasurface modulation occurs on a time scale, T_b [Fig. 4.2(c)], that is much larger than the dispersion or memory time scale, T_d, which is naturally itself larger than the interrogating signal period, $T_0 = \omega_0/(2\pi)$, i.e.,

$$T_\mathrm{b} \gg T_\mathrm{d} > T_0. \tag{4.8}$$

Under this condition, which assumes harmonic excitation (T_0) and discrete reflection switching (T_b), the system may indeed be *considered* purely dispersive (without time variance) on the time scale $t < T_\mathrm{b}$, and purely time-variant (without dispersion) on the time scale $t > T_\mathrm{b}$, as implicitly considered in Sec. 4.2.1 by considering ω_0 as a constant parameter. Let us explain this in some detail.

Its reflection coefficient may then be written in terms of the purely linear time-invariant dispersive transfer function $\tilde{R}(\omega)$, where the mention of time variance has been accordingly suppressed, and we have

$$\tilde{\psi}_\mathrm{scat}(\omega) = \tilde{R}(\omega)\tilde{\psi}_\mathrm{inc}(\omega), \tag{4.9}$$

corresponding in the time domain to[1]

$$\psi_\mathrm{scat}(t) = r(t) * \psi_\mathrm{inc}(t) = \int_{-\infty}^{t} r(t-\tau)\psi_\mathrm{inc}(\tau)\,d\tau, \tag{4.10}$$

where the upper integration limit t ensures causality. Substituting $t-\tau \to \tau'$, and subsequently replacing the dummy variable τ' by τ, yields

$$\psi_\mathrm{scat}(t) = \int_{0}^{\infty} r(\tau)\psi_\mathrm{inc}(t-\tau)\,d\tau. \tag{4.11}$$

[1]Note that the function $r(t)$ has the unit of inverse time (1/s), as required by the differential $d\tau$ in the convolution integral. This is in contrast to $\tilde{R}(\omega)$, which is, according to (4.9), unitless.

Here, the lower integration limit corresponds to the onset of the system, while the upper integration limit corresponds to the duration of the impulse response function $r(t)$, and hence to the transient time of the system. In practice, the function $r(t)$ may be truncated at a time T_d where its average value has decayed to a negligible fraction of the maximum of $r(t)$, and the upper integration limit transforms then as $\infty \to T_\mathrm{d}$.

This scenario is illustrated in Fig. 4.3, which shows that after the impulse response function, obtained by inverse Fourier transforming the reflection coefficient of the metasurface, has decayed to a sufficiently low level, about at time T_d, the output signal $\psi_\mathrm{scat}(t)$ retrieves the waveform of the input harmonic signal $\psi_\mathrm{inc}(t) = \mathrm{e}^{j\omega_0 t}$. Thus, after the transient time T_d, the system may be reasonably approximated as a time-invariant one, and the dispersion can be generally ignored at time scales larger than the modulation, $T_\mathrm{b} \gg T_\mathrm{d}$. If this steady-state condition is not satisfied, then the concept of transfer function does not make any sense and $\tilde{R}(t, \omega_0)$ cannot be used to describe the system[2]. In contrast, if the metasurface were switched at a time scale smaller than T_d, i.e., $T_\mathrm{b} < T_\mathrm{d}$, then the wave would see a change of reflection coefficient before reaching its steady state, and the system would really need to be described as a simultaneously time-variant *and* dispersive one. In practice, the condition in (4.4) can be safely satisfied.

4.3 Modulation Sequence

In this section, we investigate the choice of an optimal time-modulation for the proposed metasurface camouflaging system (Fig. 5.2). An ideal choice would be an infinite-bandwidth white noise, since such a modulation, assuming finite energy, would lead to a uniform zero spectral density, and hence to perfect camouflaging. However, practically, the bandwidth of the modulation is limited by the speed of the switching elements, which will be PIN diodes in our experiment (Sec. 4.5). Moreover, the selectivity functionality (Sec. 4.2.2) and the interference immunity property (Sec. 4.2.3) of the system require some level of coherence, related to the condition (4.8).

We shall therefore use the pseudo-random noise periodic modulation scheme shown in Fig. 4.4 for $m(t)$. Figure 4.4(a) plots this function. It consists of rectangular pulse pseudo-randomly oscillating between the values $+1$ and -1 at the bit rate or switching frequency of $f_\mathrm{b} = 1/T_\mathrm{b}$, and with a bit period of N bits, or time period of $T_\mathrm{m} = NT_\mathrm{b}$, corresponding to the function repetition frequency $f_\mathrm{m} = 1/T_\mathrm{m}$. Figure 4.4(b) shows resulting scattered waveform, which is

[2]One should beware of confusing $\tilde{R}(t)$ and $r(t)$: $r(t)$ is the impulse response of the time-invariant metasurface while $\tilde{R}(t)$ represents the time-varying reflection coefficient of the meatsurface under the condition of (4.8).

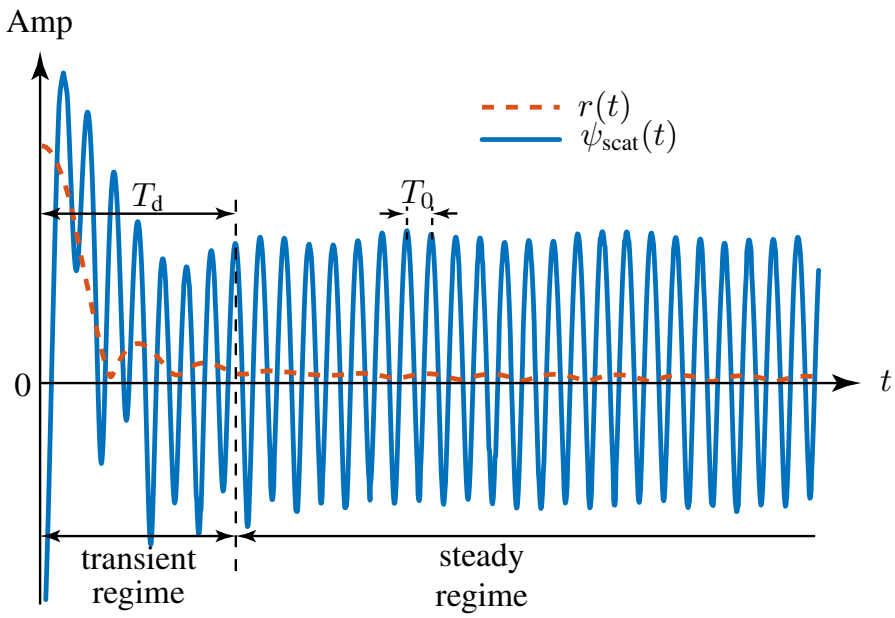

Figure 4.3 Transient regime and steady-state regime corresponding to the time-invariant dispersive nature of the metasurface within the time T_{b} under the excitation $\psi_{\text{inc}}(t) = \mathrm{e}^{j\omega_0 t}$.

a harmonic wave with π-phase discontinuities corresponding to the switching times between the states ± 1.

The pseudo-random function, as the camouflaging key, should change from time to time to minimize the chances of foe radars to find it. Therefore, it does not have a uniquely determined spectrum, $\tilde{M}(\omega)$. However, the function $m(t)$ can be generally represented by its *autocorrelation function* [129]

$$\begin{aligned} s_{\text{p}}(t) &= \int_{-\infty}^{+\infty} m(\tau) m(t+\tau)\, d\tau \\ &= -\frac{1}{N} + \frac{N+1}{N} \sum_{n=-\infty}^{+\infty} \Lambda\left(\frac{t - nNT_{\text{b}}}{T_{\text{b}}}\right), \end{aligned} \tag{4.12a}$$

which is also of period $T_{\text{m}} = NT_{\text{b}}$, and where $\Lambda(\cdot)$ is the triangular function

$$\Lambda(t) = \begin{cases} 1 - |t| & \text{if } t \leq 1, \\ 0 & \text{if } t > 1, \end{cases} \tag{4.12b}$$

which essentially results from the correlation integral of the rectangular pulses composing $m(t)$ (Fig. 4.4).

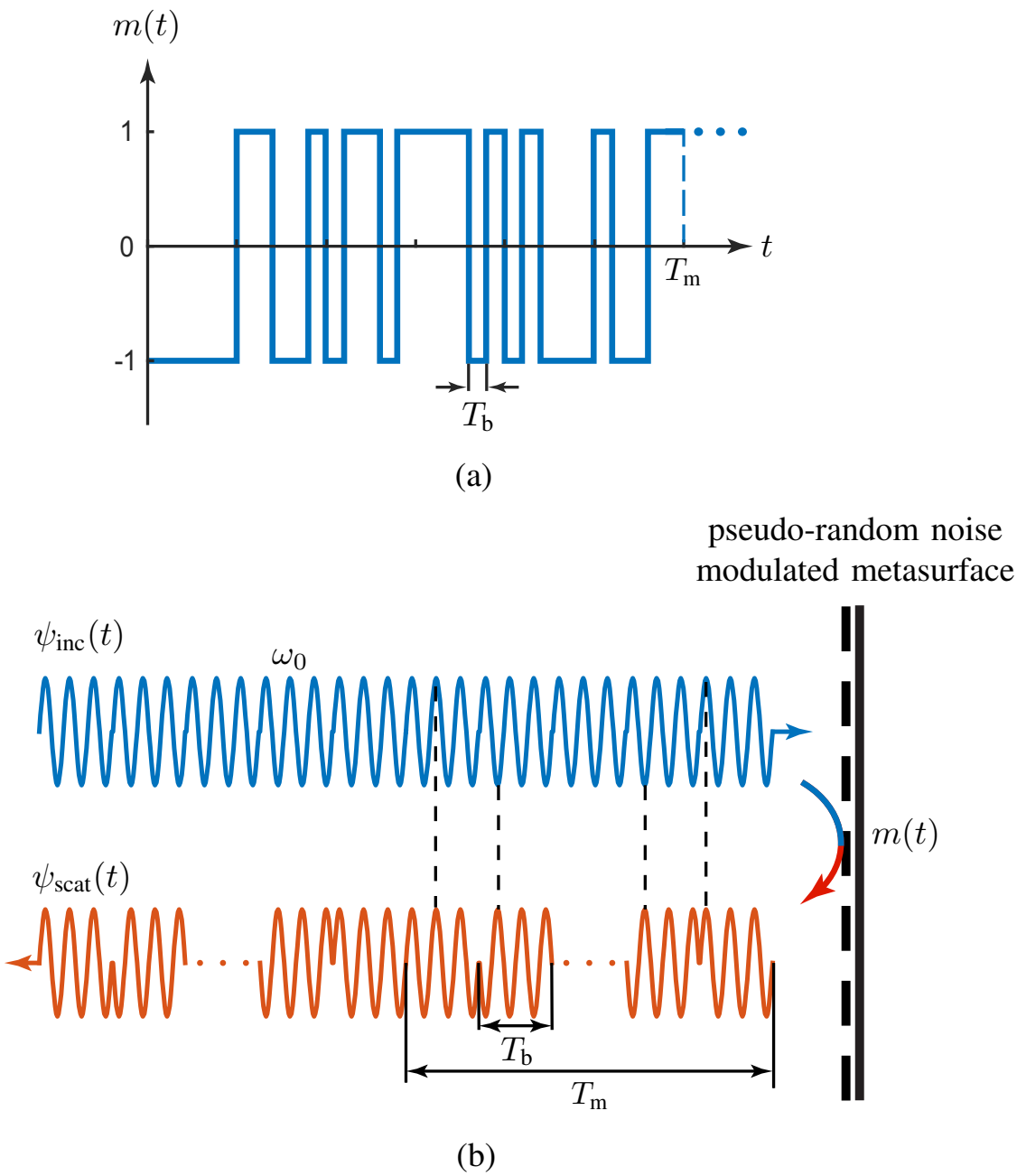

Figure 4.4 Practical modulation for the proposed system. (a) Modulation function, $m(t)$, consisting of a periodically repeated pseudo-random noise sequence of N bits with bit duration T_b, and hence period $T_\mathrm{m} = NT_\mathrm{b}$ (one period shown). (b) Corresponding scattered waveform.

The Fourier transform of (4.12) is the *power spectral density* function of $m(t)$, which reads [129]

$$\tilde{s}_{\mathrm{p}}(f) = \frac{1}{N^2}\delta(f) + \frac{N+1}{N^2}\sum_{\substack{n=-\infty \\ n\neq 0}}^{+\infty} \mathrm{sinc}^2\left(\frac{n}{N}\right)\delta\left(f - \frac{n}{N}f_{\mathrm{b}}\right), \tag{4.13a}$$

and

$$\mathrm{sinc}(f) = \begin{cases} 0 & \text{if } f = 1, \\ \dfrac{\sin(\pi f)}{\pi f} & \text{otherwise.} \end{cases} \tag{4.13b}$$

The power spectral density function (4.13) $\tilde{s}_{\mathrm{p}}(f)$ is plotted in Fig. 4.5. This function is *discrete*, due to the periodic nature of $s_{\mathrm{p}}(t)$, with period $1/T_{\mathrm{m}} = f_{\mathrm{m}} = f_{\mathrm{b}}/N = 1/(NT_{\mathrm{b}})$. It has the envelope $\frac{N+1}{N^2}\mathrm{sinc}^2(f/f_{\mathrm{b}})$, with maximum value $\frac{N+1}{N^2}$, main-lobe bandwidth $2f_{\mathrm{b}}$, and DC value $1/N^2$.

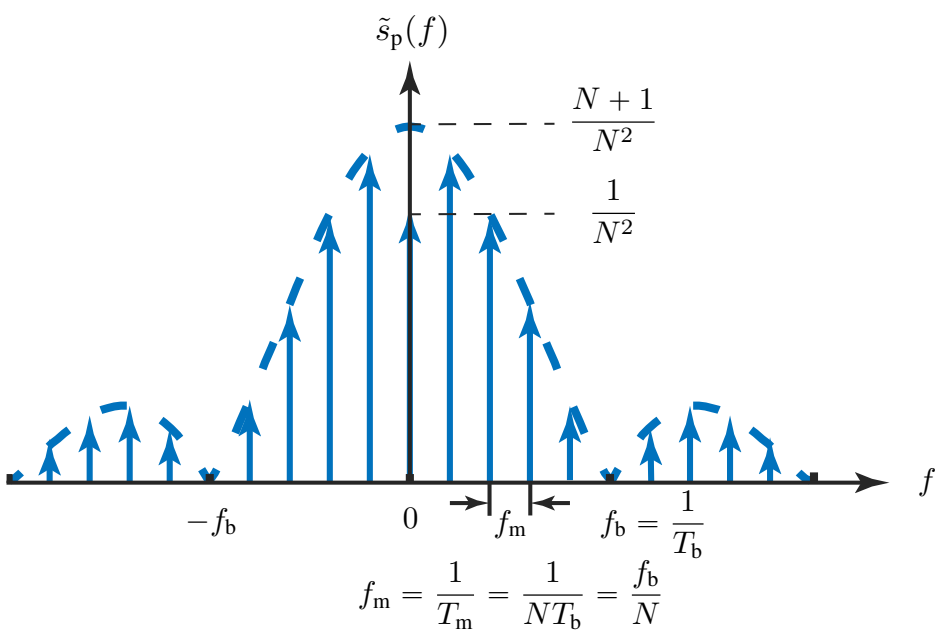

Figure 4.5 Power spectral density function $\tilde{s}_{\mathrm{p}}(f)$, given by Eq. (4.13), for the modulation function $m(t)$ in Fig. 4.4(a).

This behavior may be explained as follows:

- The nonzero $1/N^2$ value at $f = 0$ (DC component) is due to the fact that N, as the *length of a pseudo-random noise sequence*, is an odd number [129], so that there is always an imbalance between the number of -1 bits and the number of $+1$ bits, an effect that progressively vanishes by dilution as $N \to \infty$;
- As N increases, assuming fixed switching frequency, the frequency interval between the

function samples ($1/T_\mathrm{m} = f_\mathrm{m} = f_\mathrm{b}/N$) reduces at the rate of $1/N$, and therefore the spectral sample density – proportional to the number of samples within the first lobe of the sinc squared envelope – increases at the same rate (N). If the input power is fixed, as may be assumed for given radar interrogator in the application of interest, then the power level of each sample must then be reduced by the same factor (N). This is indeed what is seen in Fig. 4.5, considering that $\lim_{N\to\infty}(N+1)/N^2 = 1/N$. So, *increasing the length of the pseudo-random noise sequence results in decreasing the level of the power spectrum density function.*

- Finally, decreasing the bit length (T_b), or equivalently increasing the bit rate (f_b), for a fixed sequence length (N), increases the fastest variation of $m(t)$ and hence *spreads out its spectrum* – in particular the spectral width of the sinc squared main lobe – while decreasing the sample density, which depends only on the modulation period (T_m) at the same rate (f_b).

4.4 Simulation Results

For simplicity, we are assuming that the incident wave is a non-modulated harmonic wave, i.e., $A(t) = 1$ and $\psi_\mathrm{inc}(t) = e^{j\omega_0 t}$ in (4.1). Considering an incident harmonic wave of frequency $f_0 = 10$ GHz (Fig. 4.4), the power spectral density of the wave scattered by the modulated metasurface may be obtained from Eq. (4.3) as

$$\tilde{s}_\mathrm{scat}(\omega) = |\tilde{\psi}_\mathrm{scat}(\omega)|^2 = |\tilde{\tilde{R}}(\omega-\omega_0,\omega_0)|^2 = \tilde{s}_\mathrm{p}(\omega-\omega_0), \tag{4.14}$$

where $\tilde{s}_\mathrm{p}(\omega)$ is given by (4.13) with $f = \omega/(2\pi)$.

Figure 4.6 plots the power spectral density of the scattered wave for different values of the parameters N and f_b to illustrate the results of Sec. 4.3. Figure 4.6(a) shows how the level of the spectral power density decreases as N increases, without change of bandwidth for fixed f_b. Figure 4.6(b) shows how the bandwidth (main lobe) of the power spectral density increases as f_b increases, without change of the maximum[3] for fixed N.

Figure 4.7 plots the power spectral density of imperfect modulation for the parameter pair $(N, f_\mathrm{b}) = (127, 5\text{ MHz})$ (blue curves in Fig. 4.6). Figure 4.7(a) plots the power spectral density of unbalanced amplitude modulation, where the negative value of $R(t)$, R_n, is fixed to -1 while the positive value of $R(t,\omega_0)$, R_p, reduces from the ideal value 1 to imperfect value 0. It shows that as R_p reduces, the power spectral density of centering harmonic

[3]Strictly, $\tilde{s}_\mathrm{scat}(f_0) = 1/N^2 = 6.2\cdot 10^{-5} \approx 0$ (or -42.1 dB, not visible in the figure), and the maximum refers here to the envelope maximum, which is very close to the level of the frequency samples nearest to f_0.

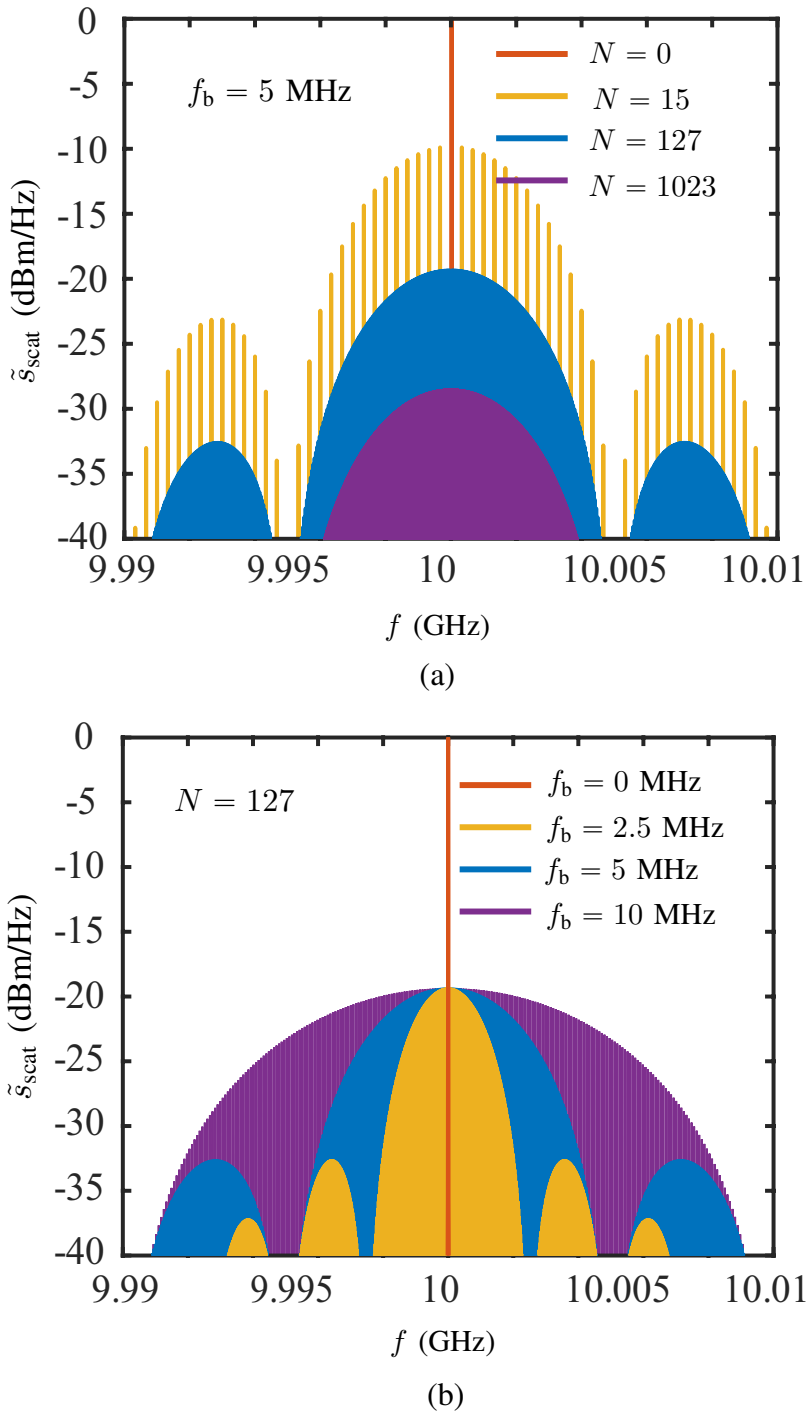

Figure 4.6 Parametric study of the power spectral density of a harmonic wave scattered by the metasurface, given by Eq. (4.14). (a) Spectrum level decrease with the increase of the modulation sequence length, N. (b) Spectrum spreading with the increase of the modulation frequency, f_{b}.

wave increases while the power spectral density of the spread-spectrum reduces. Similarly, Fig. 4.7(b) plots the power spectral density of unbalanced phase modulation, where the negative value of $R(t)$, R_n, is fixed to -1 while the positive value of $R(t, \omega_0)$, R_p, changes from the ideal value $1\angle 0°$ to unbalanced phase value $1\angle 90°$. It shows that as the phase of R_p from 0 to 90°, the power spectral density of centering harmonic wave also increases while the power spectral density of the spread-spectrum also reduces.

Figure 4.8 compares the power spectral densities received by the foe radar and by the friend radar for the parameter pair $(N, f_\mathrm{b}) = (127, 5\text{ MHz})$ (blue curves in Fig. 4.6). Figure 4.8(a) predicts the camouflaging selectivity of the metasurface system: the foe radar receives an undetectable spectrum spread signal, whereas the friend radar perfectly detects the object covered by the metasurface. Figure 4.8(b) predicts the interference immunity of the metasurface system: the foe radar detects only the interference signal, a harmonic wave at 10.001 GHz, which appropriately delivers false information about the object, whereas the friend radar does not see the interference signal while still perfectly detecting the object.

4.5 Experiment Results

A time-modulated metasurface is designed, fabricated and measured to demonstrate the proposed spread-spectrum camouflaging system. Figure 4.9 shows the layout of the metasurface prototype. The metasurface is designed on a Rogers 6002 substrate with permittivity of 2.94 and thickness 0.76 mm. Figure 4.9(a) shows the overall metasurface. The bottom side of it is a ground plane and the top side is an 8×8 array of scatterers interconnected by bias lines that are meet to a single modulation point at one side of the structure. The unit cell consists of a rectangular patch, with the bias line connection at both sides of it and a PIN diode switch (MACOM MADP-00090714020) interconnecting the patch and the ground plane through a shorted metalized via. Figure 4.9(b) provides the parameter values of the unit cell for operation at 10 GHz.

Figure 4.10 shows the simulated electrical field distribution around the unit-cell patch for the PIN diodes switched to the ON and OFF states. When the diodes are OFF, the patches are isolated from the ground and resonate, which provides quasi-PMC reflection, while when the diodes are ON, the patches are shorted to the ground, which provides a quasi-PEC reflection.

Figure 4.11 plots the simulated reflection coefficients for the 2 modulation states of the metasurface. The amplitude of this coefficient is close to 1 for both states, while the phase difference between the two states is around π at the operation frequency (10 GHz), as desired.

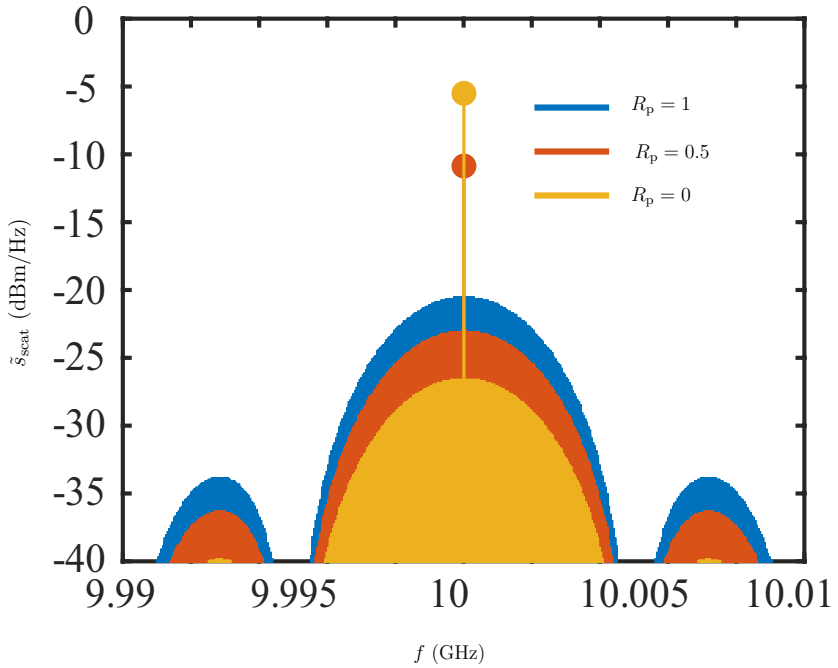

(a)

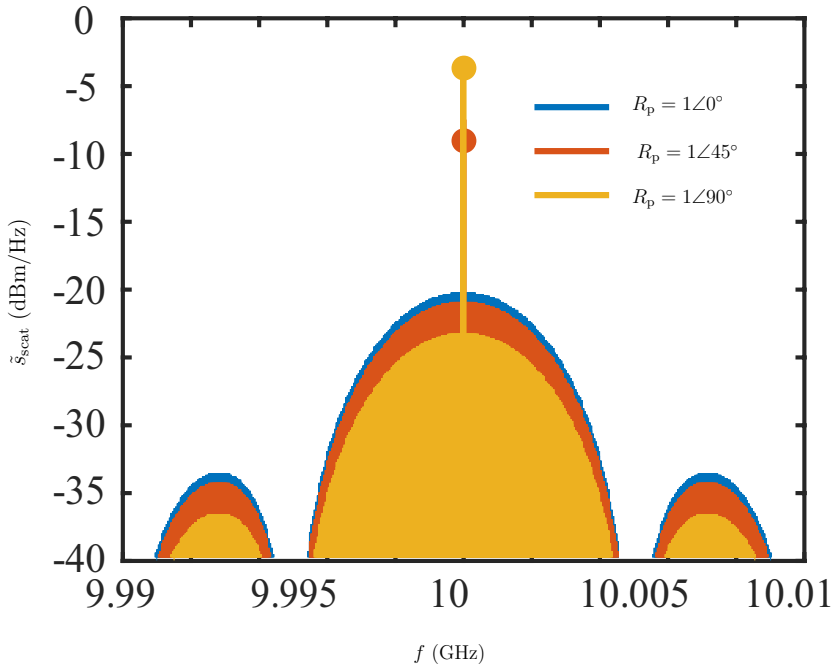

(b)

Figure 4.7 Power spectral density of a harmonic incident wave scattered by the imperfect modulated metasurface, given by Eq. (4.14). (a) Imperfect amplitude modulation. (b) Imperfect phase modulation.

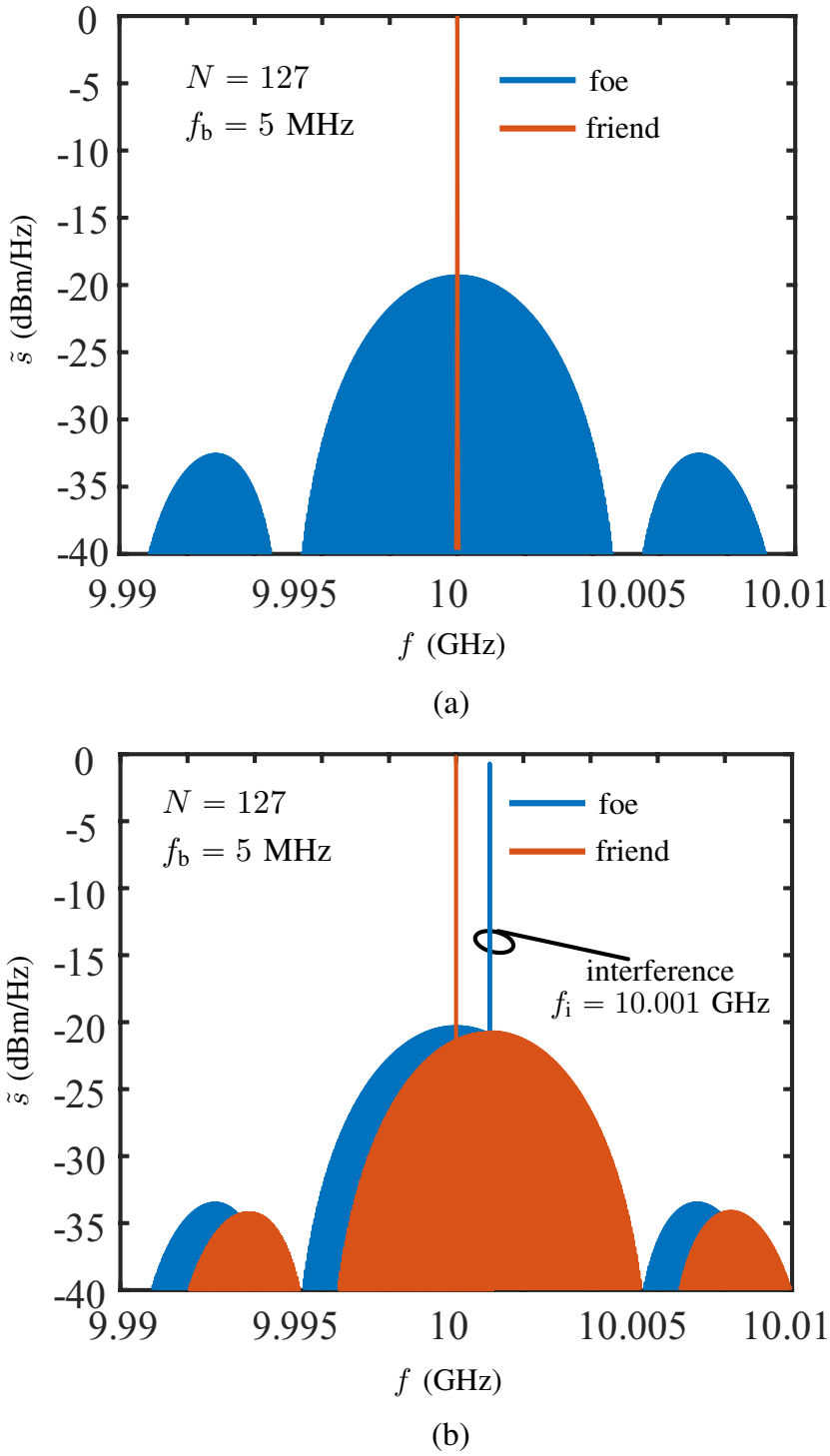

Figure 4.8 Comparison of the power spectral densities received by the foe radar and by the friend radar (Fig. 4.2). (a) Camouflaging selectivity, computed from Eq. (4.4). (b) Interference immunity, computed from Eq. (4.7).

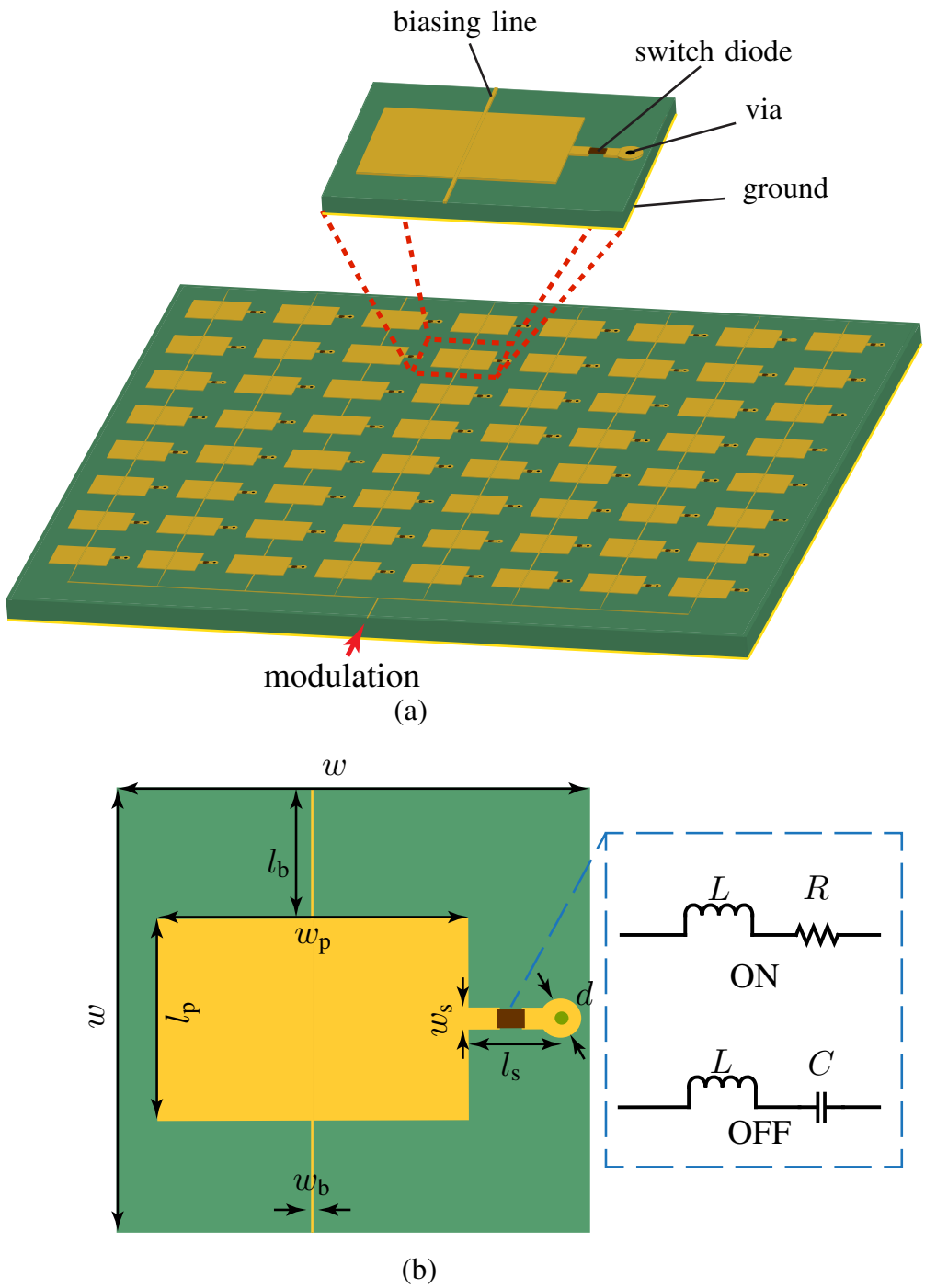

Figure 4.9 Layout of the metasurface prototype. (a) Overall view. (b) Unit cell. The parameter values are $w = 15$ mm, $w_\mathrm{p} = 7.6$ mm (resonant length), $l_\mathrm{p} = 5.6$ mm, $l_\mathrm{b} = 4.7$ mm, $w_\mathrm{s} = 0.5$ mm, $w_\mathrm{b} = 0.2$ mm, $l_\mathrm{s} = 1.8$ mm, $d = 0.4$ mm, $L = 30$ pH, $R = 7\ \Omega$ and $C = 28$ fF.

The off state features a slightly larger loss than on state, due to its resonant nature, which is apparent in Fig. 4.10. The slight loss in the on state is mostly due to the resistive loss in

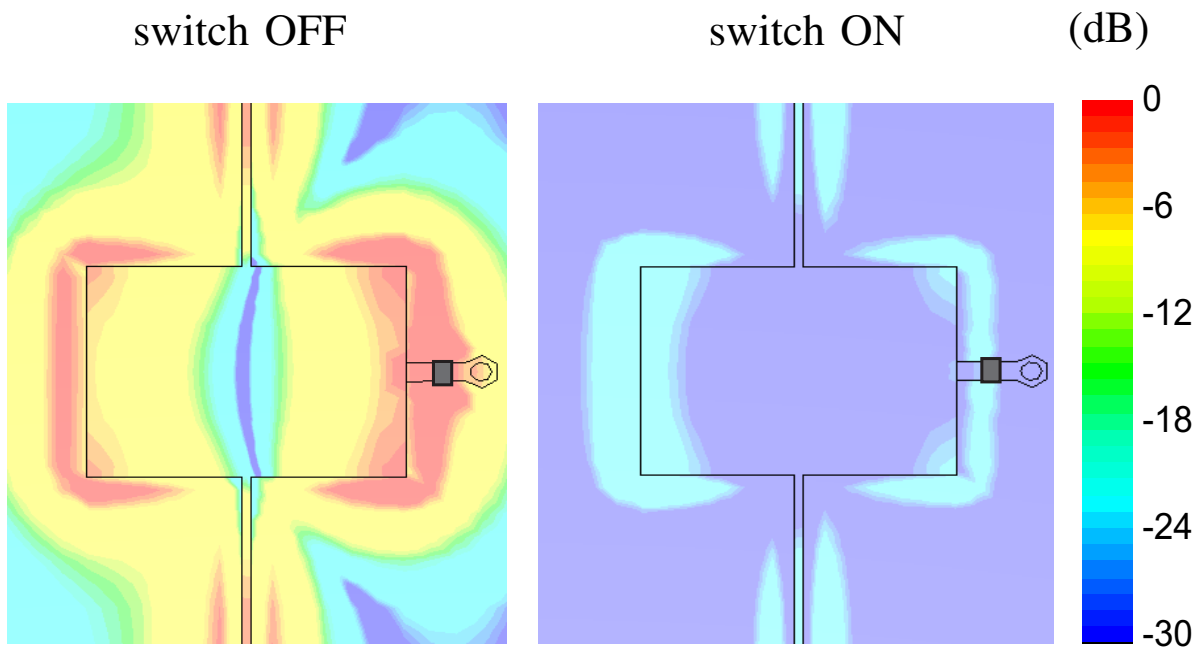

Figure 4.10 Simulated (FDTD – CST Microwave Studio) electrical field distribution around the patch of the unit cell in Fig. 4.9 for the PIN diodes switched to the ON and OFF states.

the diodes.

The imbalance between the on- and off-state reflective amplitudes (Fig. 4.11) may affect the camouflaging performance. Indeed, this imperfection typically alters the balance between the $+1$ (on-state) and -1 bits (off-state) in the modulation function [Fig. 4.4(a)]. This introduces a DC component in the scattered wave (here positive due to the higher reduction of the -1 compared to the $+1$ bits), and hence at the center frequency of the metasurface, which could ultimately reveal to the foe the presence of the object. The level of imbalance may be reduced by adding a resistor in series with PIN diode or by using a substrate of lower loss. However, the level of unbalance seen in Fig. 4.10 was found to be acceptable for the current proof of concept, as will be seen shortly. Inverse Fourier transforming $S_{11}(\omega)$ for each of the two states yields $T_{\mathrm{d(PEC)}} \approx 0$ and $T_{\mathrm{d(PMC)}} \approx 0.17$ ns, these time are much smaller than the response time of the PIN diodes, $\tau_{\mathrm{d}} \approx 2$ ns. Therefore, in practice, it is the response of the diodes that represents the lower bound for the modulation time, i.e., $T_{\mathrm{b}} \gg \tau_{\mathrm{d}} > T_{\mathrm{d(PMC)}} > T_{\mathrm{d(PEC)}}$.

Figure 4.12 shows the fabricated 10-GHz prototype while Fig. 4.13 shows the experimental set-up used to demonstrate the metasurface system. The metasurface is placed on a piece of 70×70 cm^2 absorbing material on the floor. It is modulated by a pseudo-random noise sequence of length $N = 127$ and rate $f_{\mathrm{b}} = 5$ MHz provided by an arbitrary signal generator. A pair of planar Vivaldi antennas with 4.3 dB gain, 36.8° 3-dB beamwidth and separation 28 cm,

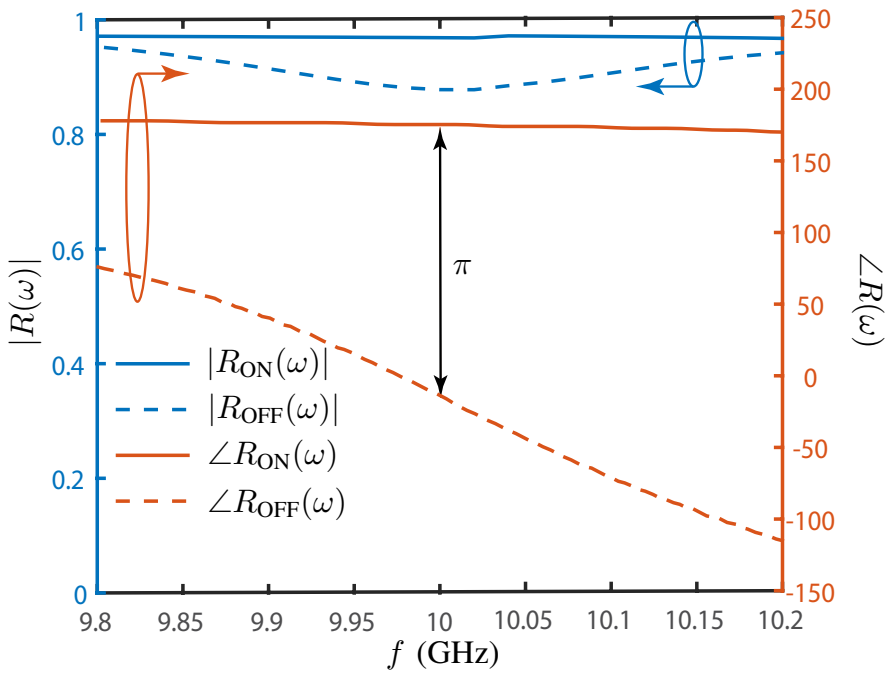

Figure 4.11 Simulated reflection coefficient of the metasurface prototoype in Fig. 4.9 for the PIN diodes switched to the ON and OFF states, corresponding to the current distributions in Fig. 4.10.

placed 110 cm above the metasurface in the far-field, simulates an arbitrary interrogating radar. The 10 GHz harmonic wave is generated by a signal generator and sent towards the metasurface by the transmitting antenna. The wave scattered by the metasurface is then collected by the receiving antenna, passed through a bandpass filter that suppresses the out-of-band noise, and measured by a vector signal analyzer with a bandwidth resolution 5 kHz.

Figure 4.14 plots the power spectral densities of the signals detected by the foe and friend radars. Figure 4.14(a) demonstrates the camouflaging selectivity of the system. When the metasurface is not modulated, the receiver perfectly detects the 10 GHz harmonic wave sent by the transmitter and scattered by the metasurface (green curve), with a signal-to-noise ratio (SNR) of 52.7 dB. When the metasurface is modulated, the scattered wave is spread out into a relatively broad band signal of 10 MHz bandwidth and with level reduced by 18.2 dB by the spectrum spreading operation.

The level of -18.2 dB (ratio of 0.015) is contaminated by external effects associated with the measurement setup, which are unrelated to the metasurface system itself. These effects include spurious coupling between the transmitting and receiving antennas and from scattering from the surrounding objects in the room. The strongest of these effects is the

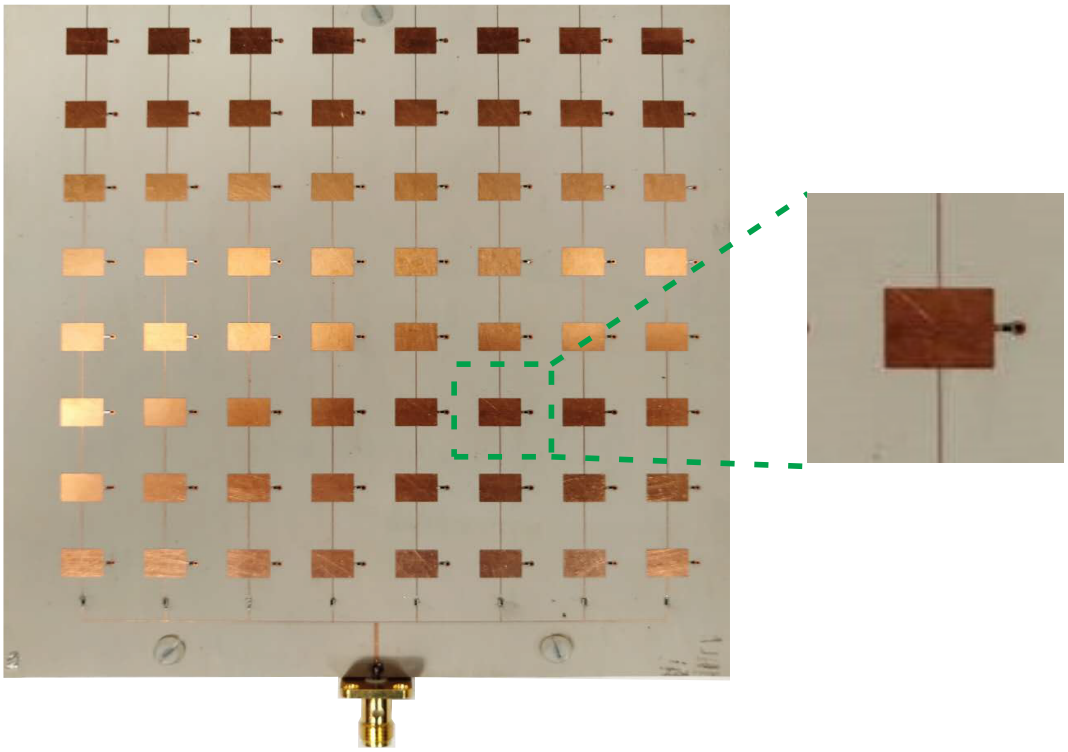

Figure 4.12 Fabricated metasurface prototype, corresponding to Fig. 4.9.

antenna coupling, whereby a substantial amount of the transmitted signal directly leaks into the receiving antenna without being reflected by the metasurface. This coupling level may be evaluated by subtracting the transfer functions measured with the metasurface and with the metasurface replaced by absorbing material; we found $S_{21(\text{abs})}(\omega_0) - S_{21}(\omega_0) = (-67.3) - (-47.6) = -19.7$ dB (ratio of 0.011). Therefore, the reflection level that is really produced by the metasurface system at ω_0 is obtained by subtracting the mutual coupling effect, i.e., $0.015 - 0.011 = 0.004$, or -24 dB (ratio of 0.004), which is lower than the power spectral density around ω_0. The remaining energy at -24 dB may be due to the imbalances in the amplitude and phase functions (Fig. 4.14(a)). So, the metasurface camouflaging effect is even much stronger than it appears in Fig. 4.14(a) after the external effect of antenna coupling has been removed.

Synchronization for demodulation is performed by correlating the key signal and the picked-up signal, with the time corresponding to maximal value providing the synchronization timing. Upon demodulation according to (4.4), the friend radar recovers the transmitted harmonic signal, with an SNR of 33.6 dB, and hence detects the object, which demonstrates the selectivity property of the system.

Figure 4.14(b) shows the interference response of the system after demodulation to an inter-

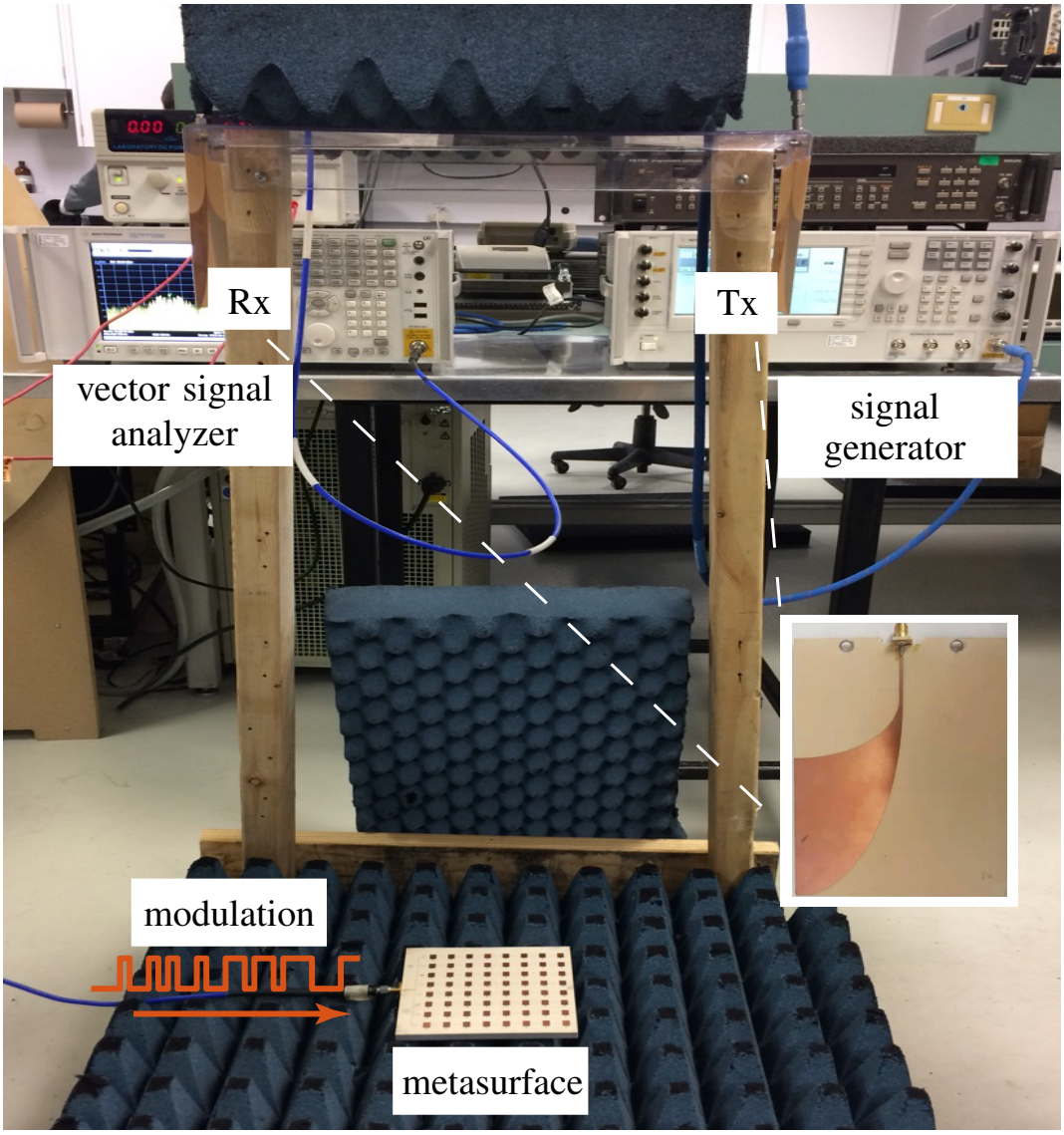

Figure 4.13 Experimental set-up.

fering signal of $f_{\mathrm{i}} = 10.001$ GHz according to (4.7). The inferering signal is added digitally on computer in post-processing to simulate a practical one. It shows that whereas the foe radar is still unable to detect the object and additionally strongly detects the interfering signal, the friend radar does not detect this interfering signal at all while still detecting the object, with an SNR of around 19.2 dB.

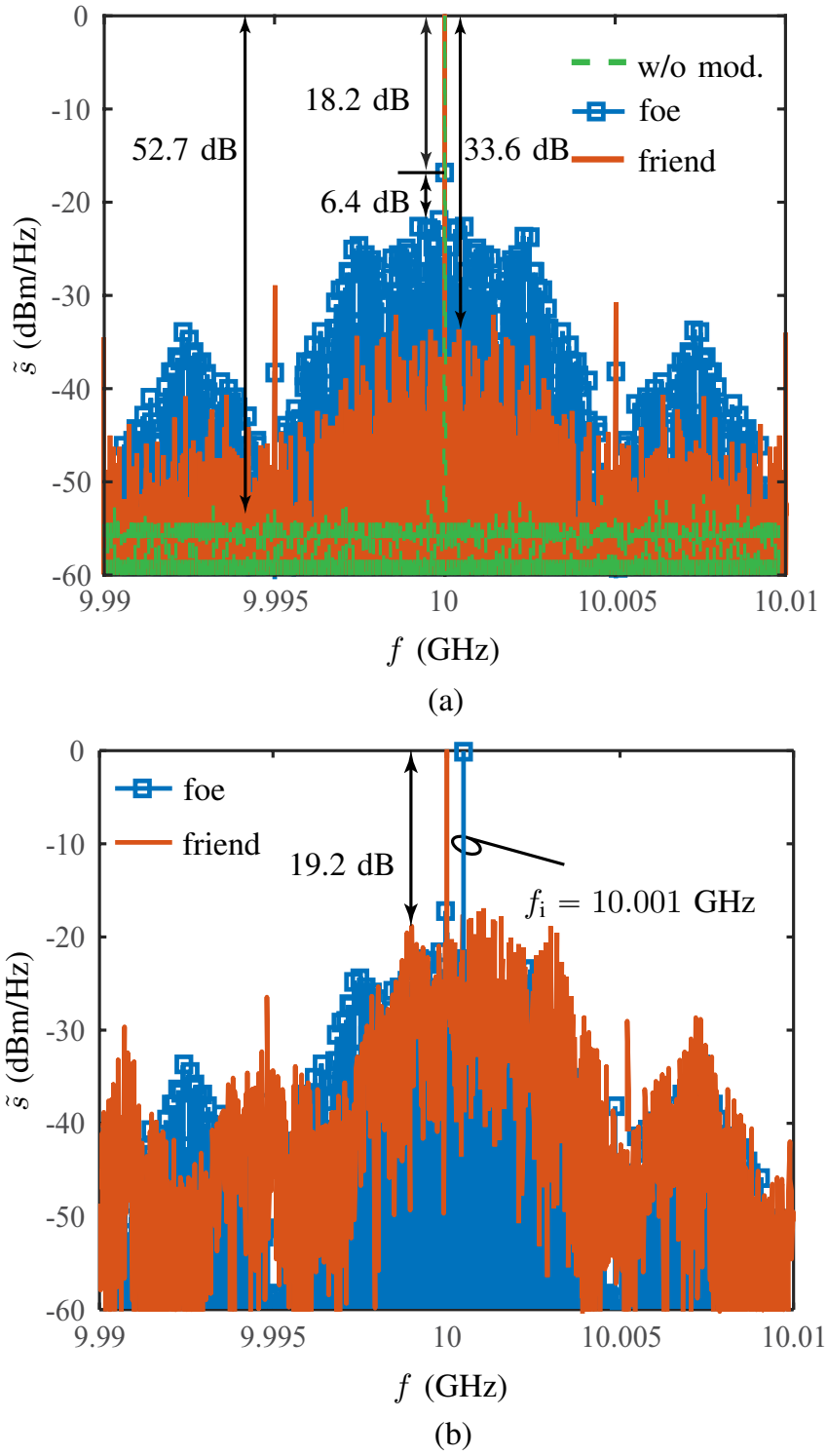

Figure 4.14 Experimental results, corresponding to the simulations in Fig. 4.8. (a) Camouflaging selectivity. (b) Interference immunity.

4.6 Conclusion

A time-modulated metasurface-based camouflaging technology using time-alternating PEC-PMC unit cell elements and pseudo-random modulation has been proposed, analyzed, simulated and experimentally demonstrated in this chapter. Compared to other reported camouflaging technologies, it shows its unique features of noise-like spread-spectrum, selective camouflaging and interference immunity capability. Given these promising features, as well as its potential efficiency, this technology may find wide applications in both defense and civilian applications.

CHAPTER 5 CONCLUSION AND FUTURE WORK

5.1 Conclusion

This thesis presents real-time microwave signal processing (R-MSP) techniques and applications. Two complementary solutions including dispersion engineering and time modulation are studied for different purpose. The chapters corresponding to selected articles represent novel R-MSP concepts, strategies and systems.

Chapter 2 presents a branch-line couplers and resonant loops based R-MSP microwave Hilbert transformer, and explains the physical operation of this transformer, using both time-domain and steady-state perspectives [38].

Chapter 3 presents an enhanced design of the planar Rotman lens spectrum decomposer (RL-SD) in terms of resolution flexibility, input port position arbitrariness and frequency range and resolution tunability. The resolution flexibility enhancement consists in allowing different frequency sampling functions by properly distributing the output port locations along the frequency-position law of the RL-SD. The input port position arbitrariness is realized by adding a calibration array compensating for the frequency deviation induced by the input modification. The frequency range and resolution tunability is achieved by electronic port switching [39].

Chapter 4 presents a time-modulated spread-spectrum metasurface active camouflaging technology. Compared to conventional camouflaging technologies, which are LTI, the proposed technology spreads the incident energy in terms of temporal spectrum. Besides, this technology modulates the metasurface with a pseudo-random sequence, which spreads the spectrum of the incident wave into a noise-like spectrum with minimal power spectral density, and hence maximal camouflaging performance; this is much more efficient than the utilization of completely periodic modulation sequence, which distributes the energy over a small number of harmonics. Finally, the proposed technology provides the extra features of selective camouflaging and interference immunity [13].

5.2 Future Work

5.2.1 Challenges

R-MSP, as a remarkable signal processing technology, has shown many potentials for future signal processing in various areas, as already shown in previous chapters. However, a lot of

work, such as components performance improvement, new concepts and applications, still needs to to further explored.

Dispersion engineering based microwave signal processing provides a new solution to process microwave signal in real-time, features the advantages of low-cost,low-latency, high-efficiency and wide-bandwidth over its conventional counterpart DSP-based digital signal processing. Nevertheless, several challenges are still need to further studied, which includes [1]

1) Closed-form synthesis methods for complex phasers.

2) Realization of phaser with all possible characteristics for required applications.

3) Design and fabrication of phasers in high millimeter-wave frequencies.

Spacetime-modulation can simultaneously manipulate the temporal and spatial spectra of electromagnetic waves, and realize operations that break the fundamental bounds imposed on conventional LTI systems [10, 30]. However, it will need to meet a large number of challenges to turn out a transformative technology. Some of these challenges are listed as follows [47]:

1) Although all the spacetime-modulated metasurfaces described in this thesis have only two states (PEC and PMC), more general amplitude and phase states are required for more sophisticated applications. The engineering of metasurfaces offering such response diversity is of great complexity.

2) Most of the designs of spacetime-modulated metasurfaces require lumped elements, such as diodes and varactors. These elements typically include parasitic resistances which leads to non-negligible loss, whose mitigation is not trivial.

3) Time-modulated metasurfaces induce temporal frequency transitions, i.e. the generation of new temporal frequencies, as nonlinear systems. In some applications, such as that of camouflaging, such temporal frequency generation is naturally desired. However, it may be undesired in other applications, such as for instance refraction and multiplexing. The termination of undesired frequencies is an area that still needs to be explored.

5.2.2 Wireless Communication systems

One of potential directions is spacetime modulated metasurface based wireless communication systems. Today's wireless communication systems demands high throughput and low latency to satisfy current users' daily life requirements. These make the wireless communication systems become more and more complicated to achieve the demands. MIMO system, as an emerging wireless communication system to provide high antenna gain, flex-

ible beam steering and spatial exploration capability, has been widely applied in current wireless communication systems. However, as MIMO system requires more and more antennas, for instance, massive MIMO system, it requires more RF front-end circuits and hance more power-consumption, which greatly increases the cost of the design. Here I propose two potential spacetime applications for wireless communication systems.

Direction of Arrival (DoA) Estimation [130]

The concept of the proposed DoA-estimation spacetime-modulated metasurface system is depicted in Fig. 5.1. This system is formed by the combination of a spacetime-modulated 2D-patch periodic metasurface with period p, a receiving antenna front-end and a modulating/demodulating FPGA processor. The N rows of patches are simultaneously modulated by N orthogonal codes generated by an FPGA, which corresponds to spacetime modulated system. The codes used to modulate the metasurface are simultaneously sent to the demodulator which multiples them with the signal received by the antenna to determine the DOA.

Spatial Multiplexing [131]

Figure 5.2 shows the principle of the proposed spacetime modulated metasurface. Here, two signals, $s_1(t)$ and $s_2(t)$, having different baseband waveforms but sharing the same bandwidth and carrier frequency (f_0) are combined together, and radiated through the same antenna. This wave impinges then on the metasurface, which is spacetime-modulated by an external processing unit. The metasurface consists of a 2D array of grounded patches having each a ground connection equipped with a switching diode, so that the structure operates as a mirror with two reflection phase states, which are here design to differ by π. These phase states are controlled by the processing unit, which modulates each of the N columns of the metasurface with a different periodic binary time sequence with period T from an orthogonal set, $\{m_n(t)\}$, with $n = 1, 2, \ldots, N$, and $\int_T m_i(t)m_j(t)dt = \delta_{ij}$ where δ_{ij} is the Kronecker delta function.

In order to be routed to the different directions θ_1 and θ_2 the signals $s_1(t)$ and $s_2(t)$ are precoded, before being radiated, as shown in Fig. 5.2. Specifically, $s_1(t)$ and $s_2(t)$ are respectively multiplied by $\mathbf{c}_1 = [c_{11}, c_{12}, \ldots, c_{1N}]$ and $\mathbf{c}_2 = [c_{21}, c_{22}, \ldots, c_{2,N}]$, which are the phase-gradient vectors defined as $c_{1n} = 2\pi f_0 nd \sin\theta_1/c$ and $c_{2n} = 2\pi f_0 nd \sin\theta_2/c$ corresponding to the directions θ_1 and θ_2, where c is the speed of light in free space and d is the spacing between the patches.

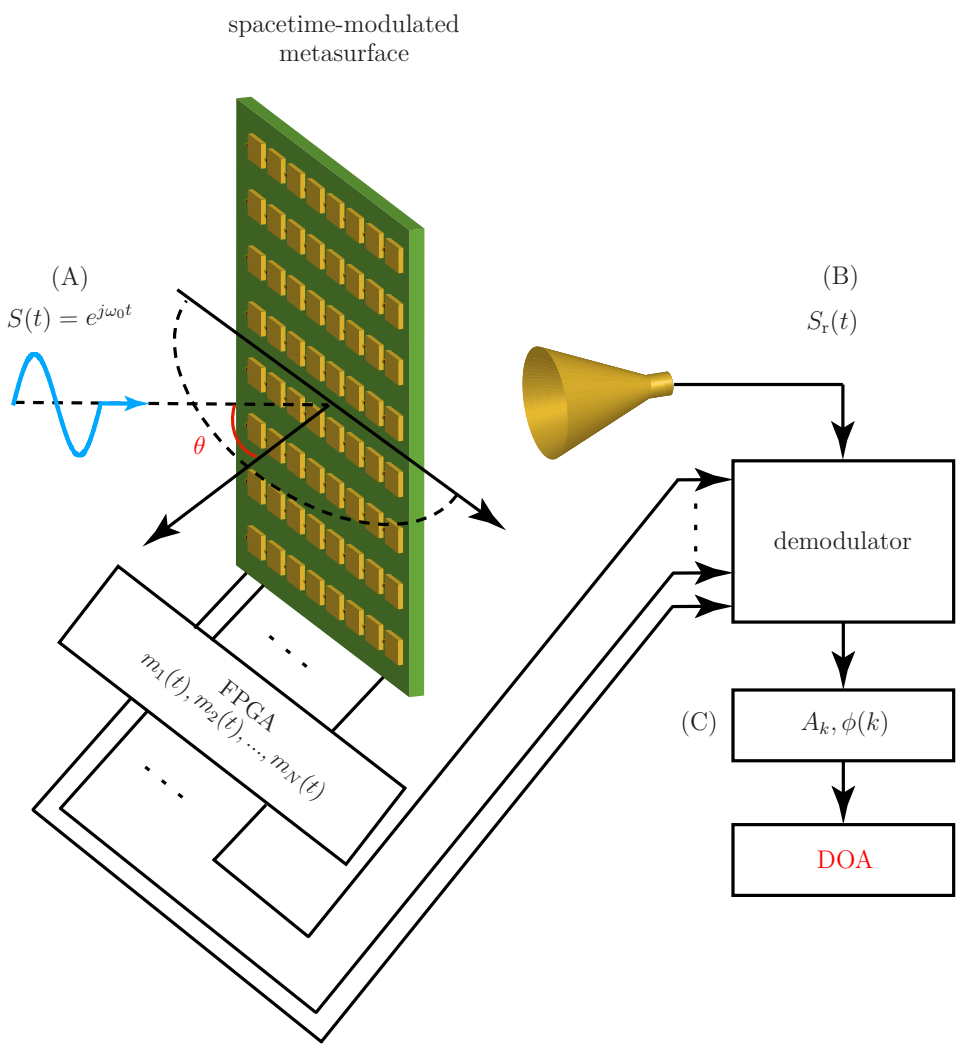

Figure 5.1 Proposed concept of direction of arrival (DOA) estimation based on a spacetime-modulated modulated.

Assuming proper synchronization, the signal reflected by the n_{th} column only contains two terms $c_{1n}s_1(t) + c_{2n}s_2(t)$, due to coding orthogonality. Therefore, the two signals $s_1(t)$ and $s_2(t)$ are reflected to the specified directions θ_1 and θ_2 upon reflection combination from all the patch columns of the metasurface, according antenna array theory.

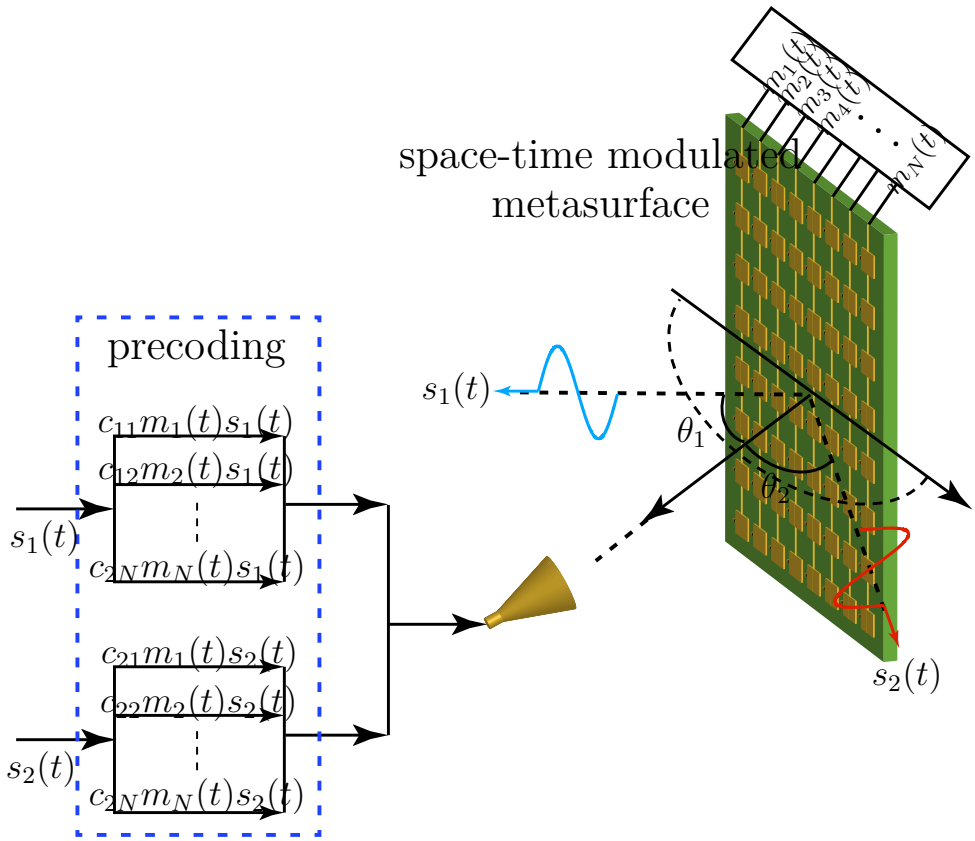

Figure 5.2 Schematic of the proposed spacetime modulated metasurface for spatial multiplexing.

REFERENCES

[1] C. Caloz, S. Gupta, Q. Zhang, and B. Nikfal, "Analog signal processing: A possible alternative or complement to dominantly digital radio schemes," *IEEE Microw. Mag.*, vol. 14, no. 6, pp. 87 – 103, Sept. 2013.

[2] S. Gupta, A. Parsa, E. Perret, R. V. Snyder, R. J. Wenzel, and C. Caloz, "Group-delay engineered noncommensurate transmission line all-pass network for analog signal processing," *IEEE Trans. Microw. Theory Techn.*, vol. 58, no. 9, pp. 2392 – 2407, Sept. 2010.

[3] Q. Zhang, S. Gupta, and C. Caloz, "Synthesis of narrowband reflection-type phasers with arbitrary prescribed group delay," *IEEE Trans. Microw. Theory Techn.*, vol. 60, no. 8, pp. 2394 – 2402, Aug. 2012.

[4] M. A. G. Laso, T. Lopetegi, M. J. Erro, D. Benito, M. J. Garde, M. A. Muriel, M. Sorolla, and M. Guglielmi, "Real-time spectrum analysis in microstrip technology," *IEEE Trans. Microw. Theory Techn.*, vol. 51, no. 3, pp. 705–717, 2003.

[5] S. Abielmona, S. Gupta, and C. Caloz, "Compressive receiver using a CRLH-based dispersive delay line for analog signal processing," *IEEE Trans. Microw. Theory Techn.*, vol. 57, no. 11, pp. 2617 – 2626, Nov. 2009.

[6] S. Gupta, S. Abielmona, and C. Caloz, "Microwave analog real-time spectrum analyzer (RTSA) based on the spectral-spatial decomposition property of leaky-wave structures," *IEEE Trans. Microw. Theory Techn.*, vol. 57, no. 12, pp. 2989 – 2999, Dec. 2009.

[7] G. Zhang, Q. Zhang, Y. Chen, T. Guo, C. Caloz, and R. D. Murch, "Dispersive feeding network for arbitrary frequency beam scanning in array antennas," *IEEE Trans. Antennas Propag.*, vol. 65, no. 6, pp. 3033–3040, June 2017.

[8] B. Nikfal, S. Gupta, and C. Caloz, "Increased group delay slope loop system for enhanced-resolution analog signal processing," *IEEE Trans. Microw. Theory Techn.*, vol. 59, no. 6, pp. 1622 – 1628, Jun. 2011.

[9] B. Nikfal, Q. Zhang, and C. Caloz, "Enhanced-SNR impulse radio transceiver based on phasers," *IEEE Microw. Wireless Compon. Lett.*, vol. 24, no. 11, pp. 778 – 780, Nov. 2014.

[10] C. Caloz and Z. Deck-Léger, "Spacetime metamaterials, part I: General concepts," *IEEE Trans. Antennas Propag.*, 2020.

[11] A. Akbarzadeh, N. Chamanara, and C. Caloz, "Inverse prism based on temporal discontinuity and spatial dispersion," *Opt. Lett.*, vol. 43, no. 14, pp. 3297–3300, Jul 2018. [Online]. Available: http://ol.osa.org/abstract.cfm?URI=ol-43-14-3297

[12] W. Tang, X. Li, J. Y. Dai, S. Jin, Y. Zeng, Q. Cheng, and T. J. Cui, "Wireless communications with programmable metasurface: Transceiver design and experimental results," *China Commun.*, vol. 16, no. 5, pp. 46–61, May 2019.

[13] X. Wang and C. Caloz, "Spread-spectrum selective camouflaging based on time-modulated metasurface," *IEEE Trans. Antennas Propag.*, 2020 (In Press).

[14] A. Shaltout, A. Kildishev, and V. Shalaev, "Time-varying metasurfaces and Lorentz non-reciprocity," *Opt. Mater. Express*, vol. 5, no. 11, pp. 2459–2467, 2015.

[15] Z. Wu and A. Grbic, "Serrodyne frequency translation using time-modulated metasurfaces," *IEEE Trans. Antennas Propag.*, 2020.

[16] Y. Zhang and V. Fusco, "Rotman lens used as a demultiplexer/multiplexer," in *2012 42nd European Microwave Conference*, Oct. 2012, pp. 164–167.

[17] C. E. Shannon, "A mathematical theory of communication," *The Bell system technical journal*, vol. 27, no. 3, pp. 379–423, 1948.

[18] L. Zou, "Dispersion based real-time analog signal processing (R-ASP) and application to wireless communications," Ph.D. dissertation, École Polytechnique de Montréal, 2017.

[19] Q. Zhang, S. Gupta, and C. Caloz, "Synthesis of broadband phasers formed by commensurate C- and D-sections," *Int. J. RF Microw. Comput. Aided Eng.*, vol. 24, no. 3, pp. 322 – 331, May 2014.

[20] S. Gupta, Q. Zhang, L. Zou, L. Jiang, and C. Caloz, "Generalized coupled-line all-pass phasers," *IEEE Trans. Microw. Theory Techn.*, vol. 63, no. 3, pp. 1 – 12, Mar. 2015.

[21] Y. Horii, S. Gupta, B. Nikfal, and C. Caloz, "Multilayer broadside-coupled dispersive delay structures for analog signal processing," *IEEE Microw. Wireless Compon. Lett.*, vol. 22, no. 1, pp. 1 – 3, Jan. 2012.

[22] X. Wang, L. Zou, and C. Caloz, "Tunable C-section phaser for dynamic analog signal processing," in *Proc. XXXIInd URSI GASS*, Aug 2017.

[23] Q. Zhang, D. L. Sounas, and C. Caloz, "Synthesis of cross-coupled reduced-order dispersive delay structures (DDS) with arbitrary group delay and controlled magnitude," *IEEE Trans. Microw. Theory Techn.*, vol. 61, no. 3, pp. 1043 – 1052, Mar. 2013.

[24] M. A. G. Laso, T. Lopetegi, M. J. Erro, D. Benito, M. J. Garde, M. A. Muriel, M. Sorolla, and M. Guglielmi, "Real-time spectrum analysis in microstrip technology," *IEEE Trans. Microw. Theory Techn.*, vol. 51, no. 3, pp. 705 – 717, Mar. 2003.

[25] L. Zou, S. Gupta, and C. Caloz, "Loss-gain equalized reconfigurable C-section analog signal processor," *IEEE Trans. Microw. Theory Techn.*, vol. 65, no. 2, pp. 555–564, 2017.

[26] X. Wang, A. Akbarzadeh, L. Zou, and C. Caloz, "Flexible-resolution, arbitrary-input and tunable Rotman lens spectrum decomposer," *IEEE Trans. Antennas Propag.*, vol. 66, no. 8, 2018.

[27] X. Wang, L. Zou, Z.-L. Deck-Léger, J. Azaña, and C. Caloz, "Coupled loop resonator Hilbert transformer," in *Proc. IEEE Int. Symp. on Antennas Propag.*, July 2018.

[28] L. Zou, S. Gupta, and C. Caloz, "Real-time dispersion code multiple access for high-speed wireless communications," *IEEE Trans. Wirel. Commun.*, vol. 17, no. 1, pp. 266–281, Jan 2018.

[29] X. Wang and C. Caloz, "Phaser-based polarization-dispersive antenna and application to encrypted communication," in *Proc. IEEE Int. Symp. on Antennas Propag.*, July 2017.

[30] C. Caloz and Z. Deck-Léger, "Spacetime metamaterials, part II: Theory and applications," *IEEE Trans. Antennas Propag.*, 2020.

[31] J. Y. Dai, W. K. Tang, J. Zhao, X. Li, Q. Cheng, J. C. Ke, M. Z. Chen, S. Jin, and T. J. Cui, "Metasurfaces: Wireless communications through a simplified architecture based on time-domain digital coding metasurface," *Adv. Mater. Technol.*, vol. 4, no. 7, p. 1970037, 2019.

[32] T. J. Cui, S. Liu, G. D. Bai, Q. Ma *et al.*, "Direct transmission of digital message via programmable coding metasurface," *Research*, p. 2584509, 2019.

[33] J. Zhao, X. Yang, J. Y. Dai, Q. Cheng, X. Li, N. H. Qi, J. C. Ke, G. D. Bai, S. Liu, S. Jin, A. Alù, and T. J. Cui, "Programmable time-domain digital-coding metasurface for non-linear harmonic manipulation and new wireless communication systems," *Natl. Sci. Rev.*, vol. 6, no. 2, pp. 231–238, 11 2018.

[34] X. Wang and C. Caloz, "Direction-of-arrival (doa) estimation based on spacetime-modulated metasurface," in *IEEE AP-S Int. Antennas Propag. (APS)*, Atlanta, USA, July 2019.

[35] M. Liu, D. A. Powell, Y. Zarate, and I. V. Shadrivov, "Huygens' metadevices for parametric waves," *Phys. Rev. X*, vol. 8, no. 3, p. 031077, 2018.

[36] D. Ramaccia, D. L. Sounas, A. Alù, A. Toscano, and F. Bilotti, "Doppler cloak restores invisibility to objects in relativistic motion," *Phys. Rev. B*, vol. 95, p. 075113, Feb 2017.

[37] N. Chamanara, Y. Vahabzadeh, and C. Caloz, "Simultaneous control of the spatial and temporal spectra of light with space-time varying metasurfaces," *IEEE Trans. Antennas Propag.*, vol. 67, no. 4, pp. 2430–2441, April 2019.

[38] X. Wang, Z.-L. Deck-Léger, L. Zou, J. Azaña, and C. Caloz, "Microwave Hilbert transformer and its applications in real-time analog processing (RAP)," *IEEE Trans. Microw. Theory Tech.*, vol. 67, no. 6, pp. 2216–2226, June 2019.

[39] X. Wang, A. Akbarzadeh, L. Zou, and C. Caloz, "Flexible-resolution, arbitrary-input, and tunable Rotman lens spectrum decomposer," *IEEE Trans. Antennas Propag.*, vol. 66, no. 8, pp. 3936–3947, Aug. 2018.

[40] X. Wang, A. Akbarzadeh, L. Zou, and C. Caloz, "Real-time spectrum sniffer for cognitive radio based on Rotman lens spectrum decomposer," *IEEE Access*, vol. 6, pp. 52 366–52 373, 2018.

[41] R. Pettersson, "Visual camouflage," *J. Vis. Lit.*, vol. 37, no. 3, pp. 181–194, 2018.

[42] C. Wang, X. Han, P. Xu, X. Zhang, Y. Du, S. Hu, J. Wang, and X. Wang, "The electromagnetic property of chemically reduced graphene oxide and its application as microwave absorbing material," *Appl. Phys. Lett.*, vol. 98, no. 7, p. 072906, 2011.

[43] T. Xia, C. Zhang, N. A. Oyler, and X. Chen, "Hydrogenated tio_2 nanocrystals: A novel microwave absorbing material," *Adv. Mater.*, vol. 25, no. 47, pp. 6905–6910, 2013.

[44] U. Lima, M. Nasar, R. Nasar, M. Rezende, and J. Araújo, "Ni–Zn nanoferrite for radar-absorbing material," *J. Magn. Magn. Mater.*, vol. 320, no. 10, pp. 1666 – 1670, 2008.

[45] A. Bondeson, Y. Yang, and P. Weinerfelt, "Optimization of radar cross section by a gradient method," *IEEE Trans. Magn*, vol. 40, no. 2, pp. 1260–1263, March 2004.

[46] X. Wang and C. Caloz, "Spacetime-modulated metasurface camouflaging," in *IEEE International Symposium on Antennas and Propagation (AP-S)*, Montreal, Canada, 2020.

[47] ——, "Advances in spacetime modulated metasurface," in *XXXIII General Assembly and Scientific Symposium of the International Union of Radio Science (URSI GASS)*, Rome, Italy, 2020.

[48] X. Wang and C. Caloz, "Spread-spectrum camouflaging based on time-modulated metasurface," in *IEEE International Symposium on Antennas and Propagation (AP-S)*, Atlanta, USA, 2019.

[49] J. Azaña, "Ultrafast analog all-optical signal processors based on fiber-grating devices," *IEEE Photonics J.*, vol. 2, no. 3, pp. 359–386, June 2010.

[50] R. Salem, M. A. Foster, and A. L. Gaeta, "Application of space-time duality to ultrahigh-speed optical signal processing," *Adv. Opt. Photon.*, vol. 5, no. 3, pp. 274–317, Sep. 2013.

[51] H. V. Nguyen and C. Caloz, "First-and second-order differentiators based on coupled-line directional couplers," *IEEE Microw. Wirel. Compon. Lett.*, vol. 18, no. 12, pp. 791–793, 2008.

[52] W. Liu, M. Li, R. S. Guzzon, E. J. Norberg, E. J. Norberg, J. S. Parker, M. Lu, L. A. Coldren, and J. Yao, "A fully reconfigurable photonic integrated signal processor," *Nat. Photonics*, vol. 10, no. 2, pp. 190–195, Jan. 2016.

[53] J. D. Schwartz, J. Azaña, and D. V. Plant, "An electronic temporal imaging system for compression and reversal of arbitrary UWB waveforms," in *Proc. IEEE Radio and Wireless Symp.*, Orlando, FL. U.S., Jan. 2008, pp. 487 – 490.

[54] H. P. Bazargani, M. D. R. Fernández-Ruiz, and J. Azãna, "Tunable, nondispersive optical filter using photonic hilbert transformation," *Opt. Lett.*, vol. 39, no. 17, pp. 5232–5235, Sept. 2014.

[55] K. Tanaka, K. Takano, K. Kondo, and K. Nakagawa, "Improved sideband suppression of optical ssb modulation using all-optical Hilbert transformer," *Electron. Lett.*, vol. 38, no. 3, pp. 133–134, Jan 2002.

[56] Z. Li, Y. Han, H. Chi, X. Zhang, and J. Yao, "A continuously tunable microwave fractional Hilbert transformer based on a nonuniformly spaced photonic microwave delay-line filter," *J. Lightwave Technol.*, vol. 30, no. 12, pp. 1948–1953, Jun 2012.

[57] H. Emami, N. Sarkhosh, L. A. Bui, and A. Mitchell, "Wideband RF photonic in-phase and quadrature-phase generation," *Opt. Lett.*, vol. 33, no. 2, pp. 98–100, Jan 2008.

[58] R. Ashrafi and J. Azaña, "Terahertz bandwidth all-optical Hilbert transformers based on long-period gratings," *Opt. Lett.*, vol. 37, no. 13, pp. 2604–2606, Jul 2012.

[59] H. Shahoei, P. Dumais, and J. Yao, "Continuously tunable photonic fractional Hilbert transformer using a high-contrast germanium-doped silica-on-silicon microring resonator," *Opt. Lett.*, vol. 39, no. 9, pp. 2778–2781, May 2014.

[60] L. Zhuang, M. R. Khan, W. Beeker, A. Leinse, R. Heideman, and C. Roeloffzen, "Novel microwave photonic fractional Hilbert transformer using a ring resonator-based optical all-pass filter," *Opt. Express*, vol. 20, no. 24, pp. 26 499–26 510, Nov 2012.

[61] S. L. Hahn, *Hilbert transforms in signal processing.* Artech House Boston, 1996.

[62] B. Liu, C. Sima, W. Yang, B. Cai, D. Liu, Y. Yu, J. Gates, M. Zervas, and P. Smith, "Experimental investigation of large time–bandwidth product photonic Hilbert transformer based on compact bragg grating," *IEEE Photonics J.*, vol. 8, no. 4, pp. 1–8, 2016.

[63] D. M. Pozar, *Microwave Engineering 4th Ed.* John Wiley, 2011.

[64] G. Waldman, *Introduction to light: The physics of light, vision, and color.* Courier Corporation, 2002.

[65] Z. Knittl, *Optics of thin films: an optical multilayer theory.* Wiley London, 1976.

[66] M. Born and E. Wolf, *Principles of optics: electromagnetic theory of propagation, interference and diffraction of light.* Elsevier, 2013.

[67] B. E. A. Saleh and M. C. Teich, "Fundamentals of photonics," *Wiley*, 2007.

[68] C. J. Kok and M. C. Boshoff, "New spectrophotometer and tristimulus mask colorimeter," *Appl. Opt.*, vol. 10, no. 12, pp. 2617–2620, 1971.

[69] S. Gupta, S. Abielmona, and C. Caloz, "Microwave analog real-time spectrum analyzer (RTSA) based on the spectral-spatial decomposition property of leaky-wave structures," *IEEE Trans. Microw. Theory Techn.*, vol. 57, no. 12, pp. 2989–2999, Dec. 2009.

[70] T. M. Hard, "Laser wavelength selection and output coupling by a grating," *Appl. Opt.*, vol. 9, no. 8, pp. 1825–1830, 1970.

[71] T. W. Hänsch, "Repetitively pulsed tunable dye laser for high resolution spectroscopy," *Appl. Opt.*, vol. 11, no. 4, pp. 895–898, 1972.

[72] J. U. White, "Gratings as broad band filters for the infra-red," *J. Opt. Soc. Am.*, vol. 37, no. 9, pp. 713–717, 1947.

[73] K. Knop, "Diffraction gratings for color filtering in the zero diffraction order," *Appl. Opt.*, vol. 17, no. 22, pp. 3598–3603, 1978.

[74] C. A. Brackett, "Dense wavelength division multiplexing networks: principles and applications," *IEEE J. Sel. Areas Commun.*, vol. 8, no. 6, pp. 948–964, Aug. 1990.

[75] P. S. Henry and J. T. Ruscio, "A low-loss diffraction grating frequency multiplexer," *IEEE Trans. Microw. Theory Techn.*, vol. 26, no. 6, pp. 428–433, Jun. 1978.

[76] H. Zmuda, R. A. Soref, P. Payson, S. Johns, and E. N. Toughlian, "Photonic beamformer for phased array antennas using a fiber grating prism," *IEEE Photon. Technol.*, vol. 9, no. 2, pp. 241–243, Feb. 1997.

[77] O. Momeni and E. Afshari, "Electrical prism: A high quality factor filter for millimeter-wave and terahertz frequencies," *IEEE Trans. Microw. Theory Techn.*, vol. 57, no. 11, pp. 2790–2799, Nov. 2009.

[78] E. Afshari, H. S. Bhat, and A. Hajimiri, "Ultrafast analog fourier transform using 2-D LC lattice," *IEEE Trans. Circuits Syst*, vol. 55, no. 8, pp. 2332–2343, Sept. 2008.

[79] J. L. Gómez-Tornero, A. J. Martínez-Ros, S. Mercader-Pellicer, and G. Goussetis, "Simple broadband quasi-optical spatial multiplexer in substrate integrated technology," *IEEE Trans. Microw. Theory Techn.*, vol. 63, no. 5, pp. 1609–1620, May 2015.

[80] M. K. Smit and C. V. Dam, "Phasar-based WDM-devices: Principles, design and applications," *IEEE J. Sel. Top. Quantum Electron.*, vol. 2, no. 2, pp. 236–250, Jun. 1996.

[81] R. Rotman, M. Tur, and L. Yaron, "True time delay in phased arrays," *Proc. IEEE*, vol. 104, no. 3, pp. 504–518, March 2016.

[82] W. Rotman and R. Turner, "Wide-angle microwave lens for line source applications," *IEEE Trans. Antennas Propag.*, vol. 11, no. 6, pp. 623–632, Nov. 1963.

[83] R. C. Hansen, "Design trades for Rotman lenses," *IEEE Trans. Antennas Propag.*, vol. 39, no. 4, pp. 464–472, Apr. 1991.

[84] S. Vashist, M. K. Soni, and P. K. Singhal, "A review on the development of rotman lens antenna," *Chinese Journal of Engineering*, 2014.

[85] X. D. Bai, X. L. Liang, J. P. Li, K. Wang, J. P. Geng, and R. H. Jin, "Rotman lens-based circular array for generating five-mode oam radio beams," *Sci. Rep.*, vol. 6, p. 27815, 2016.

[86] J. Dong, "Microwave lens designs: Optimization, fast simulation algorithms, and 360-degree scanning techniques," Ph.D. dissertation, Virginia Tech, 2009.

[87] J. Kim, C. S. Cho, and F. S. Barnes, "Dielectric slab Rotman lens for microwave/millimeter-wave applications," *IEEE Trans. Microw. Theory Tech.*, vol. 53, no. 8, pp. 2622–2627, Aug 2005.

[88] A. Lambrecht, S. Beer, and T. Zwick, "True-time-delay beamforming with a Rotman-lens for ultrawideband antenna systems," *IEEE Trans. Antennas Propag.*, vol. 58, no. 10, pp. 3189–3195, Oct. 2010.

[89] P. K. Singhal, P. C. Sharma, and R. D. Gupta, "Design and analysis of Rotman type lens using hyperbolic focal arc for wide angle scanning," in *Asia Pacic Microw. Conf*, vol. 3, 1999, pp. 932–935.

[90] N. J. G. Fonseca, "A focal curve design method for Rotman lenses with wider angular scanning range," *IEEE Antennas Wireless Propag. Lett.*, vol. 16, pp. 54–57, 2017.

[91] X. C. Zhu, W. Hong, P. P. Zhang, Z. C. Hao, H. J. Tang, K. Gong, J. X. Chen, and K. Wu, "Extraction of dielectric and rough conductor loss of printed circuit board using differential method at microwave frequencies," *IEEE Trans. Microw. Theory Tech.*, vol. 63, no. 2, pp. 494–503, Feb 2015.

[92] Y. C. Liang, K. C. Chen, G. Y. Li, and P. Mahonen, "Cognitive radio networking and communications: an overview," *IEEE Trans. Veh. Technol.*, vol. 60, no. 7, pp. 3386–3407, Sept. 2011.

[93] A. Osseiran, J. F. Monserrat, and P. Marsch, *5G mobile and wireless communications technology.* Cambridge University Press, 2016.

[94] A. Ghasemi and E. S. Sousa, "Spectrum sensing in cognitive radio networks: requirements, challenges and design trade-offs," *IEEE Commun. Mag.*, vol. 46, no. 4, 2008.

[95] D. Bhargavi and C. R. Murthy, "Performance comparison of energy, matched-filter and cyclostationarity-based spectrum sensing," in *SPAWC, 2010 IEEE 17th Int. Workshop on*, 2010.

[96] T. Yucek and H. Arslan, "A survey of spectrum sensing algorithms for cognitive radio applications," *IEEE Commu. Surveys & Tutorials*, vol. 11, no. 1, pp. 116–130, 2009.

[97] G. Ding, J. Wang, Q. Wu, F. Song, and Y. Chen, "Spectrum sensing in opportunity-heterogeneous cognitive sensor networks: How to cooperate?" *IEEE Sensors Journal*, vol. 13, no. 11, pp. 4247–4255, 2013.

[98] B. Nikfal, D. Badiere, M. Repeta, B. Deforge, S. Gupta, and C. Caloz, "Distortion-less real-time spectrum sniffing based on a stepped group-delay phaser," *IEEE Microw. Wirel. Compon. Lett.*, vol. 22, no. 11, pp. 601–603, 2012.

[99] X. Wang, A. Akbarzadeh, L. Zou, and C. Caloz, "Flexible-resolution, arbitrary-input and tunable Rotman lens spectrum decomposer," *IEEE Trans. Antennas Propag.*, vol. 66, no. 8, 2018.

[100] M. Stevens and S. Merilaita, *Animal Camouflage: Mechanisms and Function.* Cambridge University Press, 2011.

[101] D. D. Lynch and I. of Electrical Engineers, *Introduction to RF Stealth.* SciTech, 2004.

[102] B. Chambers and A. Tennant, "The phase-switched screen," *IEEE Antenn. Prooag. M.*, vol. 46, no. 6, pp. 23–37, 2004.

[103] A. Tennant, "Reflection properties of a phase modulating planar screen," *Electron. Lett.*, vol. 33, no. 21, pp. 1768–1769, 1997.

[104] K. Achouri and C. Caloz, "Design, concepts, and applications of electromagnetic metasurfaces," *Nanophotonics*, vol. 7, no. 6, pp. 1095–1116, 2018.

[105] S.-C. Jiang, X. Xiong, Y.-S. Hu, Y.-H. Hu, G.-B. Ma, R.-W. Peng, C. Sun, and M. Wang, "Controlling the polarization state of light with a dispersion-free metastructure," *Phys. Rev. X*, vol. 4, no. 2, p. 021026, 2014.

[106] P. Genevet and F. Capasso, "Breakthroughs in photonics 2013: Flat optics: Wavefronts control with huygens' interfaces," *IEEE Photon. Technol. Lett.*, vol. 6, no. 2, pp. 1–4, 2014.

[107] V. S. Asadchy, Y. Ra'Di, J. Vehmas, and S. Tretyakov, "Functional metamirrors using bianisotropic elements," *Phys. Rev. Lett.*, vol. 114, no. 9, p. 095503, 2015.

[108] E. Karimi, S. A. Schulz, I. De Leon, H. Qassim, J. Upham, and R. W. Boyd, "Generating optical orbital angular momentum at visible wavelengths using a plasmonic metasurface," *Light: Science & Applications*, vol. 3, no. 5, p. e167, 2014.

[109] C. Pfeiffer and A. Grbic, "Controlling vector bessel beams with metasurfaces," *Phys. Rev. Appl.*, vol. 2, no. 4, p. 044012, 2014.

[110] G. Zheng, H. Mühlenbernd, M. Kenney, G. Li, T. Zentgraf, and S. Zhang, "Metasurface holograms reaching 80% efficiency," *Nat. Nanotechnol.*, vol. 10, no. 4, p. 308, 2015.

[111] W. Ye, F. Zeuner, X. Li, B. Reineke, S. He, C.-W. Qiu, J. Liu, Y. Wang, S. Zhang, and T. Zentgraf, "Spin and wavelength multiplexed nonlinear metasurface holography," *Nat. Commun.*, vol. 7, p. 11930, 2016.

[112] D. L. Sounas, T. Kodera, and C. Caloz, "Electromagnetic modeling of a magnetless nonreciprocal gyrotropic metasurface," *IEEE Trans. Antennas Propag.*, vol. 61, no. 1, pp. 221–231, 2012.

[113] C. Caloz, A. Alù, S. Tretyakov, D. Sounas, K. Achouri, and Z.-L. Deck-Léger, "Electromagnetic nonreciprocity," *Phys. Rev. Applied*, vol. 10, p. 047001, Oct 2018.

[114] C. Pfeiffer and A. Grbic, "Generating stable tractor beams with dielectric metasurfaces," *Phys. Rev. B*, vol. 91, p. 115408, Mar 2015.

[115] K. Achouri, O. V. Cespedes, and C. Caloz, "Solar "meta-sails" for agile optical force control," *IEEE Trans. Antennas Propag.*, pp. 1–1, 2019.

[116] A. Silva, F. Monticone, G. Castaldi, V. Galdi, A. Alù, and N. Engheta, "Performing mathematical operations with metamaterials," *Science*, vol. 343, no. 6167, pp. 160–163, 2014.

[117] W. Emerson, "Electromagnetic wave absorbers and anechoic chambers through the years," *IEEE Trans. Antennas Propag.*, vol. 21, no. 4, pp. 484–490, 1973.

[118] M. Li, L. Guo, J. Dong, and H. Yang, "An ultra-thin chiral metamaterial absorber with high selectivity for LCP and RCP waves," *J. Phys. D*, vol. 47, no. 18, p. 185102, 2014.

[119] C. Valagiannopoulos, A. Tukiainen, T. Aho, T. Niemi, M. Guina, S. Tretyakov, and C. Simovski, "Perfect magnetic mirror and simple perfect absorber in the visible spectrum," *Phys. Rev. B*, vol. 91, no. 11, p. 115305, 2015.

[120] Y. Wen, W. Ma, J. Bailey, G. Matmon, X. Yu, and G. Aeppli, "Planar broadband and high absorption metamaterial using single nested resonator at terahertz frequencies," *Opt. Lett.*, vol. 39, no. 6, pp. 1589–1592, 2014.

[121] T. Cwik and R. Mittra, "Scattering from general periodic screens," *Electromagnetics*, vol. 5, no. 4, pp. 263–283, 1985.

[122] K. Chen, Y. Feng, Z. Yang, L. Cui, J. Zhao, B. Zhu, and T. Jiang, "Geometric phase coded metasurface: from polarization dependent directive electromagnetic wave scattering to diffusion-like scattering," *Sci. Rep.*, vol. 6, p. 35968, 2016.

[123] A. Alù, "Mantle cloak: Invisibility induced by a surface," *Phys. Rev. B*, vol. 80, p. 245115, Dec 2009.

[124] M. Dehmollaian, N. Chamanara, and C. Caloz, "Wave scattering by a cylindrical metasurface cavity of arbitrary cross section: Theory and applications," *IEEE Trans. Antennas Propag.*, vol. 67, no. 6, pp. 4059–4072, June 2019.

[125] N. M. Estakhri and A. Alù, "Ultra-thin unidirectional carpet cloak and wavefront reconstruction with graded metasurfaces," *IEEE Antennas Wirel. Propag. Lett*, vol. 13, pp. 1775–1778, 2014.

[126] R. Fleury, F. Monticone, and A. Alù, "Invisibility and cloaking: Origins, present, and future perspectives," *Phys. Rev. Appl.*, vol. 4, no. 3, p. 037001, 2015.

[127] X. Wang and C. Caloz, "Spread-spectrum camouflaging based on time-modulated metasurface," in *IEEE AP-S Int. Antennas Propag. (APS)*, Atlanta, USA, July 2019.

[128] B. P. Lathi and R. A. Green, *Linear Systems and Signals.* Oxford University Press New York, 2005.

[129] D. Torrieri, *Principles of Spread-Spectrum Communication Systems.* Springer, 2018.

[130] X. Wang and C. Caloz, "Direction-of-arrival (DoA) estimation based on spacetime-modulated metasurface," in *IEEE International Symposium on Antennas and Propagation (AP-S)*, Atlanta, USA, 2019.

[131] X. Wang and C. Caloz, "Spacetime-modulated metasurface for spatial multiplexing communication," in *13th International Congress on Artificial Materials for Novel Wave Phenomena (Metamaterials)*, Rome, Italy, 2019.

APPENDIX A LIST OF PUBLICATIONS

Journal Papers

1. X. Wang and C. Caloz. Spread-spectrum selective camouflaging based on time-modulated metasurface. *IEEE Trans. Antennas Propag.*, 2020 (In Press).

2. X. Wang, Z.-L. Deck-Léger, L. Zou, J. Azaña, and C. Caloz. Microwave Hilbert transformer and its applications in real-time analog processing. *IEEE Trans. Microw. Theory Tech.*, 67(6):2216–2226, June 2019.

3. X. Wang, A. Akbarzadeh, L. Zou, and C. Caloz. Real-time spectrum sniffer for cognitive radio based on Rotman lens spectrum decomposer. *IEEE Access*, 6:52366–52373, 2018.

4. X. Wang, A. Akbarzadeh, L. Zou, and C. Caloz. Flexible-resolution, arbitrary-input, and tunable Rotman lens spectrum decomposer. *IEEE Trans. Antennas Propag.*, 66(8):3936–3947, Aug. 2018.

Conferences:

1. X. Wang and C. Caloz. Advances in spacetime modulated metasurface. In *XXXIII General Assembly and Scientific Symposium of the International Union of Radio Science (URSI GASS)*, Rome, Italy, 2020. (***Invited***).

2. X. Wang and C. Caloz. Spacetime-modulated metasurface camouflaging. In *IEEE International Symposium on Antennas and Propagation (AP-S)*, Montreal, Canada, 2020. (***Finalist of student paper competition***).

3. X. Wang and C. Caloz. Spacetime-modulated metasurface for spatial multiplexing communication. In *13th International Congress on Artificial Materials for Novel Wave Phenomena (Metamaterials)*, Rome, Italy, 2019.

4. X. Wang and C. Caloz. Direction-of-arrival (DoA) estimation based on spacetime-modulated metasurface. In *IEEE International Symposium on Antennas and Propagation (AP-S)*, Atlanta, USA, 2019.

5. X. Wang and C. Caloz. Spread-spectrum camouflaging based on time-modulated metasurface. In *IEEE International Symposium on Antennas and Propagation (AP-S)*, Atlanta, USA, 2019. (***3th prize student paper award***).

6. X. Wang, L. Zou, Z.-L. Deck-Léger, J. Azaña, and C. Caloz. Coupled loop resonator Hilbert transformer. In *IEEE International Symposium on Antennas and Propagation (AP-S)*, Bonston, USA, 2018.

7. X. Wang, L. Zou, and C. Caloz. Tunable c-section phaser for dynamic analog signal processing. In *XXXIInd General Assembly and Scientific Symposium of the International Union of Radio Science (URSI GASS)*, Montreal, Canada, 2017.

8. X. Wang and C. Caloz. Phaser-based polarization-dispersive antenna and application to encrypted communication. In *IEEE International Symposium on Antennas and Propagation (AP-S)*, San Diego, USA, 2017.

APPENDIX B LIST OF AWARDS

1. Young Scientist Award
   International Union of Radio Science (URSI), 2020.

2. Finalist of Student Paper Competition
   IEEE International Symposium on Antennas and Propagation (AP-S), 2020. (10/203)

3. Third Prize Student Paper Award
   IEEE International Symposium on Antennas and Propagation (AP-S), 2019. (3/197)